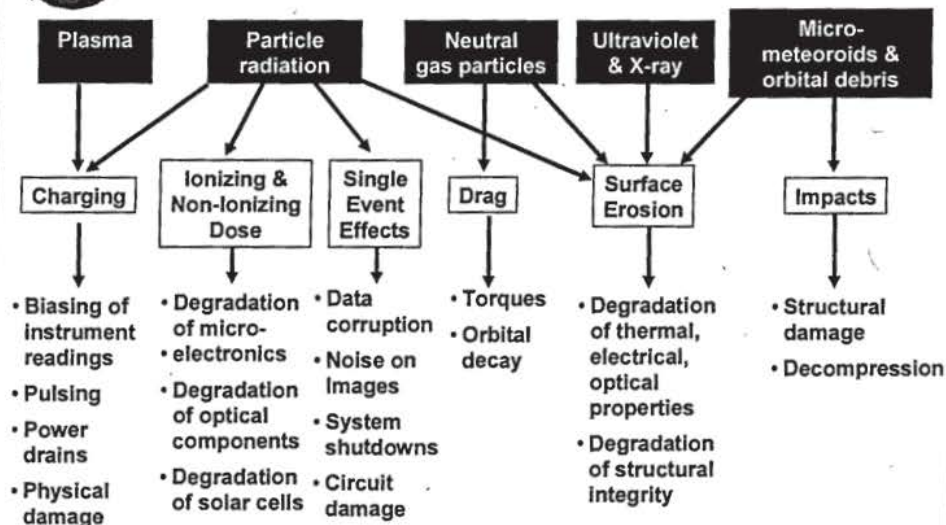# RADECS 2009 Short Course
Session I: The Evolution of the Radiation Environments

Janet Barth
NASA/Goddard Space Flight Center

Dry Run given at Quebec, CA
July 18, 2009

Environments & Effects Overview

Plasma	Particle radiation	Neutral gas particles	Ultraviolet & X-ray	Micro-meteoroids & orbital debris

Charging	Ionizing & Non-Ionizing Dose	Single Event Effects	Drag	Surface Erosion	Impacts

- Biasing of instrument readings
- Pulsing
- Power drains
- Physical damage

- Degradation of micro-electronics
- Degradation of optical components
- Degradation of solar cells

- Data corruption
- Noise on Images
- System shutdowns
- Circuit damage

- Torques
- Orbital decay

- Degradation of thermal, electrical, optical properties
- Degradation of structural integrity

- Structural damage
- Decompression

Session Objectives

- Provide basic understanding of the components of the radiation environment
- Discuss the variations in the environment
- Review progress in model development
- Understand the role of radiation environment definition in system reliability

Outline

- Overview of the Space Environment
- Magnetic Fields and Coordinate Systems
- Particle Populations
  - » Galactic Cosmic Rays
  - » Solar Particles
  - » Trapped Particles
  - » Atmospheric Neutrons

- Dynamics of the Radiation Environment
  - » Source
  - » Effects
- Model Development
- Role of Space Environment Definition in Increasing Reliability

Corona

- ◆ Solar wind source
- ◆ Highly structured region of plasma
- ◆ Expands outward, parallel to solar field lines
- ◆ "Fast" solar wind from non-polar coronal holes

Yohkoh/SXT

Solar Wind

- ◆ **Stream of charged particles from Sun's corona**
  - » Electrons
  - » Protons $\Bigr\}$ Density ~ 1 - 30 / cm^3
  - » Heavy Ions
- ◆ **Magnetized plasma**
- ◆ **Detected out to 10 billion km from Earth by Pioneer 10**
- ◆ **Velocity ~ 300 - 900 km/s**
- ◆ **Energy ~ .5 - 2.0 keV/n**

Components of the Natural Environment

- ◆ Transient
  - » Galactic cosmic rays
    - Protons & heavy ions
  - » Solar particle events
    - Protons & heavier ions
- ◆ Trapped
  - » Electrons, protons, & heavy ions
- ◆ Atmospheric & terrestrial secondaries
  - » Neutrons
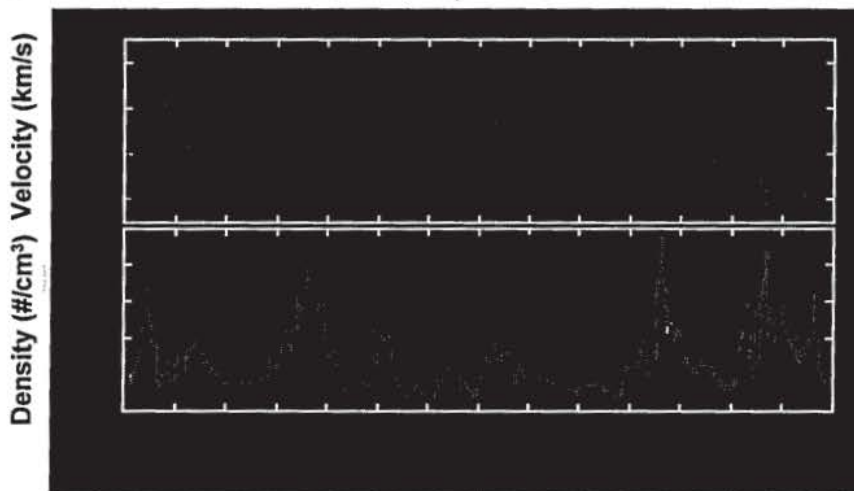
The Radiation Environment
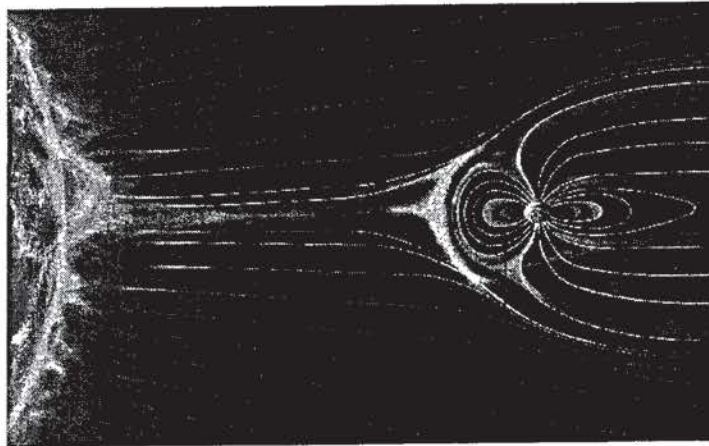
Nikkei Science, Inc. of Japan, by K. Endo

Solar Wind Density & Velocity
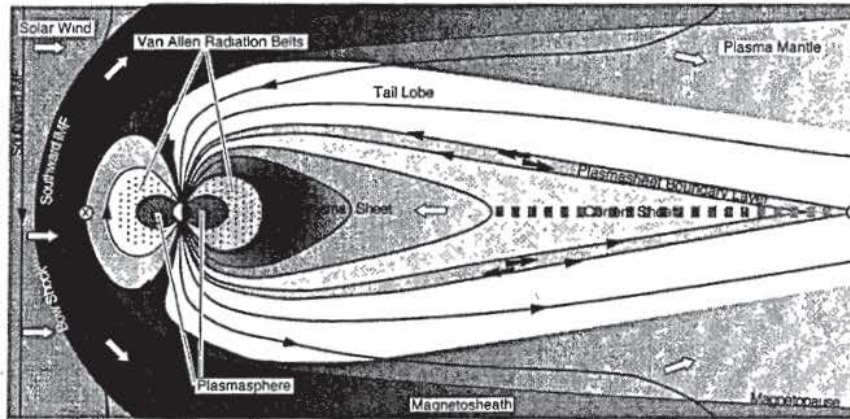
University of Maryland, SOHO/CELIAS

The Magnetosphere

- ◆ Defined by interaction of:
  Earth's magnetic field - Solar wind
- ◆ Solar direction: Compressed to ~ 10 earth radii
- ◆ Anti-solar direction: Stretched into long nagnetotail ~ 300 earth radii
- ◆ Open at the poles
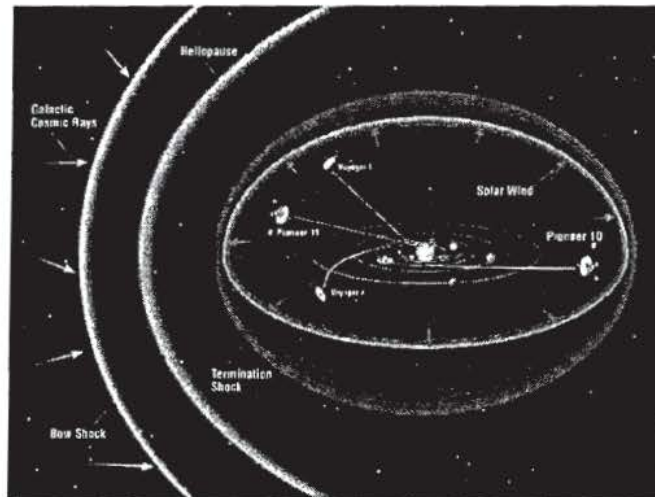- ◆ Bar magnet representation accurate to 4 - 5 earth radii

Magnetosphere

adapted from T. W. Hill by P.H. Reiff

Heliosphere

Outline

- ◆ Overview of the Space Environment
- ◆ Magnetic Fields and Coordinate Systems
- ◆ Particle Populations
  - » Galactic Cosmic Rays
  - » Solar Particles
  - » Trapped Particles
  - » Atmospheric Neutrons
- ◆ Dynamics of the Radiation Environment
  - » Source
  - » Effects
- ◆ Model Development
- ◆ Role of Space Environment Definition in Increasing Reliability
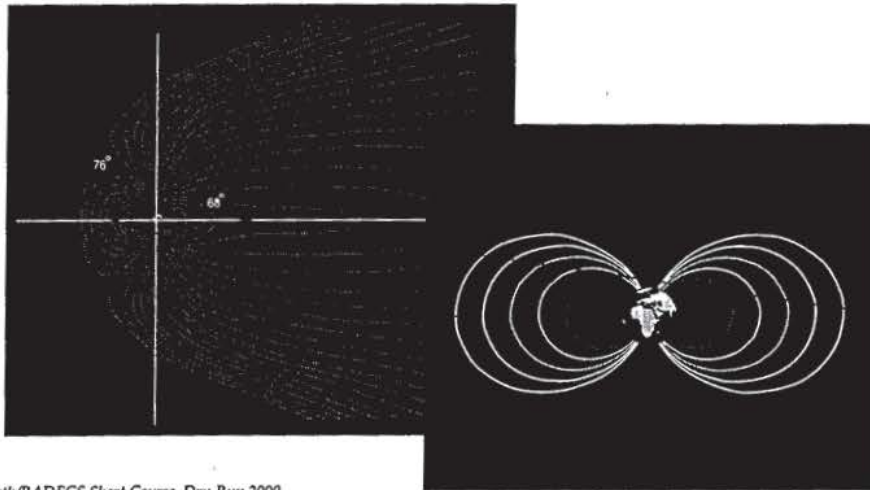
Earth's Magnetic Field

- ◆ Determines distribution of near earth particles
  - » Confines trapped particles to magnetic field lines
  - » Filters interplanetary
- ◆ Combination of two fields
  - » Internal field
    - – Induced by Earth's core
    - – IGRF series of models - IGRF/95
  - » External field
    - – Transported & induced by the solar wind
    - – Pfitzer-Olsen Model - Quiet & Stormy
    - – Tsyganenko Models - Several disturbance levels
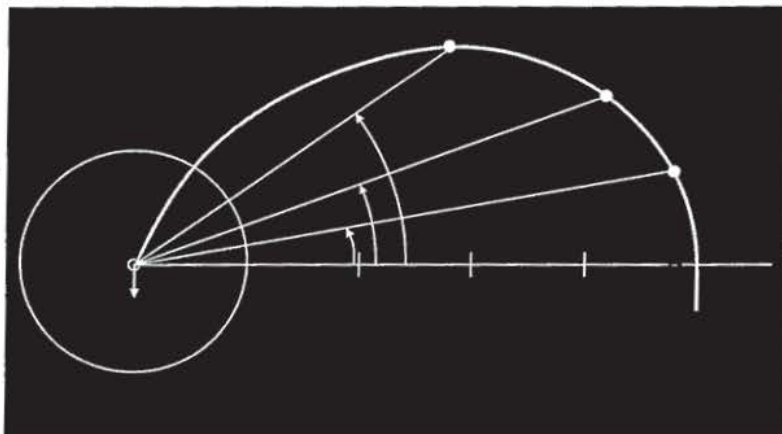
Internal & External Field Models

B-L Coordinate System - Dipole

B - Magnetic Field Strength
L - Distance at Equatorial Crossing in Earth Radii


after Stassinopoulos

Particle Penetration into the Magnetosphere

- ◆ Most solar wind particles are deflected (99.9%)
  - » Some become trapped & energized
- ◆ Galactic Cosmic Ray & Solar Particle penetration Depends on:
  - » Particle energy
  - » Ionization state
    - – Galactic fully ionized
    - – Solar & anomalous component of GCRs have lower ionization states
- ◆ Measured with magnetic rigidity in units of GV

Magnetic Rigidity

$$\frac{\text{momentum}}{\text{charge}}$$
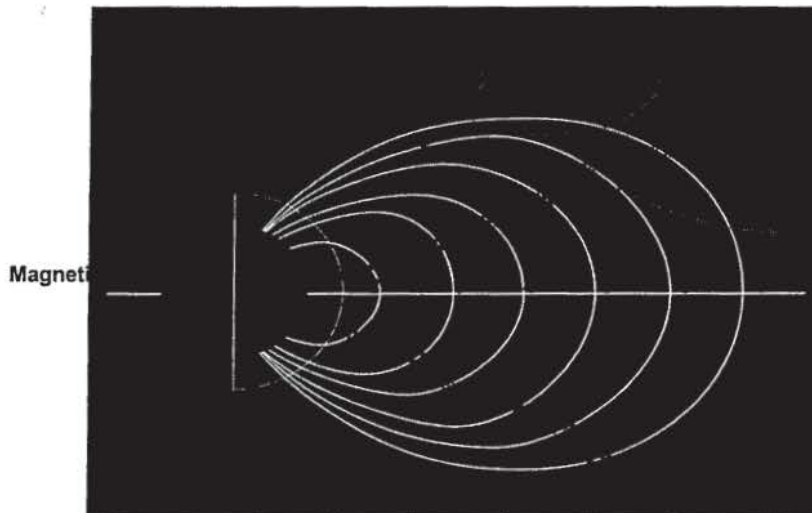
Magneti

after Stassinopoulos

Outline

NASA

- ◆ Overview of the Space Environment
- ◆ Magnetic Fields and Coordinate Systems
- ◆ Particle Populations
  - » Galactic Cosmic Rays
  - » Solar Particles
  - » Trapped Particles
  - » Atmospheric Neutrons

- ◆ Dynamics of the Radiation Environment
  - » Source
  - » Effects
- ◆ Model Development
- ◆ Role of Space Environment Definition in Increasing Reliability

---

Galactic Cosmic Ray Ions

NASA

- ◆ All elements in Periodic Table
- ◆ Energies in GeV
- ◆ Found everywhere in interplanetary space
- ◆ Omnidirectional
- ◆ Mostly fully ionized
- ◆ Cyclic variation in fluence levels
  - » Lowest levels = Solar maximum peak
  - » Highest levels = Lowest point in solar minimum
- ◆ Single Event Effects hazard
- ◆ Model: CREME96

Upsets Induced by Heavy Ions
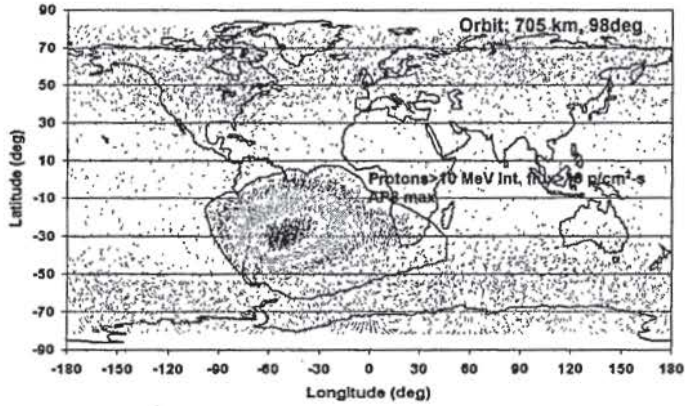
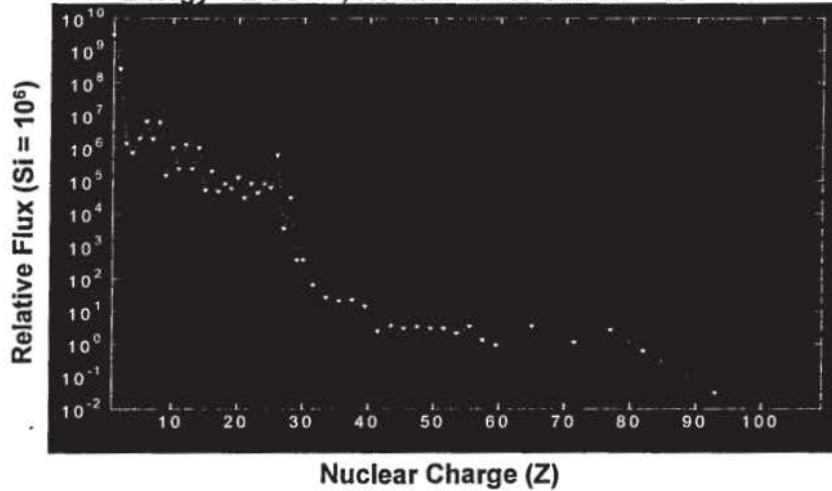Orbit: 705 km, 98deg

Protons>10 MeV Int. flux>10 p/cm²·s AP8 max

• 1SEU • 1<SEU<10 • 10≤SEU<20 • 20≤SEU<40 • ≥ 40 SEU

Single Event Upsets on Seastar Solid State Recorder – Counts for 4 years
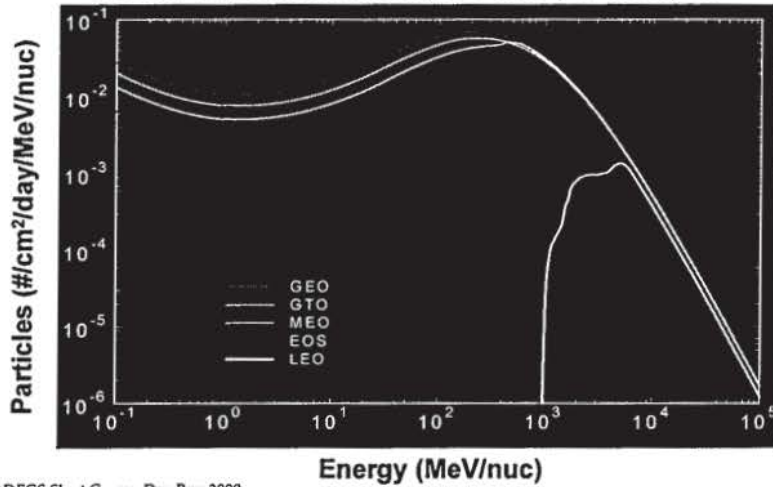
GCRs: Nuclear Composition

Energy = 2 GeV/n, Normalized to Silicon = 10^6

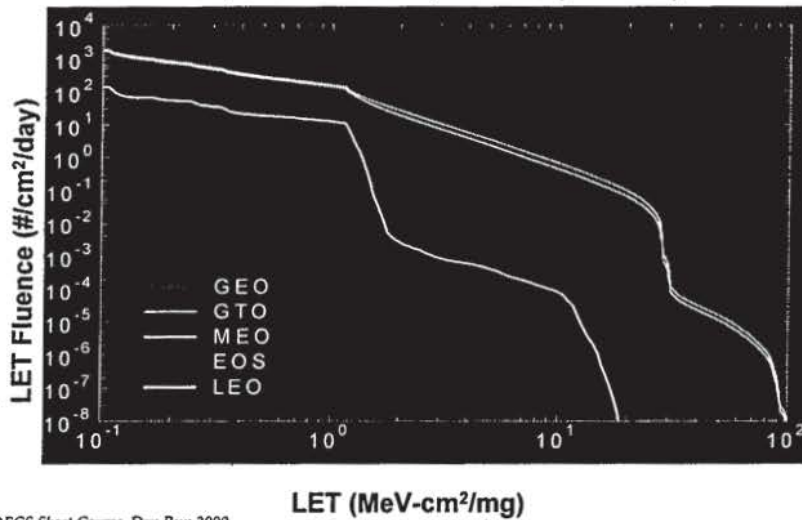# GCRs: Shielded Fluences - Fe

CREME 96, Solar Minimum, 100 mils (2.54 mm) Al

J. Barth/RADECS Short Course Dry-Run 2009

23

GCRs: Integral LET Spectra

CREME 96, Solar Minimum, 100 mils (2.54 mm) Al

J. Barth/RADECS Short Course Dry-Run 2009

24

Solar Particle Events

- ◆ Increased levels of protons & heavy ions
- ◆ Energies
  - » Protons - 100s of MeV
  - » Heavy ions - 100s of GeV
- ◆ Abundances dependent on radial distance from Sun
- ◆ Partially ionized - greater ability to penetrate magnetosphere
- ◆ Number & intensity of events increases dramatically during solar maximum
- ◆ Models
  - » Dose - SOLPRO, JPL, Xapsos/NRL
  - » Single Event Effects - CREME96 (protons & heavy ions)

Impulsive Events

- ◆ Solar flares
- ◆ Particles accelerated directly
- ◆ Heavy ion rich
- ◆ Sharp peak in x-ray emission
- ◆ Concentrated solar longitude distribution
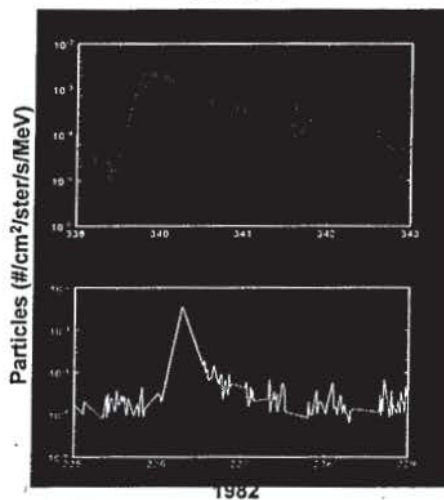
Gradual Events

Holloman AFB/SOON

- ◆ Coronal Mass Ejections
- ◆ Particles accelerated by shock wave
- ◆ Largest proton events
- ◆ Decay of x-ray emission occurs over several hours
- ◆ Large distribution in solar longitude

Gradual vs. Impulsive

Protons

Location of Events
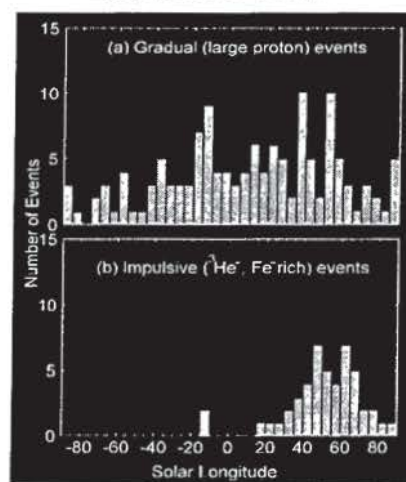
Solar Array Degradation

Average Solar Array Power (Watts)

SC4
SC3
SC2
SC1

Date (28 Oct 03 to 2 Nov 03)
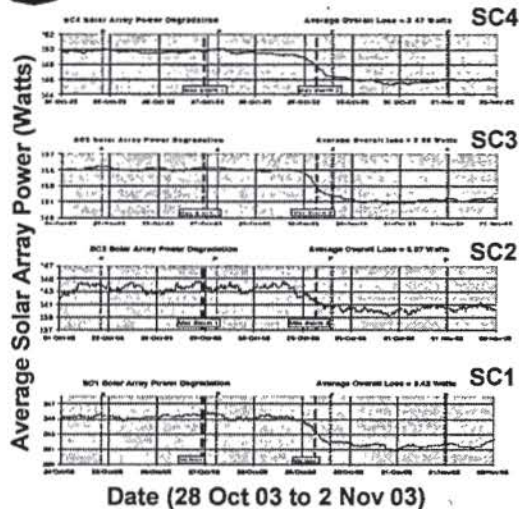
Cluster Spacecraft (4)
Elliptical, Polar orbit
Perigee: 19,000 km
Apogee: 119,000 km

increased levels of protons
during the Oct-Nov 2003
solar particle events

⇩

Increased rate of solar cell
degradation

Single Event Upsets on Seastar Solid State Recorder – Daily Counts

Orbit: 705km, 98 deg

November 9, 2000

July 14&15, 2000

SEU count per day

telemetry dropouts

April 15, 2001   November 5&6, 2001
September 25, 2001
April 21, 2002
August 24, 2002

Solar
particle
events

Background
Trapped protons
& Cosmic ray
heavy ions

Data from Orbital Sciences
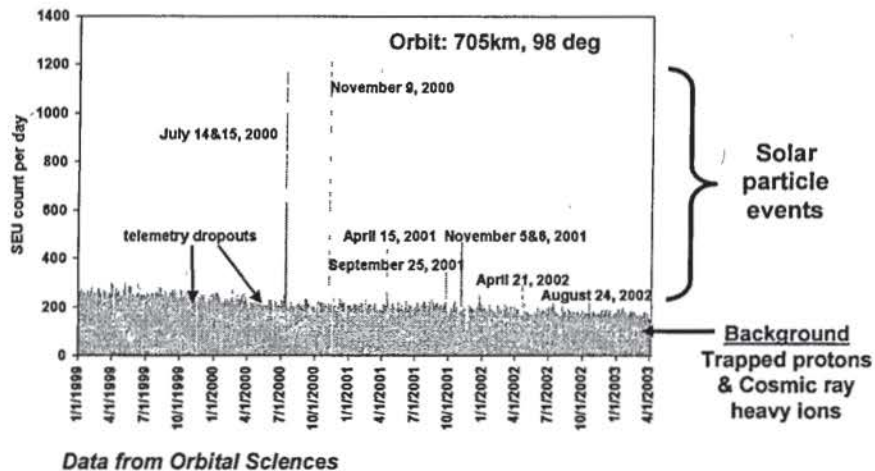
Solar Proton Event - October 1989

Protons & Electrons - Magnetic Field
99% Worst Case Event
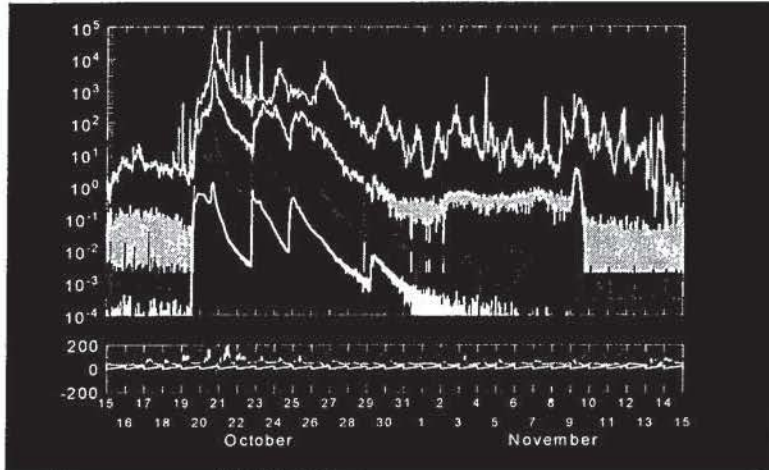
GOES Space Environment Monitor

J. Barth/RADECS Short Course Dry-Run 2009

31

Proton Event Spectra - Cycle 22

Total Integral Proton Fluence

20 Mar 1991
4 June 1991
27 Sept 1991
20 Feb 1994
Aug 1972
19 Oct 1989

Proton Fluence (#/cm²/event)

Energy (> MeV)
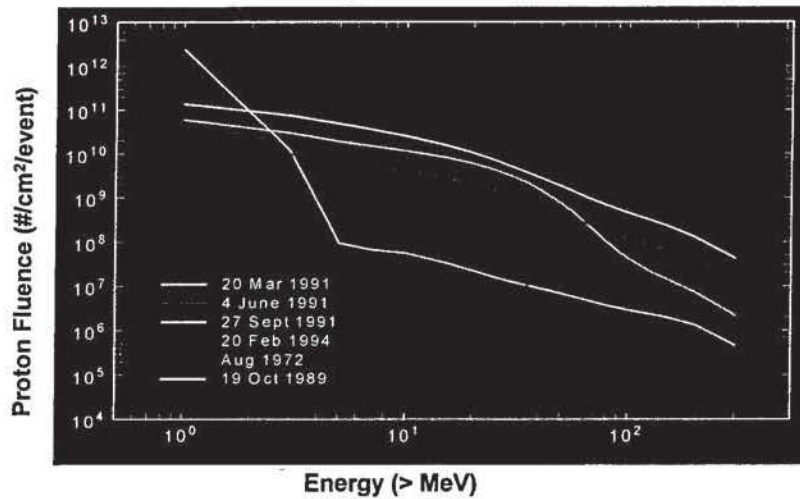
J. Barth/RADECS Short Course Dry-Run 2009

32

Solar Protons: Orbits

Proton Levels Predicted by CREME 96

Plot: Protons (#/cm²/sec/MeV) vs Energy (MeV). Legend: GEO, EOS, I=60deg/H=800 km, LEO.
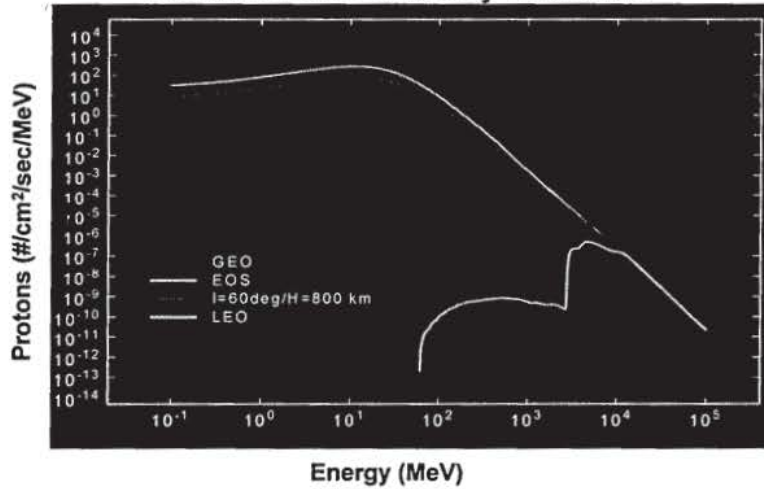
Trapped - Van Allen Belts

- ◆ **Omnidirectional**
- ◆ **Components**
  - » **Protons:**   E ~ .04 - 500 MeV
  - » **Electrons:**   E ~ .04 - 7(?) MeV
  - » **Heavier Ions:**   Low E - Non-problem for Electronics
- ◆ **Location of peak levels depends on energy**
- ◆ <u>**Average**</u> **counts vary slowly with the solar cycle**
- ◆ **Location of populations shifts with time**
- ◆ **Counts can increase by orders of magnitude during magnetic storms**
  - » March 1991 storm - Increases were long term

Upsets Induced by Trapped Protons
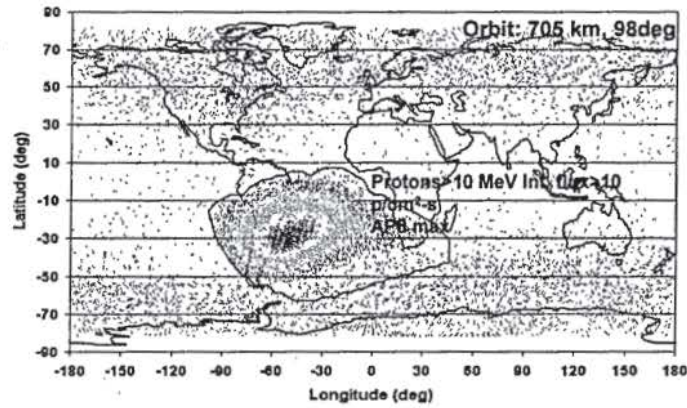
Orbit: 705 km, 98deg

Protons >10 MeV Int. flux >10 p/cm²-s AP8 max

• 1SEU • 1<SEU<10 • 10≤SEU<20 • 20≤SEU<40 • ≥ 40 SEU

Single Event Upsets on Seastar Solid State Recorder – Counts for 4 years

Trapped Particle Motions

Spiral, Bounce, Drift
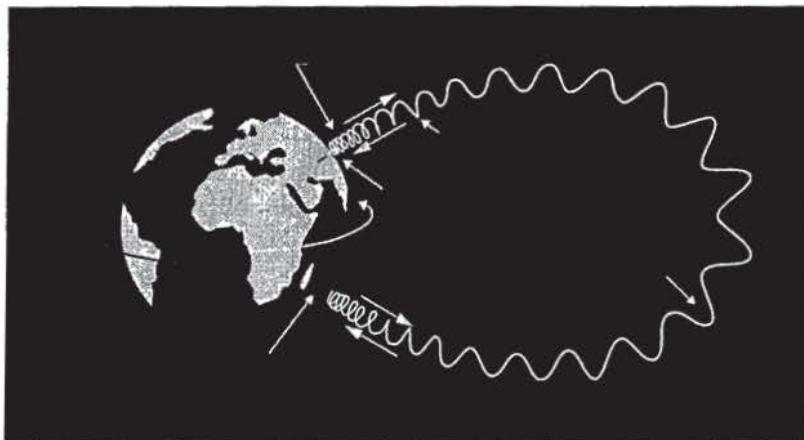
after Hess

Trapped Radiation Belts
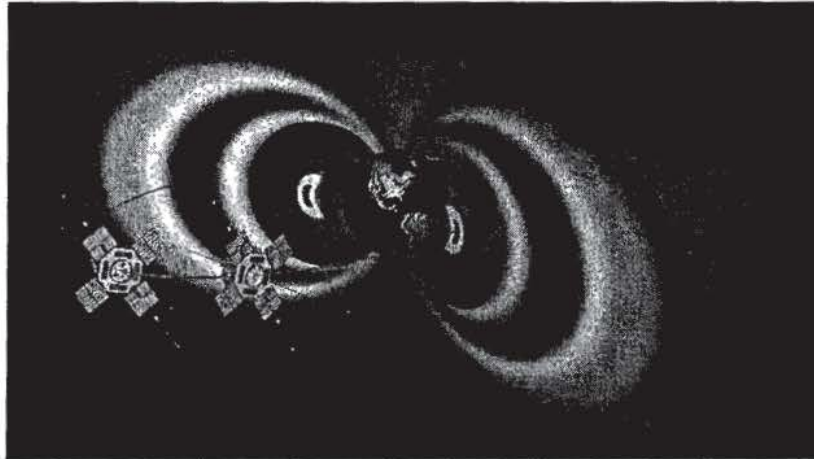
Johns Hopkins University Applied Physics Laboratory

Stable Trapping

◆ **Stable over long periods of time**
  » Range: Inner belts - Years   Outer belts - Minutes
◆ **Due to 4 processes**
  » Injection into the trapping region
  » Particle acceleration
  » Particle diffusion (radial & pitch angle)
  » Particle loss
◆ **Processes can occur simultaneously**
  » Diffusion can result in particle loss
  » Particle acceleration is coupled to diffusion

Stable Does Not Mean Static

Sources ⟵ // ⟶ Losses

- ◆ Outer zone - Solar wind & ionospheric electrons & ions
- ◆ Inner zone - Cosmic ray neutron decay
- ◆ Trapped heavy ions - Interplanetary particles
- ◆ Others
    - » *In situ* acceleration
    - » Artificial, e.g. Starfish explosion

- ◆ Collisions with Earth's atmosphere
- ◆ Collisions with H in the exosphere
- ◆ Collisions with particles in the plasmasphere

⟹ **Short term variations in populations** ⟸

AP8 - MAX Spectra

- ◆ Energy range
    - » .04 - 500 MeV
- ◆ Range in Al:
    - » 30 MeV ~ .17 inch
- ◆ Effects:
    - » Total dose
    - » Single event effects
    - » Solar cell damage

Integral Proton Fluences

MEO
GTO
EOS
LEO
GEO

Fluence (#/cm²/day) vs Energy (>MeV)
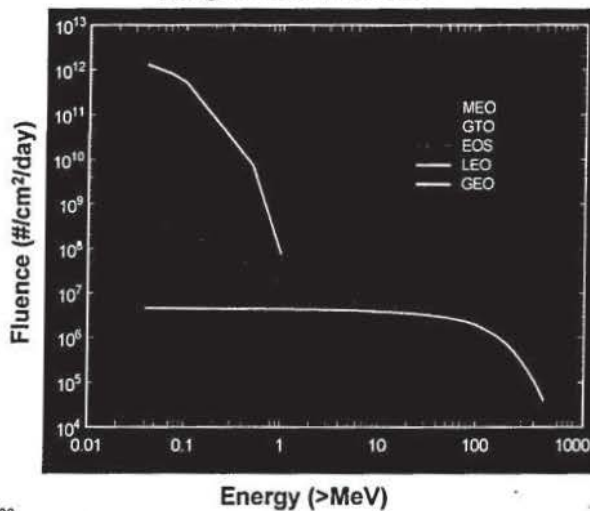
AE-8 - MAX Spectra

Integral Electron Fluences

- ◆ Energy range
  - » .04 - 7 MeV
- ◆ Range in Al:

- ◆ Effects:
  - » Total dose
  - » Surface charging
  - » Deep dielectric charging
  - » Solar cell damage

Fluence (#/cm²/day) vs Energy (>MeV)

GTO
MEO
GEO
EOS
LEO
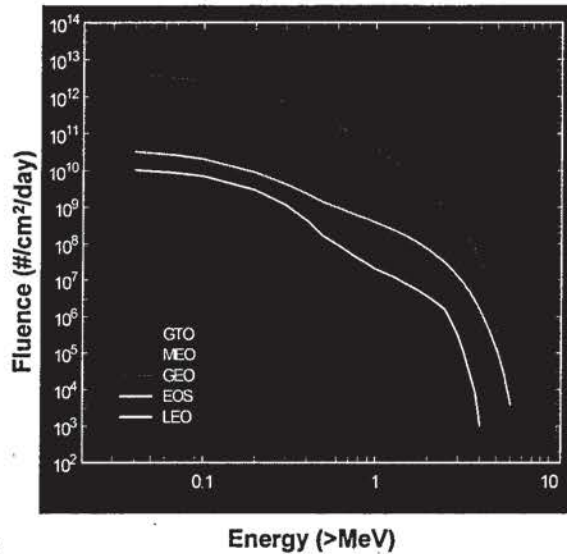
Particle Cascades in Atmosphere

- ◆ Collisions between cosmic rays & atmospheric O & N
- ◆ Important product is neutrons
  - » Single Event Upsets
    - Shuttle
    - Aircraft
    - Ground
  - » Passenger & crew exposure in aircraft
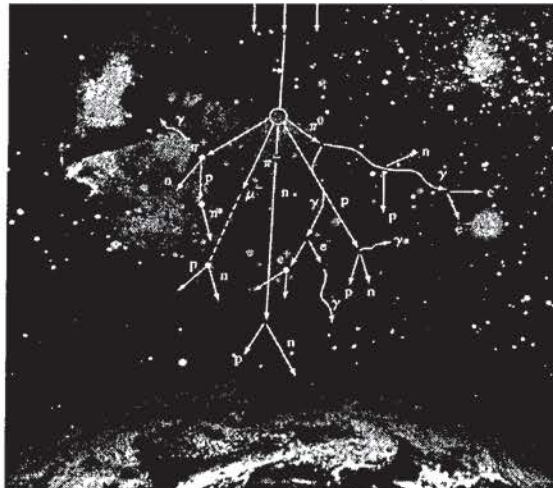
NASA *Neutron Flux Measurements*
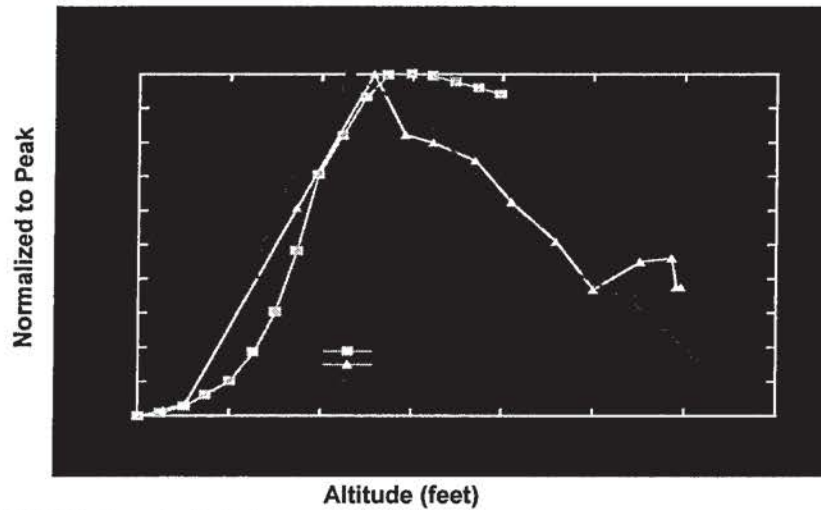
Normalized to Peak

Altitude (feet)

NASA *Outline*

- ◆ **Overview of the Space Environment**
- ◆ **Magnetic Fields and Coordinate Systems**
- ◆ **Particle Populations**
  - » Galactic Cosmic Rays
  - » Solar Particles
  - » Trapped Particles
  - » Atmospheric Neutrons

- ◆ **Dynamics of the Radiation Environment**
  - » Source
  - » Effects
- ◆ **Model Development**
- ◆ **Role of Space Environment Definition in Increasing Reliability**

NASA *Sun: Dominates the Environment*

Source	Modulator
Protons	Galactic Cosmic Rays
Heavy Ions	Atmospheric Neutrons
Trapped Particles	Trapped Particles

NASA *Solar Activity: Cyclic Variation*

◆ **Sunspot cycle discovered in mid 1800s**
◆ **Coronal Mass Ejections (CMEs)**
  » **Increase in solar wind velocity**
  » **Associated with magnetic storms**
  » **Solar particle events - Proton rich**
◆ **Solar Flares**
  » **Increase in solar wind density**
  » **Solar particle events - Heavy ion rich**

The 11-Year Solar Activity Cycle

NASA
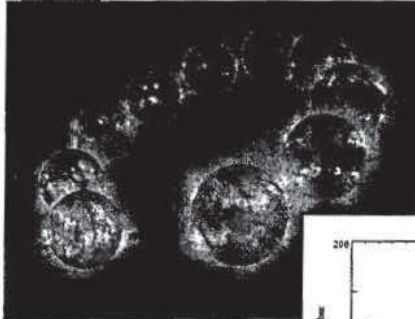
Sunspot cycle discovered by Schwab in 1844

Yearly Averaged Sunspot Numbers 1610-1998

Little Ice Age in 1645 to 1715
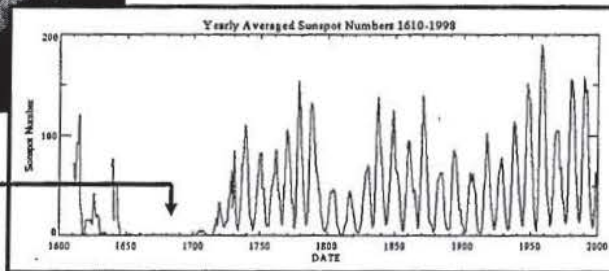
Length varies from 9 - 13 years
7 Years Solar Maximum, 4 Years Solar Minimum

Solar Flares

NASA

- ◆ Sudden brightening near sunspots
- ◆ Solar system's largest explosive events
- ◆ Particles accelerated directly by event
- ◆ Heavy ion rich Solar events

Coronal Mass Ejections

- ◆ Bubble of gas & magnetic field
- ◆ Ejects $\sim 10^{17}$ grams of matter
- ◆ Shock wave accelerates particles to millions of km/hr
- ◆ Associated with magnetic storms
- ◆ Proton rich solar events

Holloman AFB/SOON

TIROS Measurement of Protons

Day Before Coronal Mass Ejection
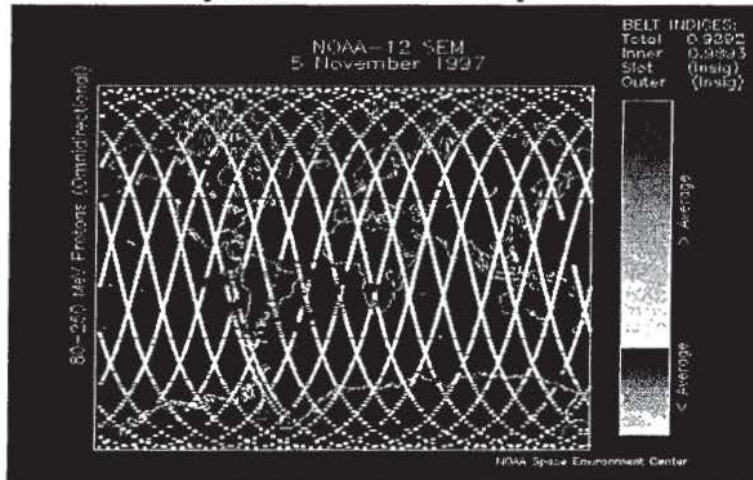
TIROS Measurement of Protons

November 6, 1997 Coronal Mass Ejection
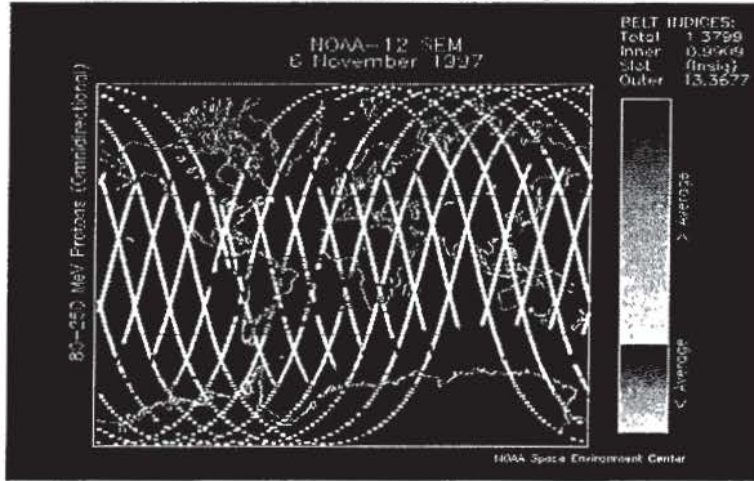
Sunspot Cycle with Solar Proton Events

Proton Event Fluences
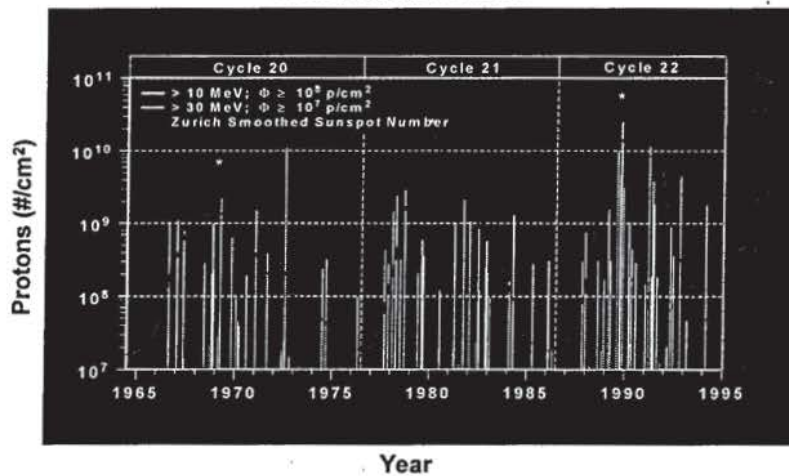
Sunspot Cycle with Magnetic Storms

Sunspots & Magnetic Storm Days

J. Barth/RADECS Short Course Dry-Run 2009   53
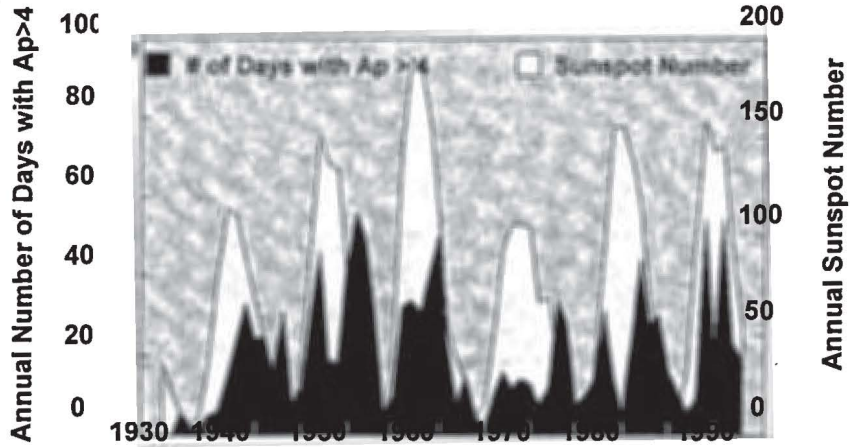
Background vs. Storms – Heavy Ions

CNO - 24 Hour Averaged Mean Exposure Flux

Storms
Solar heavy ions

Background
Cosmic ray heavy ions

J. Barth/RADECS Short Course Dry-Run 2009   54
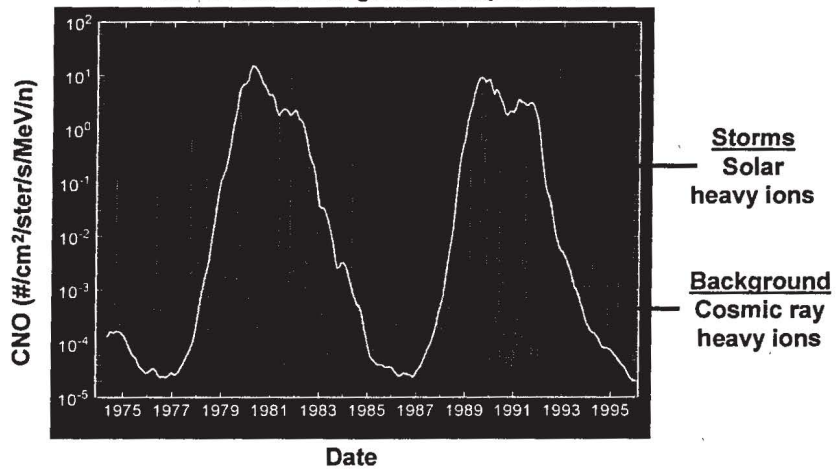
Variations - Protons

- ◆ Fairly stable
- ◆ Cyclic modulations due to the solar cycle ~ 2
  - » Lowest levels are at peak of solar maximum
  - » Highest levels are at lowest point in solar minimum
  - » Rate of change ~ 6%/year
- ◆ Geomagnetic field shift changes location
  - » ~ 6 ° westward / 20 years
- ◆ Anisotropy at inner edge (300-500 km) 2 ~ 7
- ◆ Particle increases at outer edge - New belts
  - » Geomagnetic storms

TIROS/NOAA Trapped Protons

Solar Cycle Variation: 80-215 MeV Protons

Huston et al.
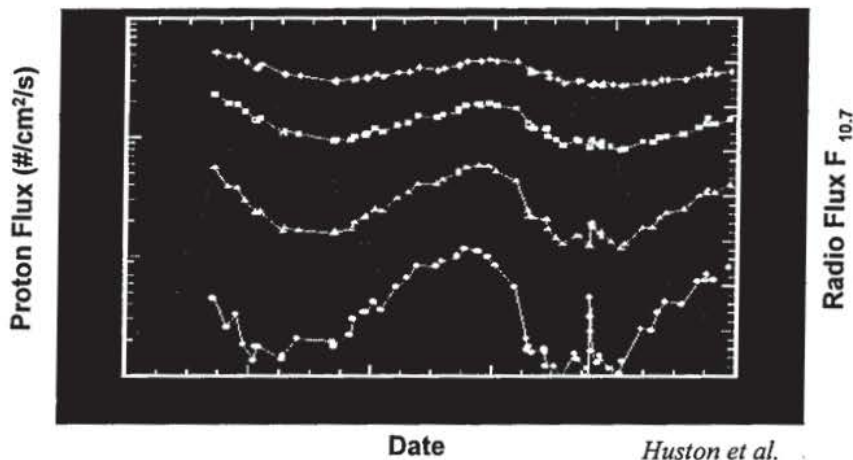
CRRES - Measured Proton Belt

CRRESPRO
Flux
6.94E+02

5.2E+02

3.47E+02

1.70E+02

4.59E+04

#/cm^2/s/MeV
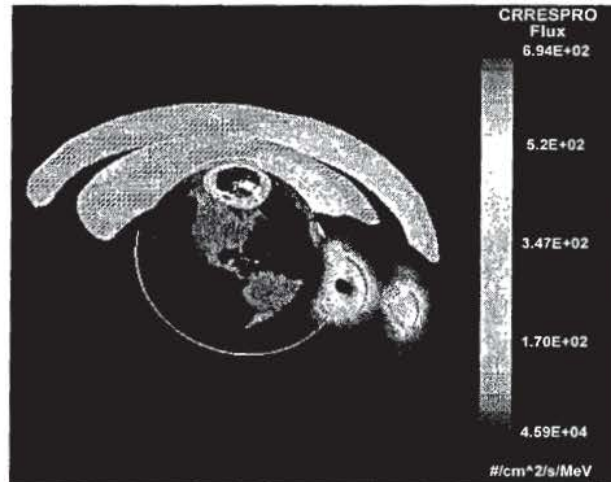
AF Phillips Laboratory, SPD/GD

Variations - Electrons

◆ **Cyclic modulation due to the solar cycle ~ 2**
  » Highest levels are near peak of solar maximum
  » Lowest levels are near lowest point in solar minimum
◆ **Inner zone - Fairly stable**
◆ **Outer zone - Dynamic $10^2 \sim 10^6$**
  » Solar cycle variations are masked
  » Local time Variations due to magnetic field distortion
  » 27-Day variation due to solar rotation
  » Magnetic storms & sub-storms

Activity in the Slot Region - SAMPEX

SAMPEX/P1ADC: Electrons E > 0.4 MeV

Day (1992)
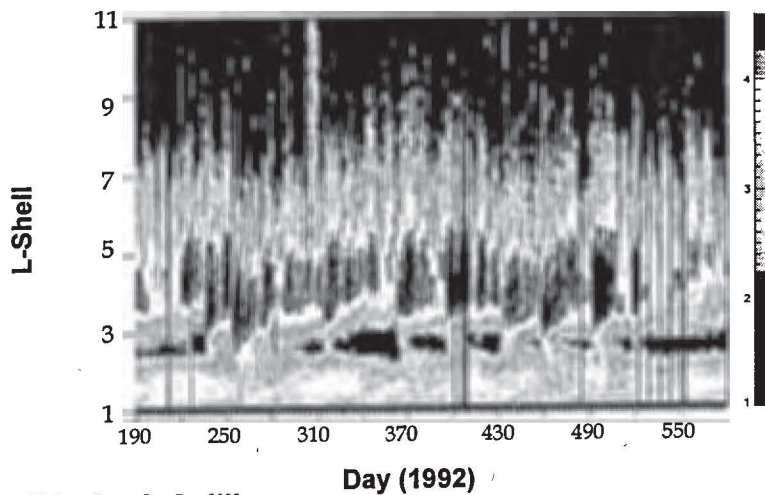
Electron Environment Dynamics

April 2001 Storm ~ 800 km
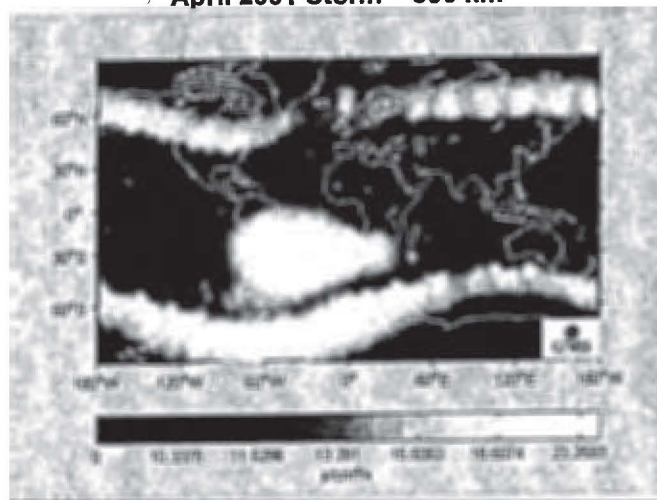
Variations in Neutron Levels

- **Magnetic rigidity determines distribution**
- **Solar cycle modulation**
  - » Function of Galactic Cosmic Ray Levels
    - Solar minimum - Higher
    - Solar maximum - Lower
  - » Measured difference ~ 25%
- **Levels increase with solar events - *Dyer et al.***
- **Dependent on atmospheric conditions**
- **Very penetrating - Aircraft shielding reduces levels by ~ 10%**

Outline

- **Overview of the Space Environment**
- **Magnetic Fields and Coordinate Systems**
- **Particle Populations**
  - » Galactic Cosmic Rays
  - » Solar Particles
  - » Trapped Particles
  - » Atmospheric Neutrons

- **Dynamics of the Radiation Environment**
  - » Source
  - » Effects
- **Model Development**
- **Role of Space Environment Definition in Increasing Reliability**

Galactic Cosmic Ray Models

De facto standard is CREME86

- Galactic Cosmic Ray (GCR) Model from Moscow State University (MSU)
  - » Solar variation is modeled with diffusion-convection theory of solar modulation
- Cosmic Ray Effects in MicroElectronics (CREME96)
  - » CREME86 was updated with the GCR MSU Model
- NASA GCR Model from Badhwar and O'Neill
  - » Similar approach to GCR MSU model with different implementation of the solar modulation theory
- New approach by Davis et al. at the California Institute of Technology (CIT)
  - » Uses transport model for the GCRs through the galaxy preceding the penetration and subsequent transport in the heliosphere

---

GCR LET: CREME 96 - CREME 86

GEO: Solar Minimum, 100 mils (2.54 mm) Al

LET (MeV-cm²/mg)
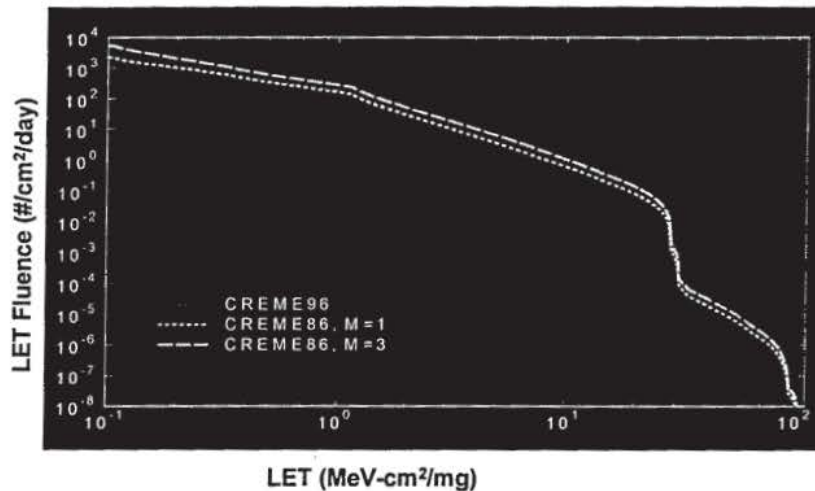
Comparison of NASA, MSU, CIT Models with ACE Instrument Data
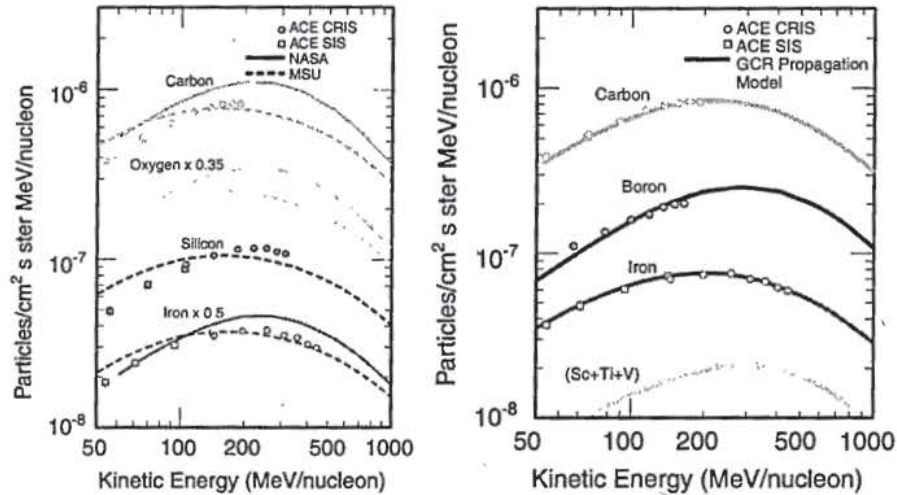
Solar Proton Models

De facto standard is JP91 for cumulative fluence, CREME86/96 for worst case event fluence

◆ Solar Particle Event Fluence Model (SPE Fluence Model)
  » Nymmik et al. sponsored by Moscow State University
  » Based on power function distributions of event fluences
◆ Emission of Solar Proton Model (ESP)
  » Xapsos et al. sponsored by NASA
  » Based on satellite data from the 21 solar maximum years during solar cycles 20-22
  » Uses Maximum Entropy Principle to generate an optimal selection of a probability distribution, and Extreme Value theory to estimate worst case
  » Calculates cumulative and worst case solar proton fluences
◆ PSYCHIC
  » Xapsos et al. sponsored by NASA
  » ESP Model with satellite data set extended to cover the time period of 1966 – 2001
  » Energy range extended to over 300 MeV
  » Includes estimates for solar minimum spectra

Comparison of Solar Proton Models
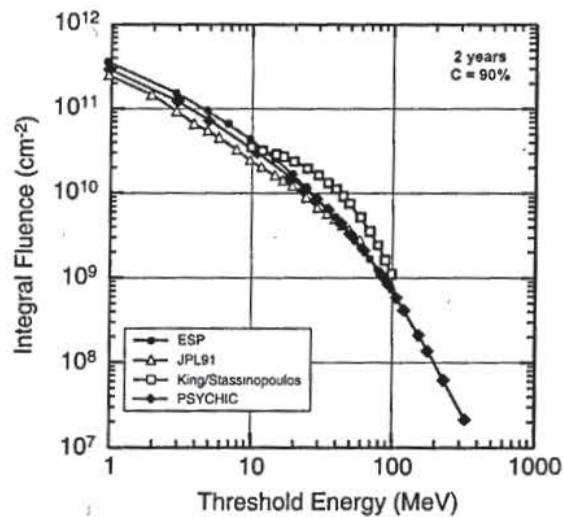
Solar Heavy Ion Model

De facto standard is CREME86/96 for worst case event fluences

- ◆ **CRRES/SPACERAD Heavy Ion Model of the Environment (CHIME) – Chenette et al. sponsored by US AFRL**
  - » Heavy ion abundances scaled to protons results in overestimates
- ◆ **Modeling and Analysis of Cosmic Ray Effects in Electronics MACREE) – Majewski at al. sponsored by Boeing**
  - » Heavy ion abundances scaled to alphas results in less conservative estimates
- ◆ **CREME96**
  - » Uses the October 1989 event as a worst case
  - » Most extensive heavy ion measurements are for C, O, and Fe, and remaining elemental fluences are determined from a combination of measurements in 1 or 2 energy bins and abundance ratios

Comparison of CREME96 to CREDO Measurements During 2000 and 2002
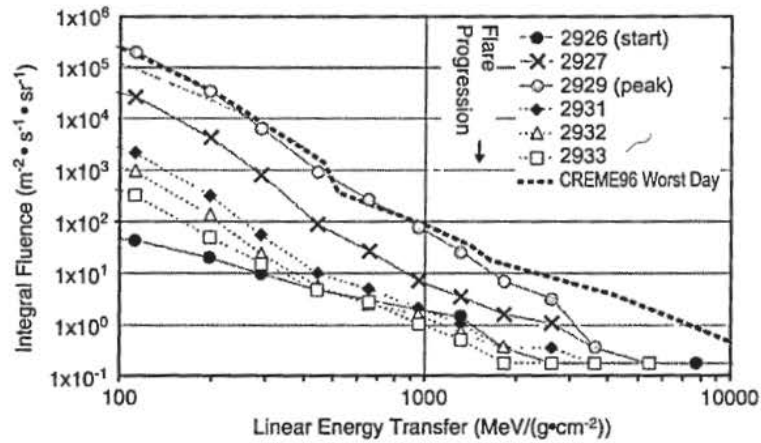
Data Courtesy of C. Dyer/QinetiQ

PSYCHIC Heavy Ion Model

Model Name	Measurement Period	Energy Range (MeV/n)	Data Source
Alpha Particles	1973-2001	$1 < E < 200$	IMP-8, GOES
C, N, O, Ne, Mg, Si, S, Fe	1997-2005	$0.2 < E < 5.9$	ACE/SIS
Less prevalent elements	-	-	Abundance model

- Model is published
- Looking for funding to develop interface

Xapsos et al.

Proton Belt Models

De facto standard is AP-8

♦ **Combined Release and Radiation Effects Satellite PROton Model (CRRESPRO)**
  » Brautigam et al. sponsored by US Air Force Research Laboratory (AFRL)
♦ **Low Altitude Trapped Radiation Model (LATRM)**
  » Huston et al. sponsored by NASA
♦ **Trapped Proton Model-1 (TPM-1)**
  » Huston et al. sponsored by NASA and AFRL
♦ **SAMPEX/PET Model (PSB97)**
  » Heynderickx et al. sponsored by ESA

Coverage of New Proton Models

Model Name	# of Years of Data	Spatial Coverage	Energy Range (MeV)	Data Source
CRRESPRO	1.2	$1.15 < L < 5.5$	$1 < E < 100$	CRRES
LATRM	17	< 1000 km	$16 < E < 80$	TIROS/NOAA
TPM-1	Depends on Region	$1.15 < L < 5.5$	$1 < E < 100$	CRRES, TIROS/NOAA
PSB97	4	$1.1 < L < 2.0$	$18.5 < E < 500$	SAMPEX

• **Note that combining the TPM and PSB97 models with an update of data taken with the SAMPEX/PET instrument would result in a fairly complete trapped proton model.**

Comparison of Trapped Protons Models
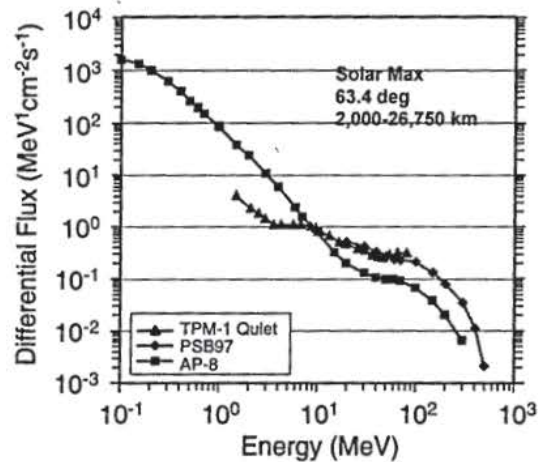
Electron Belt Models

De facto standard is AE-8

◆ **Combined Release and Radiation Effects Satellite ELEctron Model (CRRESELE)**
  » Gussonhoven et al. sponsored by Air Force Research Laboratory (AFRL)
◆ **FLUx Model for Internal Charging (FLUMIC)**
  » Wrenn et al. sponsored by ESA
◆ **Particle ONERA-LANL Environment Model (POLE)**
  » Bourdarie et al. sponsored by ONERA, Los Alamos National Laboratory (LANL), and NASA

Coverage of New Electron Models

Model Name	# of Years of Data	Spatial Coverage	Energy Range (MeV)	Data Source
CRRESELE	1.2	$2.5 < L < 6.8$	$0.5 < E < 6.6$	CRRES
FLUMIC	11	Outer Zone	$0.2 < E < 5.9$	Various
POLE	25	Geostationary	$0.03 < E < 6.0$	LANL Instruments

- Volatile nature of the outer zone electron regions suggests that probabilistic models may be useful, but they are relatively unexplored
- Worst case approaches are used to define severe electron environments

Comparison of Trapped Electron Models
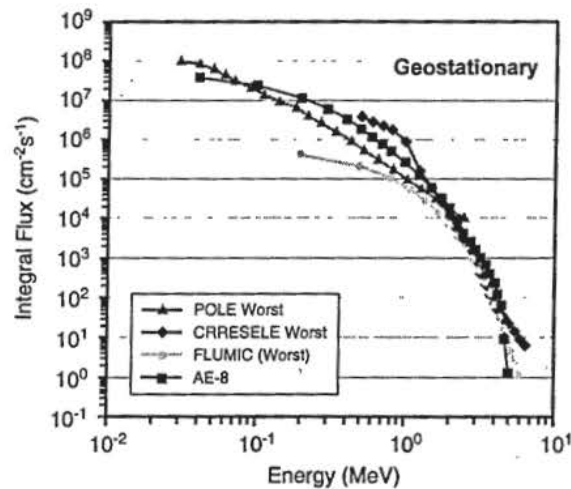
2 Models

- ◆ Boeing
  - » Function of Latitude, Altitude, and Energy
  - » Based on Studies by Mendall, Korff, and Armstrong
  - » Easy to Use
  - » Accurate
- ◆ Wilson-Nealy
  - » Function of Magnetic Rigidity & Atmospheric Depth
  - » More Accurate
  - » Includes Solar Cycle Modulation

Neutron Models: Flux vs. Altitude

1-10 MeV Atmospheric Neutron Flux
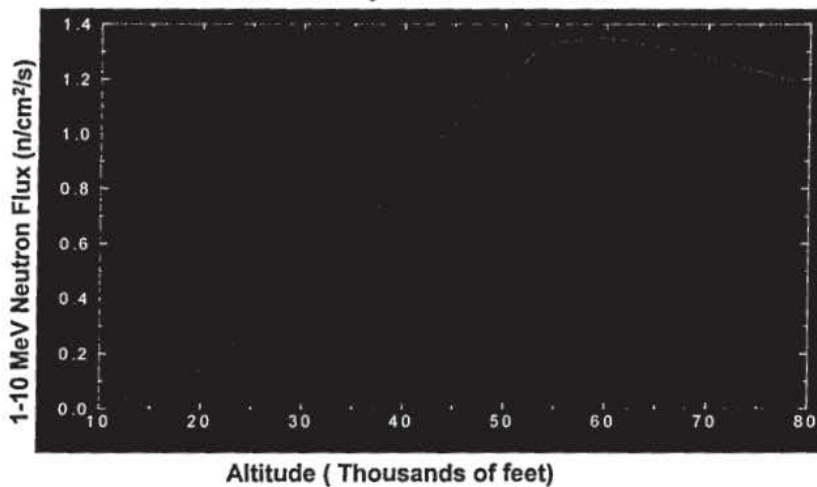
Neutron Model: Flux vs. Latitude

1-10 MeV Atmospheric Neutron Flux

J. Barth/RADECS Short Course Dry-Run 2009

79
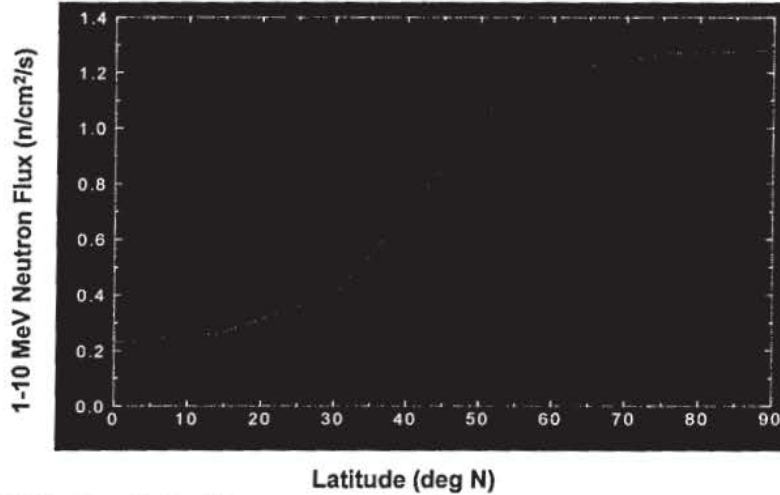
Neutron Model: Flux vs. Energy

Differential Neutron Flux - Atmospheric
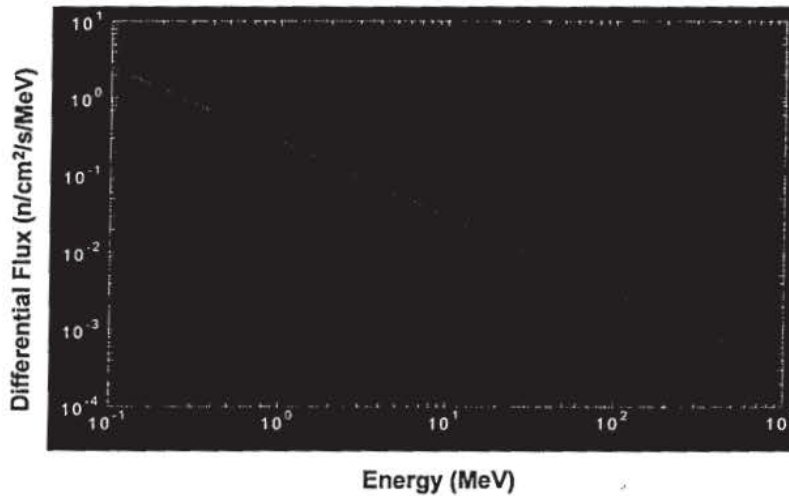
J. Barth/RADECS Short Course Dry-Run 2009

80

Outline

- ◆ **Overview of the Space Environment**
- ◆ **Magnetic** Fields and Coordinate Systems
- ◆ **Particle Populations**
  - » Galactic Cosmic Rays
  - » Solar Particles
  - » Trapped Particles
  - » Atmospheric Neutrons

- ◆ **Dynamics of the Radiation Environment**
  - » Source
  - » Effects
- ◆ **Model Development**
- ◆ **Role of Space Environment Definition in Increasing Reliability**

Space Environment Model Use in Spacecraft Life Cycle

Mission Concept

Mission Planning } **Space Climate** **Minimize Risk**

Design

Launch

Operations } **Space Weather** **Manage Residual Risk**

Anomaly Resolution ⟶ Both

+

in situ measurements
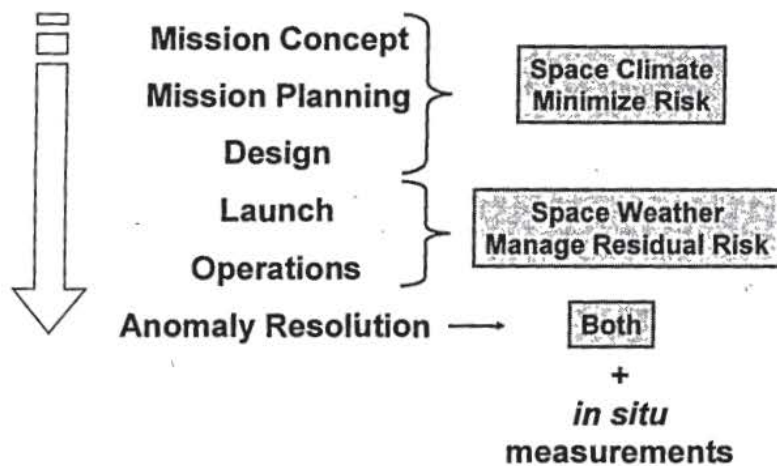
Pre-Launch Phases: Climatology

◆ **Mission Concept**
   » Observation requirements & observation vantage points
   » Development and validation of primary technologies

◆ **Mission Planning**
   » Mission success criteria, e.g., data acquisition time line
   » Architecture trade studies, e.g., downlink budget, recorder size
   » Risk acceptance criteria

◆ **Design**
   » Component screening, redundancy, shielding requirements, grounding, error detection and correction methods

Launch & Post-Launch: Space Weather

◆ **Launch & Operations**
   » Asset protection
      - Shut down systems
      - Avoid risky operations, such as, maneuvers, system reconfiguration, data download, or re-entry

◆ **Anomaly Resolution**
   » Lessons learned need to be applied to <u>all</u> phases

Questions?

Dry Run Version

2009 RADECS Short Course

Session 1: The Evolution of the Radiation Environments

Janet L. Barth
NASA/Goddard Space Flight Center

9 June 2009

Table of Contents

1 Introduction

Spacecraft are exposed to a multitude of environments that are not present at the surface of the Earth, including micrometeoroids and orbital debris, ultraviolet irradiation, neutral particles, cold and hot plasma, and particle radiation. The interaction of the space environments with spacecraft systems cause degradation of materials, thermal changes, contamination, excitation, spacecraft glow, charging, communication and navigation errors and dropouts, radiation damage, and induced background interference (see Table 1.1). This session will focus on the high-energy radiation environments that cause radiation damage (total dose and displacement damage) and single events effects.

The complex space radiation environments consist of 1) particles trapped by planetary magnetospheres in "belts", including protons, electrons, and heavier ions 2) interplanetary particles which include protons and heavy ions of all of the elements of the periodic table, and 3) primary and secondary particles in the atmospheres of planets. We will see that since the early 1960's efforts to understand the radiation environment and its variations often went hand in hand with requirements generated by the mission goals of our agencies. Modeling efforts may also be prompted by the availability of a new set of measurements or a scientific discovery that adds to our understanding. A third driver for model development activities is the emergence of new, critical radiation effects and mechanism issues as the radiation sensitivity of technologies change. More challenging mission requirements and the increase in sensitivity of the technologies that meet those requirements drive the need for radiation environment models that predict the environment with finer spatial resolution, better temporal fidelity, smaller error margins, and sometimes models that forecast the environment.

Lacking a standardization process for environment models, *de facto* model standards have been adopted by the space community for space radiation environment models. The following models have been "generally" accepted as *de facto* standards:

- AP-8 and AE-8 for radiation belt protons and electrons and plasma
- JPL91 for solar protons
- CREME86 for galactic cosmic rays and solar heavy ions

The space system design and radiation health communities have identified three concerns related to *de facto* standard models: the models are not adequate for modern applications, data that have become available since the creation of the models are not being fully exploited for modeling purposes, and when new models are produced, there is no authorizing organization identified to evaluate the models or their data sets for accuracy and robustness.

Several well known problems with the current models have been identified. The AP-8 and AE-8 models of the radiation belts have very poor time resolution, there are large uncertainties in some regions, environment definitions do not exist for some energy ranges, and contemporary applications require descriptions for a wider range of climatological conditions, i.e., averages and worst case are insufficient. For the interplanetary models, the galactic cosmic ray model in CREME86 does not represent solar modulation accurately, the JPL91 has limited energy spectrum definition in the high energy regime, and the solar heavy ion models in CREME86 overestimate worst case fluences. In the past few years, the modeling and user community have met together to define model deficiencies, review interim models and develop requirement for the new models.

The objective of this session of the Short Course is review the development of the "de facto" models, to provide information on interim models, and to describe efforts to standardize and develop new models of the radiation environment. The first section will give an overview of the structure and composition of the space environment. Next, the coordinate systems used to define the radiation environments will be provided as tools to understand the origins, magnitudes, and distributions of the high-energy radiation environment. More complete discussions can be found in previous publications [1, 2, 3, and 4]. Section 3 will give a background on magnetic fields and coordinates systems used to model and define radiation environments. Sections 4, 5, and 6 will describe the discovery, origins, and composition of the particle populations that are a concern for spacecraft design and operations. Section 7 will discuss the dynamics of the radiation environment and review the impacts on the levels and distribution of the environments in space. Section 8 will review the history and current state of the art of radiation environment model development. Section 9 will discuss the requirements for descriptions of the radiation environment that can meet the needs of system designers and operators through all phases of the life cycle of spacecraft development and operation.

2 Overview of the Space Environment

The purpose of Section 2 is to provide a context of the space environment where radiation populations originate and evolve, i.e., the solar wind, interplanetary space, the Earth's magnetosphere and atmosphere, and our heliosphere. Subsequent sections will describe how the space environment components interact and impact each other.

2.1 Solar Wind

The sun's outer atmosphere, the corona, extends several solar diameters into interplanetary space. The corona continuously emits a stream of protons, electrons, doubly charged helium ions,

3

and small amounts of other heavy ions, collectively called the solar wind. The high temperature of the corona inputs sufficient energy to allow electrons to escape the gravitational pull of the sun. The result of the electron ejections is a charge imbalance resulting in the ejection of protons and heavier ions from the corona. The ejected gas is so hot that the particles are homogenized into a dilute plasma*. The energy density of the plasma exceeds that of its magnetic field so the solar magnetic field is "frozen" into the plasma. The electrically neutral plasma streams radially outward from the sun at a velocity of approximately 300 to 900 kilometers per second with a temperature on the order of 104 to 106 K. The energies of the particles range from approximately 0.5 to 2.0 keV/nucleon. The average density of the solar wind is 1 to 30 particles/cm^3.

2.2   High-energy Interplanetary Particles

In addition to the solar wind plasma, interplanetary space contains high-energy charged particles called galactic cosmic rays (GCRs) that are present at all times. Solar events that occur sporadically (coronal mass ejections and flares) are also a source of high-energy particles.

During active phases of the solar cycle, the numbers and intensity of coronal mass ejections and solar flares increases. These events can cause periodic increases in the levels of interplanetary particles that are orders of magnitude higher than the GCR environment. The particles consist of ions of all elements but protons usually dominate the abundances. Solar particles diffuse as they move through the interplanetary medium. Therefore, the solar particles abundances are a function of radial distance from the Sun.

2.3   Earth's Magnetosphere

The Earth's magnetosphere (see Figure 2.3.1) is a cavity formed by the interaction of the Earth's magnetic field and the solar wind. In the absence of the solar wind, the Earth's magnetic field would be shaped like the field of a bar magnet; non-varying, nearly symmetric about the magnetic axis, extending outward to long distances, and open at the poles. The bar magnet representation is accurate up to altitude of 4 to 5 Earth radii. The solar wind plasma, with its embedded solar magnetic field, compresses the geomagnetic field until there is balance between the magnetic pressure from the Earth and the momentum pressure from the solar wind forming a "bow shock". On the dayside, during moderate solar wind conditions, the magnetosphere terminates at the magnetopause at ~10 Earth radii altitude. At the location of this "collisionless" shock, the solar wind plasma cannot penetrate deeply into the geomagnetic field because of its charged particle composition. In fact, 99.9% of the solar wind particles pass around the Earth's

---

* Plasma is ionized gas in which electron and ion densities are approximately equal. Plasma is distinguished from the energetic particle population in that it does not cause radiation effects and has energies < 100 keV.

4

magnetosphere. The flow of the solar wind around the flanks of the magnetopause stretches the geomagnetic field in the anti-solar direction into a long tail of up to ~300 Earth radii altitude. Some tail field lines are not closed and are connected to the solar magnetic field embedded in the solar wind.

The magnetosphere is filled with plasma that originates from the ionosphere and the solar wind. The plasmasphere is at low and mid latitudes in the inner magnetosphere, and the plasma sheet resides in the magnetotail. Overlapping the plasmasphere and the plasma sheet are the high-energy radiation belts. Charged particles become trapped because the Earth's magnetic field constrains their motion. They spiral around the field lines in a helicoidal path while bouncing back and forth between the magnetic poles. Superimposed on these spiral and bounce motions is a longitudinal drift of the particles.

The radiation belts consist of protons, electrons and heavier ions. The trapped electrons have energies up to 10s of MeV, and the trapped protons and heavier ions have energies up to 100s of MeV. These particles have complex spatial distributions that vary by several orders of magnitude depending on orbit inclination and altitude. The sun is a driver for long and short-term variations in the locations and levels of trapped particles. A feature of the Earth's trapped radiation belts is the South Atlantic Anomaly (SAA). The 11° angle between the magnetic and geographic axes and the offset of the geographic and geomagnetic centers of the Earth cause a depression in the magnetic field in the South Atlantic. This magnetic field sink causes charged particles to be trapped at low altitudes (<1000 km) in that region thereby forming the SAA.

2.4   Earth's Atmosphere

As galactic cosmic ray and solar particles enter the top of the Earth's atmosphere, they are attenuated by interaction with nitrogen and oxygen atoms. The result is a "shower" (see Figure 2.4.1) of secondary particles and interactions created through the attenuation process. Products of the cosmic ray showers are protons, electrons, neutrons, heavy ions, muons, and pions. For the radiation effects community, the most important product of the cosmic ray showers is the neutrons because of their ability to cause single event upsets in aircraft avionics.

2.5   Heliosphere

As the solar wind streams supersonically outward from the Sun's corona through the solar system, it pushes against the plasma and fields of the interstellar medium (the hydrogen and helium gas that permeates the galaxy), forming a large bubble called the heliosphere (Figure 2.5.1). On the inside of this bubble is the interplanetary medium most of which emanates from the Sun and beyond is the interstellar medium.

Interstellar ions and neutral atoms flow at 26 kilometers per second relative to the Sun. The solar wind, flowing outward at 300 to 900 kilometers per second, makes a transition to subsonic flow at the termination shock. Beyond this, the solar wind is turned toward the heliotail, carrying with it the spiraling interplanetary magnetic field. The heliopause separates solar material and magnetic fields from interstellar material and magnetic fields. Interstellar neutral atoms and higher-energy galactic cosmic rays can penetrate the heliosphere, but interstellar ions are diverted around it. Beyond the heliopause there may also be a bow shock formed in the interstellar medium.

The size of the heliosphere is determined by a balance between the solar wind pressure and the unknown pressure contributions from interstellar gas, magnetic fields, small dust grains, and low-energy cosmic rays. The solar wind pressure decreases as the solar wind expands. Once it becomes comparable to the interstellar pressure the solar wind makes a transition to subsonic flow at the "termination shock." Although there are presently no direct measurements of the size of the heliosphere, a combination of theory, modeling, and a few key measurements leads to the conclusion that the termination shock is presently located between ~80 and ~100 astronomical unit* (AU) from the Sun. In this case, the heliopause (the boundary between solar wind and interstellar plasmas) is expected to be somewhere between ~120 and ~150 AU. At > 100 AU away from the Sun, the Voyager 1 spacecraft has passed the termination shock of the heliosphere and is approaching interstellar space. [5]

3   Magnetic Fields and Coordinate Systems

The Earth's magnetosphere determines the penetration and distribution of charged particles in the near-Earth regions. The motion of a charged particle is a consequence of the forces acting on it as the particle moves through a non-uniform magnetic field. To understand the distribution of and variations in the particle environment, it is necessary to first have a basic knowledge of magnetic field models and the magnetic coordinate systems that best represent particle behavior.

3.1   Earth's Magnetic Field

The Earth's magnetic field, B, originates primarily within the Earth's interior with a small part produced by the ionosphere and the magnetosphere. Approximately 90% of the Earth's magnetic field can be represented as a dipole, offset slightly from the center of the Earth and inclined 11° from the rotational axis. Hence, the north magnetic pole is located at about 76° north

---

* An astronomical unit (abbreviated as AU, au, a.u., or sometimes ua) is a unit of length based on the mean distance from the Earth to the Sun (nearly 150 million kilometers or 93 million miles).

latitude and 100° west longitude, and the south magnetic pole is at approximately 66° south latitude and 139° east longitude. The magnetic field strength is measured in nanoteslas (nT)* and varies from a few nT at high altitudes to over 50,000 nT at low altitude, high latitude locations.

In reality, the internal component of the geomagnetic field (often referred to as the "main field") is only quasidipolar due to convection currents in the Earth's core and varies slowly with time due to changes in the core. Its intensity decreases by about 6% every 100 years and the magnetic dipole moment (~ 30,200 nT) decreases by about 20 nanoteslas per year.

The International Geomagnetic Reference Field (IGRF) is a series of mathematical models of the internal geomagnetic field and its secular variation. The first IGRF model, IGRF 1965, was adopted by the International Association of Geomagnetism and Aeronomy (IAGA) in 1968. Several revisions or updates have been issued. Newer versions of the IGRF included the Definitive Geomagnetic Reference Fields (DGRFs) issued in 5-year epochs [6]. In addition to the DGRF/IRGF model suite, the Jensen and Cain and GSFC12/66 models are used to calculate the magnetic field for some trapped particle models [7,8].

At higher altitudes where the main field is lower, it is important to include the contribution of the external field in the total field strength. The external magnetic field is the sum of the fields transported by the solar wind and those, which the solar wind induces in the magnetosphere. The Earth, with its atmosphere and main magnetic field, rotates and moves in its orbit around the Sun resulting in periodic variations in the gravitational force, solar illumination, compression, and modifications from solar wind effects. These motions yield diurnal and seasonal variations in the external field. Also, changes in the interplanetary environment, mostly caused by the Sun, result in "disturbance" field variations. The magnitude of the variations depends on the degree of perturbation in the magnetosphere.

The total geomagnetic field value is obtained by a vector addition of the internal and external field components, B_x, B_y, and B_z (when using a Cartesian coordinate system). When most of a spacecraft's orbit is spent in regions where L < 4 (see Section 3.2 for a definition of L), it is not necessary to include external field contributions because they are much smaller than the internal field. The external field component with the effects of magnetic storms on the particle environment calculations should be evaluated for spacecraft that spend most of their time in regions in the magnetosphere where L > 4. The external field model most commonly used is available from the author, Nikolai Tsyganenko [9]. Figure 3.1.1 shows the magnetic field lines calculated with the internal and external field models.

---

*1 nanotesla = 1 gamma = 10^{-5} gauss

7

3.2   B-L Coordinate System

A major contributor to the space radiation hazard is the trapped charged particles. A detailed explanation of their behavior and distribution in space is given in Section 5. A brief description of their basic motion will be given here to provide sufficient background to define the coordinate system that is used to map them in space.

Charged particles become trapped because the Earth's magnetic field constrains their motion. They spiral around the field lines in a helicoidal path while bouncing back and forth between the magnetic poles. Superimposed on these spiral and bounce motions is a longitudinal drift of the particles because of the gradient of the magnetic field. Figure 3.2.1 illustrates the three motions. When the particle makes a complete azimuthal rotation, it has traced a "drift shell". (see Figure 3.2.2)

Mapping trapped charged particles requires consideration of multiple dimensions including species, energy, pitch angle[*], altitude, latitude, and longitude. Mapping can be greatly simplified by reducing one or more of the parameters. Carl McIlwain accomplished this when he developed the dipole shell parameter, L. In early attempts to map trapped particles in space, it was found that the location of the particle could be reduced from a three dimensional system (latitude, longitude, and altitude) to a two dimensional system. The two coordinates of the McIlwain system are rings of constant magnetic field strength, B, and the dipole shell parameter, L. The L parameter is most simply described as the value that marks the particle drift shells by their magnetic equatorial distance from the center of the Earth.

The B-L coordinate system is defined in terms of geomagnetic coordinates. If the Earth's magnetic field is viewed as a simple dipole, the dipole axis is offset from the rotational axis by 11°. When dipole field lines and particle drift shells are defined in terms of latitude and longitude, it is in the geomagnetic coordinate system.

To gain an understanding of the L parameter, it is useful to define L in terms of a dipole field. Figure 3.2.3 illustrates a magnetic field line where K_0 is the magnetic dipole moment, λ is the geomagnetic latitude; and R is the radial distance to point B on the field line. R_0 is the radial distance to the field line where it crosses the magnetic equator. The field line can be mapped by:

$$R = R_0 \cos^2 \lambda \quad (3.1)$$

The parameter L is defined as:

$$L = \frac{R_0}{R_E} \quad (3.2)$$

---

[*]The pitch angle α of a particle is the angle between the field vector B and the velocity vector v. When $\alpha = 90°$, all of the motion is perpendicular to the field line and when $\alpha = 0°$, the particle moves in a straight line parallel to the field line.

where R_E = 6371 km, the radius of the Earth. Note that although positions on the field line move closer to the Earth as the latitude increases, the L value remains the same. In other words, high L values are calculated for low-earth polar orbits in the high latitude regions.

In the dipole field, the field magnitude B is:

$$B = \frac{K_0}{R_0^3} \frac{\sqrt{4 - 3\cos^2 \lambda}}{\cos^6 \lambda} \quad (3.3)$$

In reality, the field is not a dipole and the calculation of B and L for a given position in space is more complicated. The magnetic field strength for any point in space can be calculated using the internal and external field models described in Sections 3.1 and performing a vector addition on the components to obtain the total field strength. The local L is then calculated from the geomagnetic field strength:

$$L^3 = \frac{M}{B_p} F\left(I^3 \frac{B_p}{M} \right) \quad (3.4)$$

where M is the magnetic dipole of the Earth and B_p is the magnetic field strength at point P. F is a function which is not analytic but can be approximated numerically [10] and

$$I = \int_P^{P'} \sqrt{1 - \frac{B}{B_p}} \, ds \quad (3.5)$$

where B and ds are the magnitude of the field and the arc distance along the line of force. Note that L is independent of geomagnetic longitude. A set of computer codes is available to perform these calculations [11] and can be obtained from NASA/Goddard's National Space Science Data Center (NSSDC).

3.3   Magnetic Rigidity and Geomagnetic Attenuation

The Earth's magnetic field provides some protection to Earth-orbiting spacecraft from interplanetary particles by deflecting the particles as they impinge upon the magnetosphere. The exposure of a spacecraft primarily depends on the inclination and, secondarily, the altitude of the trajectory. For example, interplanetary particles have free access over the polar regions where field lines are open to interplanetary space. The penetration power of these particles is also a function of the particle's energy and ionization state and of solar wind and magnetospheric conditions. Analysis of the exposure of spacecraft orbiting the Earth as a function of the geomagnetic disturbances that are often associated with solar events is especially critical. For example, Susan Gussenhoven *et al.* [12] showed with data from the Combined Release and Radiation Effects Satellite (CRRES) that solar protons reached L shell values as low as 2.

Charged particles that have a low momentum per unit charge are deflected at a certain depth in the magnetosphere and are cut off. The magnetic rigidity of a charged particle is defined as the

momentum per unit charge and is measured in units of electron volts/number of charge units, i.e., volts. The gigavolt or GV is a convenient unit for this application. Charged particle cutoffs are a function of geomagnetic latitude, altitude, and the zenith and azimuthal directions and energy of the incident particle. There is an upper L shell cutoff above which particles are allowed, a lower cutoff below which particles cannot penetrate (forbidden regions), and a penumbral region where the transmission of the particles is chaotic [13]. The penumbral region, between the upper and lower cutoffs, complicates the calculations of cutoff values.

Carl Störmer [14] derived the following equation for particle cutoff rigidity, r_s, at the Earth's surface in a dipole field:

$$r_s = \frac{M}{R^2}\left[\frac{\cos^4 \lambda}{\left(1+\sqrt{1-\sin\varepsilon\sin\phi\cos^3\lambda}\right)^2}\right] \quad (3.6)$$

where λ is the geomagnetic latitude, ε is the zenith angle, ϕ is the azimuthal angle measured from the north magnetic axis, M is Earth's dipole moment, and R is the distance from the dipole center of the Earth in units of Earth radii. The Störmer equation shows that, for any direction specified by the zenith and azimuthal angles, the cutoff rigidity decreases with increasing geomagnetic latitude. This means that the high latitude regions are more accessible to transient particles.

The magnetic rigidity is also related to the particle's energy E in MeV by:

$$r = \frac{A}{z}\sqrt{E^2 + 2M_0 E} \quad (3.7)$$

where r is the magnetic rigidity in GV, A is the particle's mass in u*, z is the particle's charge, and M_0 is equal to 931 MeV. Because r is a function of the particle's charge, it can be shown that there is an east-west effect on the magnetic cutoff [15]. Positive particles arrive at the top of the atmosphere with greater abundance from the western part of the sky and negative particles from the eastern part of the sky.

While the Störmer theory is useful for theoretical understanding, the dipole approximation is not accurate in the real magnetic field of the Earth. In a real field, the precise values of cutoff rigidity are difficult to obtain because the equation of charged particle motion in a magnetic field does not have a closed form. Margaret Shea and Don Smart [16] calculated accurate cutoffs in the form of world map isocontours using the IGRF field models and by performing numerical integrations of particle trajectories. Because calculations must be carried out for each point, direction, and magnetic rigidity, this is not a practical method for analyzing particle accessibility to a spacecraft in orbit.

---

* u is unified atomic mass unit which is one twelfth of the mass of an unbound atom of carbon-12 (12C) at rest and in its ground state.

10

Smart and Shea [13] also derived useful approximations from Störmer's equation by normalizing to the Earth's actual magnetic field. The McIlwain's B-L coordinate system is used ($\cos^2\lambda = R/L$) with vertical cutoff rigidities (implying that ε and $\phi = 0°$) to give:

$$r = \frac{15.96}{L^{-2.001}} \quad (3.8)$$

where r is the cutoff rigidity and L is McIlwain's dipole shell parameter. With this relation, approximating particle accessibility to orbiting spacecraft becomes a simple matter of calculating L for altitude, latitude, and longitude positions and converting L to rigidity. By using the rigidity-energy equation given above, histograms are accumulated for the orbit and are used to attenuate the particle energy-fluence spectra of the transient particles. Figure 3.3.1 illustrates the particle energy-rigidity-L relationship. In the rigidity energy formula, z/A can be approximated with a value of 0.5 for ions Z > 1. Figure 3.3.2 shows magnetic rigidity contours on a world map at an altitude of 800 km as calculated by Shea and Smart.

Calculations of cutoff rigidity are further complicated by the effect of the solid Earth subtending particle paths. By stopping some particles, the Earth produces a "shadow" effect, blocking out some regions that would otherwise be accessible to particles. Adams *et al.* [17] derived a simple correction factor Ω which estimates the portion of the geometry factor occulted by the Earth:

$$\Omega = 2\pi \frac{1 - \sqrt{(R_E + h)^2 - R_E^2}}{R_E + h} \quad (3.9)$$

where R_E is the Earth's radius and h is the altitude.

3.4 Atmospheric Depth and Rigidity

The problem of neutron induced single event upsets in avionics [18,19] resulted in the need for a coordinate system to describe the neutron environment at aircraft altitudes. It is known that the neutron intensities vary with energy, altitude, and latitude. In reference 19, it is shown that simple models of neutron abundances can be constructed using altitude and latitude coordinates.

A more accurate coordinate system [20,21] replaces altitude with atmospheric depth (mass of air per unit area above the observation point) and latitude with vertical cutoff rigidity. Vertical cutoff rigidity was discussed in Section 4.2. The rigidity is strongest at the magnetic equator where a particle must have a rigidity of ~15 GV to penetrate and weakest at the poles where

---

*Neutrons are the products of interactions between galactic cosmic ray heavy ions and particles in the atmosphere. Therefore, the transport of the primary cosmic ray particles is important in determining neutron distributions.

particles need a rigidity of < 1 GV to penetrate. The second coordinate, atmospheric depth x in units of g/cm^2 is given as:

$$x = 1033 \exp \left\{ - \left[0.4534 - (1.17 \times 10^{-9}) \times \left| \frac{A - 1.05 \times 10^5}{1 \times 10^3} \right|^{3.58} \right] \left(\frac{A}{1 \times 10^3} \right) \right\} \quad (3.10)$$

where A is the altitude in feet. Atmospheric depth is used because atmospheric conditions have an effect on the measured particle intensity.

4 Interplanetary Particles

4.1 Galactic Cosmic Ray Heavy Ions

4.1.1 Discovery

In the early 1900s, scientists were puzzled by a mysterious source of "charge" on the leaves of electroscope instruments. During laboratory experiments, the electroscope leaves repelled each other without the presence of charge. Scientists assumed that this was the result of the ionization of air by the natural radiation present on Earth. Efforts were made to eliminate the radiation by using radiation pure materials, however, the problem persisted. In 1913 an Austrian scientist, Viktor Hess, devised an experiment to put an electroscope in a balloon to get it away from the Earth's radiation. As Hess and his experiment ascended in the balloon, he observed that the radiation source did not go away rather, as the altitude of the balloon increased, the radiation increased. Hess concluded that the source of this radiation was from outer space. In the summer of 1925, Robert Millikan confirmed with his lake experiments that the radiation source was from outer space. When he presented his lake experiment findings, he called the radiation "cosmic rays" [22]. Hess and C. D. Anderson received the Nobel Prize for their discovery of cosmic rays in 1936.

Intense interest in understanding cosmic rays continued into the 1950s. The launch of the Sputnik Earth orbiter by the Russians on October 4, 1957 sparked efforts in the United States to develop a space program. In 1955, James Van Allen and several other American scientists had proposed the launch of a scientific satellite as part of research programs to be conducted during the International Geophysical Year (IGY) of 1957-1958. Van Allen's interest in getting instruments into space was to study cosmic rays and their origin. The success of Sputnik led to the approval of Van Allen's proposal for the Explorer I spacecraft. Van Allen designed a cosmic ray detector to measure the low background cosmic rays, which was launched on board the Explorer I satellite on January 31, 1958 from Cape Canaveral, Florida.

In the late 1960s, the interest in cosmic rays of solar and galactic origin went beyond basic scientific research and became a safety issue when astronauts on Apollo missions reported visual

light flashes. Peter McNulty [23] proposed that Cerenkov radiation generated by individual cosmic ray ions traversing the vitreous of the eye were responsible for the flashes. He and his colleagues proceeded with a series of experiments that exposed human subjects, McNulty, Victor Pease, Victor Bond, and Lawrence Pinsky, to energetic heavy ions at accelerators. Understanding of the source and mechanism of the light flashes raised the concern for astronaut and safety, which in turn generated interest in measuring and modeling the galactic and heavy ion space environment. In fact, the IMP-8 spacecraft, which has provided the best long-term data set of heavy ions, was planned as a result of these concerns.

4.1.2 Newer Technologies Increased Concerns about Heavy Ions

Prior to 1975, heavy ion populations, whether of galactic or solar origin, were not considered a major concern for the reliability of spacecraft electronics. Regardless of the region of space that missions visited, the contribution of heavy ions to spacecraft charging, ionizing dose, or displacement damage effects were insignificant compared to other sources of radiation, such as, the trapped radiation belts or protons from solar events. Interest in understanding cosmic ray heavy ion particles changed in 1975 when Daniel Binder et al. [24] reported, "Anomalies in communication satellite operation have been caused by the unexpected triggering of digital circuits. Although the majority of these events have been attributed to charge buildup from high temperature plasmas, some of the events appear to be caused by another mechanism." In addition to an analysis of the circuit effects and the basic mechanism of these events, the authors presented cosmic ray spectra of Peter Meyer [25], and they calculated the intensities using abundances from various authors, including M. O. Burrell and J. J. Wright [26] who investigated dose rates of GCRs for astronaut exposure. Previous research on galactic cosmic rays by magnetospheric physicists interested in basic scientific research and by nuclear physicists concerned with astronaut dose became significant for the space community. McNulty [23] slightly modified the interaction models used to explain the light flashes observed by astronauts eyes to explain the upsets observed in microelectronic circuits. The Binder paper sparked intense interest in modeling heavy ion environments and interactions in materials.

4.1.3 Origin

Galactic cosmic ray heavy ions originate outside of the solar system. Their origin was a matter of debate for many years. The long-standing conjecture was that the shock front of a supernova remnant accelerates the GCRs arriving at the Earth [27]. In October 2007, using data from NASA's Chandra X-ray Observatory, Yasunobu Uchiyama et al. [28], reported the detection of extremely fast, year-scale variability in the X-ray flux from the supernova remnant RX J1713.7-3946. They observed remarkable variability in "real time" in the form of brightening and

decaying. Combining the Chandra data with results obtained from the Japanese Suzau X-ray satellite, Uchiyama *et al.* concluded that the supernova remnant is capable of accelerating GCRs to energies of the order of 1 PeV.

4.1.4   Composition and Energy Spectra

Our knowledge of the abundances of galactic cosmic rays comes from spacecraft and balloon experiments that have been conducted over a fifty-year period. Galactic radiation consists of ions of all elements of the periodic table and is composed of about 83% protons, 13% alphas (^{4}He ions), 3% electrons, and about 1% heavier nuclei. Figure 4.1.4.1 from Richard Medwaldt [29] shows the abundances of the heavy ions at an energy of 2 GeV/nucleon as a function of particle nuclear charge z. The values are normalized to silicon = 10^6. Note that the relative flux intensities vary by several orders of magnitude. The relative abundances are roughly proportional to the distribution in solar system material. Significant differences are discussed in Medwaldt [29] who also gives a table of relative abundances. Because GCRs must pass through about 7 g/cm^2 of interstellar gas, those of even the heaviest ions are probably fully ionized [30].

A second source of galactic particles is the so called "anomalous component". It is composed of helium and heavier ions with energies greater than 50 MeV/nucleon. It is believed that the anomalous component originates in the neutral interstellar gas that diffuses into the heliosphere, becomes singly ionized by solar radiation or charge exchange, and is then connected by the solar wind to the outer heliosphere. The ions are then accelerated and propagate to Earth. The anomalous component is seen only during solar minimum and the details vary from solar minimum to solar minimum. There is growing evidence that the anomalous component is singly ionized, therefore, the ions have greater ability to penetrate the magnetosphere. The anomalous component of the galactic cosmic rays is thought to be the source of heavy ions trapped in the Earth's magnetic field.

The galactic cosmic ray population also contains electrons. However, the electrons are not in sufficient number to make the population electrically neutral. The GCR electron density is orders of magnitude lower than the density of the solar wind; therefore, it does not have to be taken into account when evaluating radiation damage levels.

The interplanetary energy spectra for H, He, and Fe are given in Figure 4.1.4.2 [31]. The H values are multiplied by five for better resolution on the graph. The measurements were taken for various times throughout the solar cycle as shown by the variation of the spectra below energies of 1 to 3 GeV. As discussed in Section 3.3. Figure 4.1.4.3 gives GCR energy spectra for a low earth orbit (LEO) at 29° inclination and 600 km perigee and apogee, a middle earth orbit (MEO) at 51° and 10,000 km perigee and apogee, a geostationary orbit (GEO) at 0° inclination and

14

36,000 km perigee and apogee, a geostationary transfer orbit (GTO) at 18° inclination and 360 km perigee and 36,000 km apogee, and the orbit for the Earth Observatory Satellite (EOS) at 98° inclination and 705 km perigee and apogee.

Scientists believe that GCRs propagate through all space that is unoccupied by dense matter. They are essentially isotropic outside of regions of space that are dominated by particles and fields of the Sun. Measurements from Pioneer and Voyager show that the composition of cosmic rays is weakly dependent on the distance from the Sun. The radial gradient from 0.3 to 40 AU is < 10% per AU. For the anomalous component, the gradient increases to 15% per AU. During solar actives periods of time, there is 0% gradient out to 30 AU. Latitude gradients have also been studied and found to be 0.5% per degree and 3-6% per degree for the anomalous component [30].

4.2 Solar Particles

4.2.1 Discovery

In response to a 1932 recommendation by Robert A. Millikan and Arthur H. Compton, the Carnegie Institution of Washington sponsored the development of a network of detectors for the continuous recording of cosmic-ray intensity. The data from these meters were central to Scott Forbush's research for many years. In 1946, Forbush was performing a retrospective study of ionization chamber data from Cheltenham, Godhavn (Greenland), Christchurch, and Huancayo. In the records of the three high- and mid-latitude stations, he found large impulsive increases in cosmic-ray intensity on February 28 and March 7, 1942, and on July 25, 1946, each following an exceptionally large solar "flare". No increase was observed at the equatorial station, Huancayo. The brief (hours) increases in particle intensity were precursors to large Forbush decreases* at all four stations. He concluded that the increases originated from solar impulsive emission of energetic particles having energies up to at least 3 GeV, but less than the geomagnetic cutoff at Huancayo, about 15 GeV [32,33]. Study of the sporadic solar emission of energetic protons and heavier ions and of electrons subsequently became a major field of research in solar and interplanetary physics as the energy and intensity thresholds for their detection have been progressively lowered, especially by instruments on spacecraft. According to James Van Allen, "Scott Forbush laid the observational foundations for many of the central features of the now huge field of solar-interplanetary-terrestrial physics." [33]

---

* A Forbush decrease is a rapid decrease in the observed galactic cosmic ray intensity following a coronal mass ejection (CME). It occurs due to the magnetic field of the plasma solar wind sweeping some of the galactic cosmic rays away from Earth.

4.2.2 Effects of Solar Particles on Spacecraft

The particles from solar events cause radiation damage and single event effects on spacecraft. In fact, for spacecraft in orbits that visit regions outside of the Earth's magnetosphere where they are exposed to these particles, they are often the driver for setting single event effects requirements. Experimenters have measured single event upsets (SEUs) on several satellites. Reno Harboe-Sørenesen et al. [34] measured SEU rates in regions of space where $L > 2$ and found that, during the October 1989 solar particle event, the rates increased by factors of 3 to 30 depending on the SRAM or DRAM memory type. Len Adams et al. [35] measured a similar response to the October 1989 event in memories on board the Meteosat-3, which was in a geostationary orbit. Figure 4.2.2.1 shows daily counts of SEUs on the Seastar solid state recorder. Superimposed on the daily background rate of upsets caused by protons in the SAA are sudden increases for brief periods of time (hours) caused by particles from solar storms. In the last solar cycle, Clive Dyer et al. reported on solar proton and heavy ion induced SEUs and a single event transient (SET) observed on spacecraft during the October and November 2003 solar storms [36].

Protons from solar particle events also contribute to total dose and solar cell damage, especially for interplanetary missions and those at geostationary positions and in geostationary transfer orbits. Adams et al. [35] measured doses with RADFETs on the Meteosat 3 and found that doses jumped by a factor of 20 with the onset of the October 1989 event. Figure 4.2.2.2 shows average solar array power plotted as a function of time for four Cluster spacecraft. Note the sudden decrease in solar array power caused by the increase in solar particles during the October 2003 solar storm.

4.2.3 Origin

Solar energetic particles are accelerated at multiple sites on the Sun, including exploding flare loops, magnetic reconnection sites, and shocks that move from the lower corona to the inner heliosphere. The largest events, which can cause dangerous radiation levels at Earth, may include more than one acceleration site. Solar flare explosions can accelerate particles immediately and may also set off instabilities in magnetic structures in the corona that can launch coronal mass ejections (CMEs). These often drive shocks that can begin to accelerate additional energetic particles minutes after the CME is launched and continue to do so for days in the case of the largest events.[37] Solar energetic particle events (SEPs) are infrequent when the Sun is in its inactive phase.

Despite some troubling uncertainties, scientists long sought to identify large solar flares as the primary cause of large, non-recurrent geomagnetic storms, transient shock wave disturbances in the solar wind, and major energetic particle events. This thinking about solar events is what

16

John Gosling labeled the "solar flare myth" [38]. Gosling and others showed that the major disturbance events observed in interplanetary space are strongly correlated to CMEs that have no fundamental association with flares. Although particles are often accelerated to high energies during flares, they are not directly associated with the major events observed near the Earth.

To support his theory, Gosling cited the work of Don Reames [39] who categorized solar energetic particle events into two types corresponding to two types of solar x-ray flares. In "gradual" events, the decay of the x-ray intensity takes place over many hours. In "impulsive" events, a sharp peak in x-ray emission occurs. In Figure 4.2.3.1, the time profiles of protons for the two types of events are plotted showing why they were labeled gradual and impulsive.

Gradual events (also known as long duration events) are strongly associated with CMEs. Reames showed that particles from these events have the same elemental abundances and ionization states as the Sun's corona and the solar wind plasma. Approximately 10 gradual events per year are observed at 1 AU during solar maximum [40]. CMEs tend to be the events with the largest proton fluences. The very largest SEP events are associated with fast CMEs. Multiple CMEs occur every day at solar maximum, so it is a mystery why only about one CME per month creates a large SEP event.

Impulsive events are characterized by marked enhancements of heavy ions. The Fe/O ratio is approximately 1.0 in comparison to 0.1 or less in gradual events. Also, the ^{3}He/^{4}He ratio is 2 to 4 orders of magnitude larger than in the solar atmosphere or in the solar wind. Impulsive events originate deeper within the Sun, and the particles may be directly accelerated by solar flares. Low energy electrons dominate the impulsive events, and these events have smaller proton fluxes than the gradual events. Reames has shown that the elemental abundances of particles from gradual events are characteristic of interactions in the flare plasma. Approximately 1000 impulsive events per year are observed at 1 AU during solar active periods of time [39]. Impulsive events represent the majority of the small solar particle events observed at Earth.

The solar longitude of the flare or CME largely determines the rise time of the particle fluence and the severity of the event. The solar longitude most effective for producing fluxes in the GeV/nucleon range is close to 60° west and the solar longitude most effective in producing large solar enhancements with energies greater than 10 MeV/nucleon is 30° west.

Solar physicists are seeking to understand the roles and importance of the different processes that produce and accelerate solar particles and have proposed a "Solar Sentinel" mission to make multipoint spacecraft measurements between the Sun and the Earth [37]. By making comprehensive measurements close to the Sun where their signatures are more readily identifiable, we can separate and understand their roles. Figure 4.2.3.2 shows electron and alpha

17

particle time profiles recorded by Helios-1 at 0.3 AU and by IMP-8 measured at 1.0 AU during a series of impulsive particle events on 28 May 1980. Whereas Helios-1 observed multiple injections, no such structures can be resolved in the intensity–time profile at 1 AU. If both spacecraft were observing the same events (and this is not certain), then this plot illustrates the effects of both radial and longitudinal transport inside 1 AU and the need for observations as close to the Sun as possible [41].

4.2.4 Composition and Energy Spectra

As with galactic cosmic rays particles, our knowledge of the abundances of SEP events comes from spacecraft and balloon experiments. However, unlike the galactic cosmic ray particles which are always present, SEP events occur sporadically and are rare when the Sun is in its inactive phase. Therefore, the data sets for SEP event measurements are not as dense as those for the GCRs.

Solar energetic particle events increase the levels of electrons, protons, and heavy ions in interplanetary space and consist of all elements of the periodic table. Unlike the GCRs which have their electrons stripped when passing through interstellar matter, the solar heavy ions are singly ionized which increases their ability to penetrate into the magnetosphere. The SEP events last from several hours to a few days. Figures 4.2.4.1 and 4.2.4.2 show electron (E > 2 MeV) and alpha ion (E = 4-10, 10-21, 21-60, 60-150, 150-250, and 300-500 MeV) measurements (uncorrected) at geostationary altitude from the GOES 6 environment monitor during the October 1989 solar storm. Note that levels of particles increase orders of magnitude over the background level and that before the ion fluxes from the first SEP event decay to background levels, the ions from the next event arrive.

The duration, composition, particles levels, and energy spectra vary widely from event to event so a typical SEP event cannot be defined. This is shown in Figure 4.2.4.3 which plots solar proton energy spectra for several large events from solar cycle 22. As with the GCRs solar particles are also attenuated by the Earth's magnetosphere as shown in Figure 4.2.4.4 which gives the energy spectra for solar protons for a low earth orbit (LEO) at 29° inclination and 600 km perigee and apogee, a middle earth orbit (MEO) at 51° and 10,000 km perigee and apogee, a geostationary orbit (GEO) at 0° inclination and 36,000 km perigee and apogee, a geostationary transfer orbit (GTO) at 18° inclination and 360 km perigee and 36,000 km apogee, and the orbit for the Earth Observatory Satellite (EOS) at 98° inclination and 705 km perigee and apogee.

Figure 4.2.4.5 from Michael Xapsos et al. [42] (points on the plot from Allan Tylka et al. [43]) shows the energy-flux spectra derived from the GOES Space Environment Monitor, the

18

IMP-8 Goddard Medium Energy instrument, and the ACE Solar Isotope Spectrometer instrument. From this plot we see that the energies of the heavy ions from SEP events can also reach a few hundred MeV.

Solar particle intensity also varies with distance from the Sun. As particles move away from the Sun, the particles diffuse into the larger volume of space. Spacecraft near the Earth have provided us with a large data set of particles measurements so particle intensities are scaled as a function of distance from the Earth. (The Earth is at 1 AU or the distance between the Sun and the Earth). We know from Pioneer and Voyager measurements that the particle intensity varies by $1/r^2$ where r is in units of AU as move away from the Earth. Because there are so few measurements as we move closer to the Sun (less than 1 AU), we are not certain about the variation of particle intensity. Estimates range from $1/r^2$ to $1/r^3$.

5   Trapped Particles

5.1   Discovery

Kristian Birkeland theorized the existence of radiation trapping in planetary magnetospheres in 1895 when he performed vacuum chamber experiments to study aurora. With Henri Poincaré, he showed that charged particles spiral around field lines and are repelled by strong fields. Later Stöermer continued the work of Birkeland on aurora and made calculations that led to the theory that there was a belt-like area around the earth in which particles were reflected back and forth between the poles. However, it was felt that the magnetic field was not strong enough to hold the particles. In 1957 Singer proposed that ring current could be carried by lower energy particles injected by into trapped orbits by magnetic storms. A complete history of radiation belt science is given in Space Storms and Space Weather Hazards [44].

Recall from Section 4.1.1, the United States space program began with the 1958 launch of the Explorer I spacecraft with Van Allen's instrument to study cosmic rays and their origin. In analyzing the data from his instrument, Van Allen was puzzled by "zero" readings. At first he thought that the instrument had malfunctioned but later he realized that the instrument was being "flooded" with radiation measurements. Van Allen determined that his instrument was measuring intense radiation surrounding the Earth, and he announced his discovery on May 1, 1958 [44,45]. Most of the scientific instruments flown in space in the late 1950s and early 1960s were designed to detect energetic protons and electrons. With the results, scientists gained a general understanding of the near-Earth radiation environment but found differences up to a factor of 10 when making quantitative comparisons between measurements in the same locations.

19

It was also during the early 1960s that spacecraft electronics were found to be unreliable. Problems from differential charging from the solar wind and from noisy data transmission to the Earth from soft fails were noted. These problems were largely dealt with by building redundancy into systems. As the first scientific satellites were being launched in the late 1950s and early 1960s, the Union of Soviet Socialist Republics and the United States also detonated nuclear devices at altitudes above 200 kilometers. The most dramatic of these tests was the US Starfish detonation on July 9, 1962. Ten known satellites were lost because of radiation damage, some immediately after the explosion [46]. The Starfish explosion injected enough fission spectrum electrons with energies up to 7 MeV to increase the fluxes in the inner trapped radiation belt by at least a factor of 100. Effects were observed out to 5 Earth radii. The Starfish electrons that became trapped (modeled by Teague and Stassinopoulos [47]) dominated the inner zone environment (~ 2.8 Earth radii at the equator) for five years and were detectable for up to eight years in some regions.

5.2   Effects of Trapped Particles on Spacecraft

Problems of radiation effects in spacecraft systems operating in the Earth's trapped radiation belts have been identified from the earliest days of space exploration. Even in regions where the radiation levels are relatively stable and benign, sensitive technologies are susceptible to the impacts of the trapped protons and electrons. Figure 5.2.1 shows single event upsets on the NASA Seastar Mission's Solid State Recorder that clearly define the SAA. (Note that no data were lost in this mission due to mitigation that was implemented in the system design.)

High energy protons in the inner radiation belt are the main contributors to ionizing dose deposition in shielded components. They also dominate single event upset (SEU) rates at low altitudes and latitudes, where cosmic rays and solar energetic particles are effectively shielded by the geomagnetic field. Lower energy protons (up to 10 MeV) contribute to displacement damage on detectors and solar cells.

Low energy electrons contribute to spacecraft surface charging. High energy electrons injected and accelerated through the magnetotail can cause dielectric charge buildup deep inside spacecraft in geostationary orbits which can result in destructive arcing. Inner and outer belt electrons also contribute to ionizing doses through direct energy deposition and bremsstrahlung effects.

5.3   Origins and Trapping Mechanism

The energetic charged particles trapped in the trapped radiation belts are protons, electrons, and heavy ions. The electrons move at speeds near the speed of light, therefore, they must be

20

analyzed by using relativistic theory. Protons and other heavy ions are much slower. The Earth's atmosphere is the lower boundary of the radiation belts due to a particle loss mechanism that is discussed later in this section. The upper boundary is determined by the strength of the geomagnetic field. As the distance from the Earth increases, the magnetic field decreases to the point where stable trapping can no longer occur.

While a number of possible sources for the trapped particles have been identified, we do not have a complete understanding of precisely where they come from or how they are accelerated to high energies. The solar wind is a possible source. Some solar wind particles may cross magnetic field lines and leak into the magnetosphere, and others may collect in the magnetotail in the neutral plasma sheet and be ejected Earthward during times of increased geomagnetic activity. Also, ions and electrons from the ionosphere may diffuse out of the polar ionosphere and escape into the magnetotail regions. From the magnetotail, these particles can become energized and be ejected into the trapping regions. The primary source of inner zone particles is referred to as cosmic ray albedo neutron decay (CRAND). The primary cosmic ray particles from interplanetary space collide with atmospheric atoms, producing neutrons that decay into energetic protons and electrons. Also, interplanetary particles that have been accelerated by interplanetary shock waves or in the magnetosphere of other planets, and low energy components of the galactic cosmic rays (see Section 4.1.3) may find their way into the trapped radiation regions. *In situ* acceleration occurs during magnetic storms when low energy particles that are already trapped are transported to lower L-shells, thereby, increasing their energy [48].

The plasma sheet (see Figure 2.3.1) in the Earth's magnetotail is a mixture of particles from several of the sources mentioned above. By the process described in reference 2, particles in the plasma sheet convect toward the Earth and become accelerated and trapped in the radiation belts during magnetospheric substorms.

Whatever the source, the protons and electrons become "trapped" because the Earth's magnetic field constrains their motion perpendicular to the magnetic field vector. The electromagnetic Lorentz force is directly responsible for restraining a trapped charged particle and keeping it well within a defined region around the Earth. It is given by:

$$\frac{dp}{dt} = qv \times B \quad (5.1)$$

where p is the momentum, q is the charge, v is the velocity, and B is the magnetic field. The two components of the instantaneous velocity vector are the component parallel to the magnetic field and the component perpendicular to the field. As a result of the forces acting on the particles, they

21

spiral around magnetic field lines, oscillating back and forth between the northern and southern hemispheres. Because of the non-uniformity of the geomagnetic field, the particles do not mirror back to exactly the same point from which they started. Therefore, superimposed on the spiral and bounce motions is the slow westward drift of protons and the eastward drift of electrons. (see Figure 3.2.1) The opposite direction of the drift is a result of the opposite charges of the particles producing opposite spiral directions. The frequency of the spiral motion (gyration) at 1000 km altitude is about 0.5 Mhz for very low energy electrons and 300 Mhz for low energy protons. As energy increases, the period decreases because of the greater relativistic mass. The bounce period at 1000 km is about 1 second for 1 MeV protons and about 0.1 second for 1 MeV electrons. It takes about 1/2 hour for 1 MeV protons to complete an azimuthal drift cycle at 1000 km and about 1 hour for electrons. Because the frequencies are of different orders of magnitude, the three motions are "uncoupled". These three motions confine the region occupied by the particles to drift shells, designated by the L parameter, which was described in Section 3.2.

The best way to characterize and model the trapped radiation environment is to combine theoretical approaches and experimental measurements. To simplify theoretical descriptions, a dipolar magnetic field is assumed. Extensive work was done in the first half of the 20th century to find a general analytic solution to the equation of motion for a charged particle in a dipolar field. It was never found, and particle traces had to be done numerically [49]. In 1963 Hannes Alfvén and Carl-Gunne Fälthammer [50] introduced physical simplifications known as adiabatic theory. The motion of trapped particles in the radiation belts has been described successfully by using three adiabatic invariants. They are called adiabatic because, under certain conditions, the invariants remain unchanged with the particle motions. If the reader wishes to investigate this topic in more detail, several researchers have provided detailed mathematical derivations of approximations of the motion of trapped particles [50,51,52]. Highly readable descriptions of trapped particle morphology are provided by Al Vampola [53] and Daniel Boscher et al. [54].

Over long periods of time, the trapped radiation belts are stable because of four simultaneous processes; the injection of charged particles into the trapping region of the magnetosphere, particle acceleration, particle diffusion, and particle loss. The processes occur simultaneously, e.g., some particle loss mechanisms are the result of diffusion, particle acceleration is coupled to diffusion. This makes mathematical treatment of diffusion extremely complicated to solve numerically.

A short description of particle diffusion and loss mechanisms will be given here. Detailed discussions of diffusion mechanisms are provided by Juan Roederer in reference 51 and a detailed description of diffusion processes is given by Michael Schultz and Louis Lanzerotti in reference

52. Two diffusion processes important to trapping theory are radial diffusion and pitch angle diffusion. Radial diffusion transports particles across dipolar magnetic field lines and may explain how some solar wind particles reach the magnetosphere. Pitch angle diffusion alters the particle's pitch angle, hence, its mirror point location. In both cases, the Earth's atmosphere causes removal of particles through collisions with atmospheric particles. Radial diffusion transports them to very low L-shells and pitch angle diffusion lowers the mirror points into the atmosphere. Besides particle loss due to collisions with the atmosphere, collisions of trapped particles with atomic hydrogen in the exosphere and particles in the plasmasphere are important loss mechanisms.

5.4   Composition and Energy Spectra

Figure 5.4.1 is an artist's drawing, which shows the belt-like structure of Earth's trapped particle regions. The trapped particle populations are divided in a compact region called the "inner" zone and a large "outer" zone region that wraps around the inner zone. This figure does not show the SAA (a bulge in the underside of the inner belt caused by the tilt of the Earth's magnetic pole from the geographic pole and the displacement of the magnetic field from the center). The SAA is a dominate feature in the trapped radiation belts in the altitude regions of ~300 to ~1200 km. Figure 5.4.2 shows the SAA on a map of proton fluxes plotted as a function of invariant latitude. Despite the SAA's reputation for plaguing spacecraft, the flux levels there are actually much lower than those at higher altitudes.

Protons are the most important component of the inner zone. The energies range from tens of keV to hundreds of MeV with intensities up to 10^5 protons/(cm^2-s) for energies greater than 30 MeV. The location of the peak flux intensities varies with particle energy. In the equatorial plane, the high energy protons (> 30 MeV) extend only to about 3.5 Earth radii. Figure 5.4.3 shows the particles fluxes for several proton energies as a function of L along the geomagnetic equator ($B/B_0=1$) as calculated with the AP8 model for trapped protons [55]. Note that, due to the trapping dynamics, the peak fluxes shift to higher L values as the energy decreases. Therefore, even though there is a sharp cutoff of high energy protons at L > 2.4, the "slot" region is filled with lower energy protons and is not devoid of particles as is often portrayed in illustrations. The E > 30 MeV proton fluxes peak at approximately 2,500 km altitude at the equator. Figure 5.4.4, a plot of proton flux contours at 1,000 km altitude, shows the shape of the inner zone proton belt on a world map.

Figure 5.4.5 plots proton energy fluence spectra obtained when calculating fluence levels with the AP-8-MAX model for a low earth orbit (LEO) at 29° inclination and 600 km perigee and apogee, a middle earth orbit (MEO) at 51° and 10,000 km perigee and apogee, a geostationary

orbit (GEO) at 0° inclination and 36,000 km perigee and apogee, a geostationary transfer orbit (GTO) at 18° inclination and 360 km perigee and 36,000 km apogee, and the orbit for the Earth Observatory Satellite (EOS) at 98° inclination and 705 km perigee and apogee. The figure shows that the variations in fluence level due to spacecraft orbit reach orders of magnitude. In general, the greatest inclination dependencies occur in the range of $0° < i < 30°$. For inclinations over 30°, the fluxes rise more gradually until about 60°. Over 60°, increasing inclination has little effect on the proton flux levels. The largest altitude variations occur between 200 to 600 km where large increases in flux levels are seen as altitude rises. For altitudes over 600 km, the flux increase with increasing altitude is more gradual. As with the L parameter, the altitude where the peak proton fluxes occur varies with particle energy. This implies that the location of peak of a device response to the environment will depend on the type of effect and on the sensitivity of the device.

The electrons are trapped into two regions, the inner and outer zones. Under normal conditions of the magnetosphere, the electron distribution can be separated into two zones, the inner ($1.0 < L < 2.8$) and outer ($2.8 < L < 12.0$). The energies modeled by the AE8 model [56] for trapped electrons in the inner zone are 0.04 to approximately 4.5 MeV. The modeled outer zone energy spectra extend to energies up to 7 MeV. The intensities reach about 10^7 electrons/(cm^2-s) for energies greater than 0.5 MeV. Figure 5.4.6 gives the electron fluxes for several energies as a function of L along the geomagnetic equator. Notice the double peaks, which distinguish the inner and outer zones. As with the protons, the location of the peak flux varies with energy. Also, although the slot region has reduced numbers of electrons, it is not devoid of particles. The $E > 2$ MeV peak electron fluxes at the equator are at approximately 2,500 km altitude in the inner zone and at 20,000 km altitude in the outer zone. Figure 5.4.7, a plot of electron flux contours at 1,000 km altitude, shows the shape of the inner zone electron belt and the high latitude outer zone electrons "horns" that wrap around the inner belt on a world map.

Figure 5.4.8 plots electron energy fluence spectra for the same LEO, MEO, GTO, GEO, and the EOS orbits. Notice that, for higher altitudes, the spectra become more energetic and increase in intensity due to increasing exposure to the more intense outer zone electrons. The altitude and inclination dependencies are similar to those of the protons but, as seen in the GEO spectra, the electrons extend out to higher altitudes. As with the L parameter, the altitude where the peak fluxes occur varies with energy.

Heavy ions are also trapped in planetary magnetic fields. For most shielded spacecraft systems, the abundances of these ions at energies high enough to penetrate spacecraft materials are too low to be a dominant factor in the rates of in single event effects in electronics systems.

24

5.5 Other Planets

The minimum requirement for the existence of a planetary radiation belt is that the planet's magnetic dipole moment must be sufficiently great to arrest the flow of the solar wind before the particles reach the top of the atmosphere where the particles will lose their energy due to collisions. Venus and Mars do not have magnetospheres and, therefore, cannot support particle trapping. The magnetic fields of some of the other planets are similar to the Earth's, however, they vary in strength. Mercury has a weak magnetic field so it is expected that it has a trapped particle population proportionally lower than that of the Earth. Saturn, Uranus, and Neptune have magnetic fields with similar strength to that of the Earth but measurements indicate that the intensities of the trapped radiation environments of Saturn, and Uranus are much lower than the Earth's and do not pose serious problems to the design of spacecraft systems. On the other hand, Jupiter's enormous magnetic dipole (428,000 compared to 30,760 nanoTesla for Earth) can support an intense particle environment. Its magnetosphere is the largest object in the solar system. Measurements have shown that Jupiter's radiation environment is considerably more intense than the Earth's and is more extensive, therefore, mission planning for spacecraft that will spend even short times in the trapping regions of Jupiter must include careful definitions of the radiation environment. The Phobos probe showed that Mars has a radiation environment; however, it is due to the thin atmosphere of Mars, which allows interplanetary GCRs and solar particles to penetrate to the surface. Interaction of these particles with the atmosphere produces neutrons, which penetrate to the planetary surface and then reflect back.

6 Atmospheric Radiation

6.1 Discovery

As cosmic ray and solar particles enter the top of the Earth's atmosphere, they are attenuated by interaction with nitrogen and oxygen atoms. The result is a "shower" of secondary particles and interactions created through the attenuation process (see Figure 2.4.1). Products of the cosmic ray showers are protons, electrons, neutrons, heavy ions, muons, and pions. This section will focus on the neutron component of atmospheric radiation due to the importance of upsets in aircraft avionics systems.

Serge Korff is credited with discovering cosmic ray neutrons. The focus of his scientific career was observing and mapping the rain of neutrons and, he made balloon observations in Guam, the Galapagos Islands, Greenland, the Caribbean and several points within the United States. To obtain readings from as close as possible to the top of the atmosphere, observations were made from an elevation of 17,100 feet in Chacaltaya, Bolivia; from the top of Mount

Wrangell in Alaska, from rockets and from high-flying aircraft. Among the flights was one circling the earth over both poles. In 1951 Korff published his discovery of neutrons produced by the cosmic radiation, including his findings on the effects of altitude and latitude dependence [57].

6.2 Neutron Effects on Aircraft Avionics

Two papers published in 1984 pointed out the hazard of single event upsets at avionics altitudes. C. H. Tsao *et al.* [58] showed that, below altitudes of about 60,000 feet, secondary neutrons from cosmic ray heavy ion fragmentation are the most important contributor to SEUs. Rein Silberberg *et al.* [59] give a method for calculating the neutron SEU rate. They also predict that SEU rates increase with enhanced solar particle backgrounds. Since that time, several flight experiments [19] have demonstrated that energetic particles can cause single events effects in electronics at avionics altitudes. In a study completed in 1992 [18], SEU rates measured in flight were shown to correspond with atmospheric neutron flux levels, and rates calculated using laboratory SEU data agreed with the measurements.

6.3 Energy Spectra

Our knowledge of neutron levels comes from balloon, aircraft, and ground based measurements. Since the discovery of SEUs at aircraft altitudes, researchers have made significant efforts to monitor the environment. Dyer *et al.* flew a version of their Cosmic Ray Environment and Activation Monitor (CREAM) on regular flights on board Concorde G-BOAB between November 1988 and December 1992. They first reported on the results of measurements aboard the Concorde aircraft [60]. Results from 512 flights were analyzed of which 412 followed high latitude transatlantic routes between London and either New York or Washington DC [61]. Thus some 1,000 hours of observations have been made at altitudes in excess of 50,000 feet and at low cut-off rigidity (< 2 GV), and these span a significant portion of solar cycle 22. In an investigation of single event upsets in avionics, Taber and Normand [62] flew a large quantity of CMOS SRAM devices at conventional altitudes on a Boeing E-3/AWACS aircraft and at high altitudes (65,000 feet) on a NASA ER-2 aircraft. Upset rates in the IMS1601 64Kx1 SRAMs varied between 1.2×10^{-7} per bit-day at 30,000 feet and 40° latitude to 5.4×10^{-7} at high altitudes and latitudes. Reasonable agreement was obtained with predictions based on neutron fluxes.

James Ziegler and colleagues [63] began an effort to define the cosmic ray terrestrial environment based on the work of many researchers who began studying cosmic radiation after Hess' balloon experiments. The focus of the work was on defining neutron energy spectra as a function of altitude as shown in Figure 6.3.1. In the figure, the altitude dependence is expressed

26

as atmospheric depth where 0 g/cm^2 represents the top of the atmosphere. Figure 6.3.2 shows the measured neutron flux normalized to the peak versus altitude for two energy ranges, E = 1 - 10 MeV and 10 - 100 MeV. It shows that the neutron flux peaks at an altitude of about 60,000 feet, which is the same altitude of the peak of observed SEU rates.

Balloon and aircraft studies show that the energies of the neutron flux range from keV to hundreds of MeV. For SEU calculations in aircraft systems, it is usually only the energies greater than 10 MeV that is significant. However, it has recently been demonstrated by Dyer and Fan Lei [64] that aircraft structures, passengers and fuel can produce significant thermal neutron fluxes, leading to potentially high rates of SEU in components containing the nuclide boron-10 in borophosphosilicate glass passivation layers.

7   Dynamics of the Radiation Environment

To this point, discussions have focused on the discovery, origins, and general descriptions of the radiation environments. Variations in the space environments depend on location in space and on the year in the solar cycle, both somewhat predictable. However, large variations that depend on events on the Sun are not predictable with reasonable certainty. Our knowledge of large variations is statistically based and is useful in the design phase of space systems to determine upper limits on the severity of the space environments. However, knowledge based on statistics has limited application for forecasting the real time space environment for operational systems.

The challenge in modeling the radiation environments comes from the complex variations in the environment which are driven by short- and long-term variations in the magnetic field and solar activity. Also, the complexities of the variations are not entirely understood compounding the modeling challenge. The next section will present environment variations caused by changes in the Earth's internal magnetic field, the variations in the solar cycle, and disturbances in the interplanetary magnetic field due to storms on the sun. Section 8 will review the development of models of the radiation environment and attempts to represent environment variations in the models.

7.1   Geomagnetic Field Drift

The spacecraft data used to construct the AP-8 [55] and AE-8 [56] models of the trapped protons and electrons populations were normalized to 1960 or 1970 dates with two field models. However, the shift in the internal magnetic field (see Section 3.1) causes a predominantly westward drift of the SAA of approximately 0.3 degrees/year [65,66] which is not represented in the AP-8 and AE-8 models. Errors from the SAA shift are averaged out when using these models

27

to calculate total mission orbit integrated fluences. However, for applications that require knowledge of the location of SAA fluxes, such as, instrument operation or flight data analyses, it is important to know the correct location and flux levels in the SAA. To minimize the error, Daly et al. [67] demonstrated the need to calculate fluxes from the models with the field values used to normalize the data, and if the absolute position of the flux is important for one's application, it is necessary to perform a latitude and longitude transformation reflecting the shift of the magnetic field to place the fluxes in the correct latitude and longitude positions.

Gregory Ginet et al. [68] used measurements from the Compact Environment Anomaly Sensor (CEASE) flown onboard the Tri-Service Experiment-5 (TSX-5) satellite (410 km x 1,710 km, 69 degree inclination orbit) to develop a new set of flux intensity maps for energetic protons in the South Atlantic Anomaly (SAA) region for the epoch 2000-2006. Maps were constructed for > 23 MeV, > 38 MeV, > 66 MeV, and > 94 MeV protons with boundary contours for 1/2 maximum, 1/10 maximum, and 3 times the derived standard deviation of the background. Estimates are given of the integral energy spectra as a function of altitude from 400 km to 1650 km, an interval spanning the range where the controlling factor in the dynamics changes from the neutral density to the global magnetic field. The position of the maximum flux point is compared to that determined from earlier measurements in the 1994-1996 epoch and found to be consistent with the westward drift. Figure 7.1.1 shows the map of corrected particle locations for > 23, 38, 66 and 94 MeV protons for an altitude range of 800 to 850 km [68].

7.2 Solar Activity

The Sun is composed of gas, so its solar magnetic field is convoluted and highly variable. The Sun has a 22-year cycle of activity that is caused by the rapidly varying dipole moment reversing polarity every 11 years. The Sun's activity also has short-term variations in the form of intense, short lived storms. Both phenomena are responsible for observable changes in interplanetary and near-Earth radiation levels. The best known variation in solar activity is the sunspot cycle. Records of naked-eye sunspot observations in China go back to at least 28 BCE. The scientific study of sunspots in the West began after astronomers began to use the telescope in 1609. Galileo and Thomas Harriot were probably the first who recorded telescope observations around the end of 1610. [69] Starting in 1825, S. Heinrich Schwabe observed the Sun nearly every day for 42 years. In 1843 Schwabe found that his 17 years of nearly continuous sunspot observations revealed a 10-year periodicity in the number of sunspots visible on the solar disk [70]. The 11-year cycle of sunspots corresponds to similar 11-year cycles of other features in the

sun's active regions, including the number of faculae[*], the rate of incidence of solar flares and CMEs, and the intensity of coronal x-ray and radio-frequency emissions. Figure 7.2.1 gives a plot of the historical record of sunspot averages as a function of time.

The length of the solar cycle can be highly variable. From 1645 to 1715, the sunspot activity seemed to disappear. Because temperatures on Earth dropped during that time, those 70 years are known as the little ice age. From 1100-1387, there was an increase in the number of sunspots. Studies of recent solar cycles [71,72], cycles 19 through 22, determined that the length of the solar cycle over the past 40 years ranged from 9 to 13 years, with 11.5 being the average. For modeling purposes and for defining the environment for spacecraft missions, the solar cycle is usually divided into a 7-year maximum phase of high levels of activity and a relatively "quiet" 4-year minimum phase.

The study of solar-terrestrial physics began with two observations. Edward Sabine [73], reported the observation that geomagnetic activity appeared to track the 11-year sunspot cycle. In 1859, Richard Carrington [74] observed a brightening on the surface of the sun now known as a solar flare. He noted that a large geomagnetic storm began within a day of the flare. From 28 August until 2 September, 1859, numerous sunspots and solar flares were observed and it is believed that a massive CME arrived at the Earth within eighteen hours. On 1 and 2September, the largest recorded geomagnetic storm occurred. Telegraph wires in both the United States and Europe shorted out, some even causing fires. Auroras were seen as far south as Hawaii, Mexico, Cuba, and Italy, phenomena which are usually only seen near the poles. Recently, the "Carrington Event" was analyzed and compared to other large events by a group of scientists, resulting in a publication of their findings [75].

Major perturbations in the geomagnetic field can occur with changes in the solar wind density (e.g., solar flares), the solar wind velocity (e.g., CMEs), and the orientation of the embedded solar magnetic field. The CMEs and solar flares cause disturbances of the solar wind, and it is the interaction between these disturbances and the Earth's magnetosphere that causes the perturbations called magnetic storms and substorms. During storms, energy is extracted from the solar wind, is stored, and then dissipated. This process results in a redistribution of particles in the Earth's magnetosphere [53].

The substorm process begins in the magnetotail. The neutral sheet plasma is heated by the viscous flow of surface currents produced by the solar wind. This heating increases the internal pressure and stretches the tail further. If the tail field lines are disrupted or if the pressure that can

---

[*] bright regions in the photosphere associated with sunspots

be sustained by the tail field lines is exceeded, heated plasma can be ejected Earthward as closed field lines are relaxed to a more dipolar shape carrying charged particles with them. Under normal magnetospheric conditions, substorms occur every 2 to 3 hours, however, during magnetic storms, they occur with greater frequency and intensity [76].

Major magnetic storms are closely associated with CMEs. A CME can arrive with any magnetic orientation; therefore, not all CMEs affect the Earth. Until recently, it was thought that the most violent solar events occur at Earth when the magnetic field lines embedded in the solar wind are directed southward enabling them to connect with those that surround the Earth. Using data from the THEMIS (Time History of Events and Macroscale Interactions) spacecraft and confirmed through simulations, Wenhui Li et al. discovered that twenty times more solar particles cross the Earth's leaky magnetic shield when the Sun's magnetic field is aligned with that of the Earth (i.e., northward direction) compared to when the two magnetic fields are oppositely directed. [77]

The most well known phenomenon associated with magnetic storms is the increase in the intensity and the distribution of the aurora. In fact, the auroras are a good gauge of the intensity of the solar wind. Other phenomena are higher levels of solar protons and heavy ions, redistribution of trapped particles, increased ring current, increased plasma electrons resulting in an increase in spacecraft charging and discharging [78], and power blackouts on Earth.

As with several other phenomena, the number of magnetic storm days shows the same cyclic variation as the solar activity level. Figure 7.2.2 [79] plots the number of sunspots for a 60-year period, indicating the level of solar activity. Plotted with the sunspot cycle is the number of geomagnetic storm days as measured by the A_p magnetic index. The correlation of the number of storm days with the level of solar activity is clear.

7.3 Solar Particle Variations

As one would expect, the intensity of high-energy solar particle events is closely associated with solar cycle variations. Figure 7.3.1 shows large solar proton events measured by the GOES series of spacecraft as a function of time. Superimposed on the graph is the sunspot cycle. Note that most solar energetic particle events occur during solar active times and that those that occur during solar inactive times have lower particle counts. Figure 7.3.2 from Dyer et al. [36] shows heavy ion LET spectra for some of the largest events for solar cycle 23 plotted with the background. For short periods of time during a solar event, the single event effect hazard induced by the solar heavy ions greatly exceeds the GCR hazard.

30

7.4 Galactic Cosmic Ray Variations

The galactic particles are always present; however, their intensities rise and fall slowly with solar activity cycles. The Sun modulates a set of local interstellar spectra at the outer boundary of the heliosphere [80]. The modulation can be defined by a single parameter, which is a function of distance from the Sun, the speed of the radial solar wind, and a radial transport particle diffusion coefficient. As with the trapped proton population, GCRs are at their peak level during solar minimum and at their lowest level during solar maximum. The length of the GCR modulation cycle is 22 years. The difference between the extremes of the solar minimum and maximum fluence levels is approximately a factor of 2 to 10 depending on the ion energy. Figure 7.4.1 shows the slow, long-term cyclic variation of the cosmic ray (C, N, O) fluences for a 20-year period as measured by the IMP-8 spacecraft. Superimposed on the GCR levels are unpredictable, sudden rises in the flux levels due solar energetic particles events.

7.5 Trapped Particle Variations

It was noted in Section 5.3 that the trapped particle populations are stable over long periods of time. However, when viewed on shorter time scale, trapped particle population levels and distribution in the magnetosphere are not static. The inner zone is a fairly stable population with the exception of the slow drift of the SAA (see Section 7.1). In contrast, the outer zone flux levels are dynamic to the degree that any variations due to solar cycle are masked by other dynamics. The variability can be over 6 orders of magnitude in the regions of L approximately 2.5 to 5.

One variation is the cyclic rise and fall of the fluence levels in response to the cyclic variation of the Sun's activity. The solar cycle has opposite effects on electron and proton levels. The electron and proton flux levels are lowered during the maximum phase of the solar cycle because the increased solar activity increases the atmospheric scale height. This, in turn, results in increased removal rates of trapped particles due to collisions. Hence, the proton population decreases during solar maximum as shown in Figure 7.5.1 which plots trapped protons fluxes as a function of time. At the same time that particles are being lost into the atmosphere, electrons are injected into the magnetosphere at greater rates during solar maximum increasing the electron levels above the atmospheric loss rates. Therefore, the net effect on the electrons during solar maximum is an increase in particle populations. The magnitude of this variation is not the same for all regions in the magnetosphere.

Other variations are superimposed on the changes caused by the cyclic nature of solar activity. Local time variations caused by the lack of azimuthal symmetry of the geomagnetic field for L > 5, and fluctuations caused by the rotation of the Sun. Figure 7.5.2 shows, the LT variation

becomes more marked with increasing L. A 27-day cyclic variation due to the rotation of the Sun is superimposed on the LT variations. This 27-day variation, as measured by the GOES spacecraft, can be seen in Figure 7.5.3.

The trapped particle levels and locations are highly dependent on particle energy, altitude, inclination, and the activity level of the Sun, and the levels are highly dynamic. The slot region between the inner and outer zones (2 < L < 2.8) and the outer zone (L >2.8) proton and electron populations can increase above averages by several orders of magnitude due to changes in the magnetosphere induced by solar and magnetic storms. Figure 7.5.4, a plot of measurements of trapped electrons over a 1-year period, shows changes in the extremely dynamic outer zone and the slot region filling periodically with storm electrons. Due to their complex distribution and dependence on long- and short-term solar variability, the trapped particle populations are difficult to model and forecast.

7.6   Atmospheric Environment Variations

The galactic cosmic rays are the primary particles that produce the secondary neutrons and protons in the atmosphere, therefore, it is the variations in the GCRs intensities that cause most of the variations observed in the secondary neutron and proton levels. For example, neutron levels rise and fall in the same 11-year solar cycle that modulates the GCRs. Also, the ability of a heavy ion to penetrate the magnetosphere is determined by its magnetic rigidity (see Section 3.4) which, in turn, is dependent on geomagnetic latitude. Magnetic disturbances occur more frequently during the active phase of the solar cycle increasing the ability of GCRs to penetrate the magnetosphere thereby increasing the levels of secondary particles. Atmospheric conditions, especially barometric pressure, also affect the neutron levels. In 1990, Dyer *et al.* demonstrated that the neutron levels were increased by 5-fold during the October 1989 solar events using measurements from the CREAM monitor on the Concorde [81].

Figure 7.6.1 shows the count rate in CREAM channel 1 (19fC to 46fC, LET 6.1 MeV cm^2 g^{-1}) plotted as monthly averages for the GV ranges 54,000-55,000 feet and 1-2 GV. The rates show a clear anticorrelation with the solar cycle and track well with the neutron monitor at Climax Colorado (altitude 3.4 km, cut-off rigidity 2.96 GV). The enhanced period during September and October 1989 comprised a number of energetic solar particle events observed by ground level, high latitude neutron monitors and the Concorde observations are summarized in Table 7.6.1 [84]. The enhancement factors are the ratios between flight- averaged count rates at greater than 50,000 feet during the solar particle events and the rates during immediately preceding flights on identical routes when only quiet-time cosmic rays were present. The charge-deposition thresholds of each of the channels are also given.

Dyer and Lei [60] calculated the neutron fluxes in the atmosphere during large solar particle events using Monte-Carlo radiation transport in conjunction with data from ground-level neutron monitors and space borne detectors. Some success has been obtained in fitting the results from Concorde and it has been demonstrated that such events can produce high rates of SEU, up to several hundred times the cosmic ray rates, for high latitude routes even at subsonic altitudes of less than 40,000 feet.

8 Model Development

When modeling, particles are treated as isotropic and omnidirectional with the exception of plasma, low altitude trapped protons (<500 km), and cosmic radiation on the ground. There are large spatial and temporal variations in the constituency and density of the environments; therefore, exposure to the environment is highly dependent on the location of the spacecraft.

8.1 Heavy Ion Models

8.1.1 Early Estimates

In 1965 when James Vette [82] compared the levels of solar "flare" protons and galactic cosmic rays based on work by H. H. Malitson and W. R. Webber [83], the primary concern was dose levels on spacecraft components, which was considered a non-issue in the presence of protons and electrons. Later, James Haffner discussed the concern for the GCR contribution to total dose on spacecraft in his 1971 [84]. He presented values for the levels of galactic cosmic rays and estimated that the expected GCR dose for the Grand Tour Missions[*] to the outer planets was in the range of a few hundred rads.

8.1.2 The Cosmic Ray Effects on Microelectronics (CREME) Code

After the discovery of cosmic ray induced single event upsets on microelectronic devices, a team at Naval Research Laboratory led by James Adams recognized the need for a comprehensive software package to calculate single event upset rates in space that integrated environment predictions with particle interaction models. They embarked on the task of

---

[*] The Planetary Grand Tour was an ambitious plan to send probes to the outermost planets of the solar system. The Grand Tour would have exploited the alignment of Jupiter, Saturn, Uranus, Neptune, and Pluto, an event that would occur in the late 1970s, and not recur for 176 years. A probe sent to Jupiter could use that planet as a gravitational slingshot to extend its trajectory to planets further out in the Solar System. The original proposed mission design had four probes. The first two, launched in 1976 and 1977, would fly by Jupiter, Saturn, and Pluto. The other two, launched in 1979, would fly by Jupiter, Uranus, and Neptune. NASA budget cuts eventually doomed the Grand Tour missions in 1972, as well as later proposals for a "mini grand tour". However, many elements of the Grand Tour were added to the Voyager program. The two Voyager probes, launched in 1977, were originally meant to fly by Jupiter and Saturn. But Voyager 2 used the fortunate alignments of the outer planets and was able to add close flybys of both Uranus and Neptune. Voyager 2's mission has specifically come to be regarded as the "Grand Tour."

developing a comprehensive computer tool that could be used by researchers and engineers. Due to the extent of the upset problem, the effort had to include compilation of data sets for GCR and solar heavy ion populations, development of GCR and solar heavy ion models, evaluation of solar proton data and models, development of magnetospheric cutoff calculations, analysis of spacecraft shielding effects, and development interaction models for upsets due to heavy ions and protons. Adams *et al.* produced two Naval Research Laboratory (NRL) Memorandum Reports, which reported on topics related to this task [85,86]. The first report, published in 1981, contained a comprehensive review of the near-Earth particle environment.

8.1.3   The CREME Heavy Ion Environment Models

The GCR environment model was based on data from several researchers collected through 1980. (see Adams [85]). Because of the dissimilar shape of their energy spectra, the hydrogen, helium, and iron ion distributions were treated as separate cases, and the other elements were scaled to one of the three spectra, as appropriate, using the relative abundances of the elements. Four different models of the GCR environment were developed, one of them being the well known "90% worst case environment".

The solar heavy ion environment was more difficult to model because of the unavailability of a good data set from spacecraft instrumentation. Adams *et al.* assumed that the solar particle events with the highest proton fluxes are always heavy ion rich and estimated fluence levels for the higher energy solar heavy ions (>1 MeV) by scaling the abundances to protons. Eight different models of the solar heavy ion environment were developed because, without the benefit of comprehensive space measurements, the authors had to account for all possible solar activity conditions.

8.1.4   Extending the Models to a Rate Prediction Tool – CREME86

In 1982 Adams *et al.* presented a paper [87] that, with a paper by Edward Petersen *et al.* [88], essentially laid the groundwork for the CREME86 code. This code was the first end-to-end desktop capability to calculate radiation environments throughout near-Earth regions and to use laboratory test parameters from devices to calculate the rate of a radiation effect. The simple title, "The Natural Radiation Environment Inside Spacecraft," does not reflect the complexity and groundbreaking nature of the work. The paper reviewed the work on the development of the environment models [85] and presented methods to calculate the transport of particles through the magnetosphere and through spacecraft shielding. The authors also showed the utility of using linear energy transfer (LET) spectra to represent the heavy ion environment in a form that condenses the energy spectra of all ions into a compact expression and that can be applied to calculating energy transfer in microvolumes. W. Heinrich constructed the first LET spectrum

34

describing the ion environment in space in 1977 for biomedical purposes [89] (see also [90]). In 1978 James Pickel and James Blanford showed the applicability of the LET spectrum to the single event upset problem in microelectronics [91]. The resulting CREME [92] code was first released in 1986.

CREME offered four different models of the GCR environment, specified in the code by the "M" input parameter. In 1992, it was recommended that only two of the four GCR models the old CREME code be used [93]. Because of mounting evidence that the anomalous component is singly ionized, the "M=2" environment option was considered inaccurate because it calculates a fully ionized anomalous component. Also, the "M=3" option or the so called "90% worst case environment" was no longer recommended as a standard environment for device comparisons. This environment calculates GCR spectra for peak solar minimum conditions and adds in particles from medium sized solar events with energies less than 100 MeV/nucleon. The additional fluence levels were determined such that instantaneous fluxes will occur with a 10% probability. (Larger events were modeled in the solar particle models of CREME.) These conditions only occur for very short time periods during a mission. Therefore, Petersen *et al.* [93] recommended that the "M=1" option for the peak of the solar minimum (YEAR = 1975.144) be used to provide fluxes for normal conditions and that the "M=4" option be used to calculate the solar minimum spectrum with the singly ionized component to predict worst case GCR levels. An uncertainty factor of 2 was defined for the models.

Peterson *et al.* also pointed out that the solar cycle modulation function is not correct because it is based on an 11-year modulation cycle and not the correct 22-year cycle. Other models of the GCR environment, including the CHIME model, [94] a model by Badhwar and O'Neill [95], and Boeing's MACREE [96], were developed with the goal of improving the solar cycle modulation of the GCRs. The CHIME model is based on measurements taken on the CRRES satellite. Besides the solar cycle modulation, the major difference between CHIME and the old CREME model is the particle flux database. The low energy enhancements resulting from medium solar events are not part of the CHIME GCR database. Instead, they are included in the solar particle event data. The GCR environment of the MACREE model is the same as that used in the old CREME package. The authors of the Badhwar and O'Neill model added measurements taken after 1980 to the GCR database.

8.1.5 *Updates to the CREME Code*
For ten years the CREME86 code was a standard for calculating heavy ion environments. As knowledge of the radiation environment increased, it became apparent that the CREME86 models could be improved. Using ISEE 3 data, Reames *et al.* [97] found an inverse correlation between

proton intensity and the iron/carbon heavy ion abundance ratio and that the composition of a solar particle event was a result of the location of the event on the Sun. This contradicted Adams' assumption that all solar events are He rich, meaning that the solar heavy ion models were probably over predicting. Dyer et al. [98] measured LET spectra during the March 1991 event with the CREDO instrument on UoSAT-3. When they compared the measurements with LET calculated using the CREME86 solar heavy ion models (Figure 8.1.5.1), they found that, in the LET range important for single event effects analyses, all of the models severely over-predicted the LET levels.

In the 1990s, NRL recognized the need to update the environment models in the CREME86 code. Tylka et al. [99] implemented the improved understanding of the GCR environment provided by Rikho Nymmik et al. (Moscow State University (MSU) model [100,101]) to simplify model selection. In the updated code (CREME96), the models choices are the highest level of GCRs (peak during solar minimum including the anomalous component) and the lowest levels of GCRs (during solar maximum). These two model choices define the upper and lower limits of the GCR environment in which a system must perform for a long mission. Also, users have the option of calculating GCR levels for a specific date. An improved solar cycle modulation function was added to the CREME96.

The most important update to the code was the solar heavy ion model. William Dietrich from the University of Chicago analyzed the solar heavy ion data from the IMP-8 satellite, providing a comprehensive set of solar heavy ion space data [43]. The data set was especially important for modeling the fluences at higher energies. A team led by Tylka used the results to model the solar heavy ions based on the October 1989 solar particle event. An analysis of 100 solar heavy ion events in the Dietrich database showed that this event could be used as a representative of a "worst-case" environment [99]. The CREME96 solar heavy ion estimates are significantly lower than the heavy ion models in CREME86. Figure 8.1.5.2 compares the LET energy spectra for the CREME86 and CREME96 solar heavy ion models.

The GCR environment model was also updated to include the analysis of the SAMPEX measurements of anomalous cosmic rays (ACRs). With the finding that the ACRs are not singly charged over energies of 20 MeV/nucleon, four models in CREME86 were replaced with one GCR model in CREME96.

8.1.6   Recent Models for Heavy Ion Environments

Since the early 1990s, O'Neill has made continuous improvements in the Badhwar-O'Neill model of GCRs. The most recent improvement is the inclusion of measurements of GCR energy spectra for 50-500 MeV/nucleon boron through nickel ions from the Cosmic Ray Isotope

Spectrometer (CRIS) on the Advanced Composition Explorer (ACE) These new data was used to update the original Badhwar – O'Neill Model and greatly improved the interplanetary GCR prediction accuracy. The updated model [102] was shown to be accurate to within 5%, for elements such as oxygen, which have sufficient abundance that over 1000 ions are captured in each energy bin within a 30 day period. The solar modulation parameter used in the updated model is based on the Climax neutron count, the IMP-8 (z > 8 channel 7), and the ACE oxygen ion flux for solar cycles 21, 22, and 23. A new approach by Davis *et al.* [103] at the California Institute of Technology (CIT) shows application of a cosmic ray interstellar propagation and solar modulation model provides an improved fit to the ACE measurements compared to radiation environment models currently in use. The Badhwar-O'Neill, MSU, and CIT models are compared with ACE measurements of carbon, oxygen, silicon, and iron ions in Figure 8.1.6.1.

A team led by Xapsos identified the concern that the solar heavy ion model currently in CREME96 does not have a true statistical basis and may misrepresent a worst case environment. Dyer *et al.* [104] made comparisons to the CREME96 worst case models and actual solar energetic particle events using measurements from the Cosmic Radiation Environment DOsimetry (CREDO) Experiment onboard the Microelectronics and Photonics Test Bed (MPTB). The data show that three major events during this time period approximately equaled the "worst day" model. An example of this is shown in Figure 8.1.6.2 for an event that occurred in November 2001.

Xapsos *et al.* developed a solar heavy ion model called Prediction of Solar particle Yields for CHaracterizing Integrated Circuits (PSYCHIC) [105]. It is a statistical model of cumulative solar heavy ion fluences during the solar maximum time period and is based on probabilistic methods, analysis of long-term satellite measurements of solar particle events, and current knowledge of the chemical composition and processes in the solar photosphere. It calculates solar particle energy spectra and LET spectra to be obtained for different mission time periods, levels of confidence and shielding. See Figure 4.2.4.5 for differential fluence-energy spectra for protons, alpha particles, oxygen, magnesium, iron and summed spectra for Z > 28 calculated with the PSYCHIC model.

8.2 Solar Proton Models

8.2.1 Early Estimates of Solar Proton Levels

In 1965 Vette compared the levels of solar "flare" protons and galactic cosmic rays based on work by Malitson and Webber [83] and noted that the solar protons are low during periods of low solar activity. He also pointed out that they were considered a serious hazard for astronauts on Apollo missions. To predict the solar proton environment for the Grand Tour Missions to the

outer planets, Haffner compiled all of the existing solar proton data at 1 AU for 1956-1968, including data from Webber, McDonald, Lewis, Modisette, and Mosley (see reference 83). He developed fitting functions to fill in missing data that described the onset, rise time, and decay of solar events as a function of time. He then reconstructed probable values based on sunspot numbers by using predictions of future sunspot numbers developed by Weddell and Haffner [106]. To estimate the diffusion of the solar protons throughout interplanetary space, Haffner assumed a spatial dependence of $1/r^2$ where r is measured in AU, which is an approximation still used today. The method was used to predict the expected solar particle environment for each year from 1970 to 1989. Haffner pointed out the large uncertainties in predicting solar particle levels.

8.2.2   The First Statistical Models

As concern grew over electronics and human exposure to solar protons and as the amount of available on-orbit particle measurements increased, the use of compilations of data for estimating solar proton levels was replaced by modeling efforts. In 1974 Joseph King [107] published the first statistical model for solar proton events using Poisson distributions. He concluded from his analysis of proton data from the 20th solar cycle that solar proton events could be classified into "ordinary" and "anomalously large". This was based on the fact that only one anomalously large event occurred in the 20th solar cycle, the August 1972 event. That event alone accounted for 84% of the total proton fluence in the solar cycle at energies E > 30 MeV. However, when Joan Feynman *et al.* [108] added cycles 19 and 21 data to the solar proton event database, they were able to conclude that individual solar proton events actually form a continuum of event severity from the smallest to the largest, blurring the distinction between ordinary and anomalously large events.

8.2.3   Engineering Oriented Statistical Models

Many large events similar to the August 1972 event occurred in cycle 22 increasing concern about the validity of the solar proton models. With the goal of improving the ability to address practical aspects of spacecraft reliability, a team led by Xapsos began compiling solar proton data for solar cycles 20, 21, and 22 and using statistical techniques to derive probability distributions of cumulative solar proton fluences. A review of the data sets can be found in Reference [109]. In 1996 Xapsos *et al.* [110] presented a paper that described the application of extreme value theory to determine probability of encountering a single large event over the course of a mission. They also used compound Poisson process theory to describe the probability of encountering various fluence levels during a mission. The work of the Xapsos team confirmed the Feyman conclusion that a "typical event" cannot be defined and was used as the basis to develop the Emission of Solar Protons (ESP) model. Later the team updated the model to include data covering the time

38

period from 1966 to 2001 and to extend the proton energy range to over 300 MeV (see PSYCHIC model [105]. Figure 8.2.3.1 shows a comparison of the King, Feynman, and Xapsos models.

Some missions are planned for times when the Sun is mostly in its inactive phase, i.e., during solar minimum. Usually, it is assumed that there are no solar events during that period which is not the case. Model developers have used Monte Carlo based approaches to parameterize the number of events that are predicted as a function of time throughout the solar cycle for predicting cumulative fluences during periods of low solar activity. One such model is that developed by Nymmik [111]. Xapsos et al. also analyzed solar minimum time periods and developed models for three average solar proton flux levels that allow varying degrees of conservatism to be used [112].

The Xapsos team also worked on understanding how to define the peaks of solar proton events. To accomplish this, they applied Maximum Entropy Principle (MEP) to select the least biased event probability distribution. The MEP, used for earthquake predictions, is valuable for analyzing incomplete data sets. They validated the results with Lunar Rock Records dating back to ancient times [113]. The Xapsos team continued their work by establishing worst case solar proton spectra for solar events [114]. When comparing their model with the CREME96 [99] "worst-week" solar proton model, which was based on the October 1989 solar particle event, they found that, statistically, the CREME96 model is closer to a 90% worst case event model [115]. Xapsos et al. combined the model elements into the Emission of Solar Protons (ESP) model, which is available as a computer code [115,116].

Solar particle intensity also varies with distance from the Sun. As particles move away from the Sun, the particles diffuse into the larger volume of space. Spacecraft near the Earth have provided us with a large data set of particles measurements so particle intensities are scaled as a function of distance from the Earth. (The Earth is at 1 AU or the distance between the Sun and the Earth). We know from Pioneer and Voyager measurements that the particle intensity varies by $1/r^2$ where r is in units of AU as move away from the Earth. Because we have so few measurements as we move closer to the Sun (less than 1AU), we are not certain about the variation of particle intensity. Estimates range from $1/r^2$ to $1/r^3$.

8.3 The Earth's Radiation Belts

8.3.1 The Beginnings of the Radiation Belt Modeling Program

The production of enhanced radiation levels by the Starfish explosion and others and the ensuing problem of shortened spacecraft lifetimes emphasized the need for a uniform, quantitative description of the trapped particle environment. Wilmont Hess of the National Aeronautics and Space Administration's (NASA's) Goddard Space Flight Center (GSFC)

developed the first empirical models of the trapped radiation belts. Using data from several satellites, he began constructing quantitative radiation models for inner zone protons and electrons. These models were designated as P1, P2, etc. and E1, E2, etc. Starting in 1962 and continuing through the late 1960s, several series of satellites were launched with instruments designed to measure the effects of Starfish, providing a large volume of particle data. In late 1963, James Vette of Aerospace Corporation and later of NASA/GSFC was appointed to lead a trapped radiation environment modeling program jointly funded by NASA and the United States Air Force (USAF). At that time, there were several groups actively involved in trapped particle measurements, including Aerospace Corporation, Air Force Cambridge Research Laboratory (now Phillips Laboratory), Johns Hopkins/Applied Physics Laboratory, Bell Telephone Laboratories, GSFC, Lawrence Livermore Laboratory, Lockheed Missile and Space Corporation, the University of California at San Diego, and the University of Iowa. Each organization agreed to make its measurements available to the modeling program.

In 1965 James Vette of the Aerospace Corporation presented an overview paper of the efforts to model the trapped radiation environment [117]. He referenced 31 papers from various scientific meetings and journals (AGU, Journal of Geophysical Research, etc., see reference 117) where measurements and modeling results had been presented. Vette reviewed the efforts to model the outer zone particles, stressing the difficulty of developing static maps of the dynamic electrons in that region. He compared the lifetimes of the outer particles (minutes) to those of the inner zone (years). As his paper demonstrates, the modulation of the electrons driven by the 27-day solar rotation period and the fluctuations connected with magnetic activity were known at that time. Rather than presenting maps of the dynamic outer zone, he gave "typical" integral spectra. It was known at the time that the protons in the outer zone are more stable, are more closely confined to the magnetic equator, and have a "soft spectrum". With respect to damage to spacecraft, he noted that outer zone protons affect only unshielded devices, but that electron exposure during long missions will result in measurable effects.

Vette presented the AE-1* map of the inner zone electron model and the newly developed AP maps for protons with energies greater than 4 MeV. He noted that the natural inner zone electron population was not well known before Starfish and that Starfish electrons dominated the population levels in regions below L of 1.8. He also stated that, before Starfish, protons up to several 100s of MeV dominated the inner zone. Interestingly, as an aside, Vette made reference to a then recent observation by McIlwain that a redistribution of protons at > 34 MeV followed a large magnetic storm in the L = 2-3 region [118].

---

*The "A" is for Aerospace Corporation where Vette first worked on the models.

8.3.2 Trapped Particle Model Development, 1960s, 1970s, 1980s

Eight trapped proton models, eight trapped electron models, and one Starfish decay model were released during the 27 years that the trapped radiation modeling program was operative. The trapped particle models that are most often used at this time are the AP-8 [55] for protons and the AE-8 [56] for electrons. The AP-8 model, released in 1976, was the culmination of a long-term effort to include all of the previous models under one common approach and to include all of the data after 1970. After 1977, the modeling budget was significantly reduced so a similar effort to consolidate the electron models into the AE-8 model was not completed until 1983. The formal documentation of that model was released in 1991.

The AP-8 and AE-8 models include data from 43 satellites, 55 sets of data from principal investigator instruments, and 1,630 channel-months of data. By the 1970s, scientific interest had shifted from trapped particles to the plasma regime to determine the physical mechanisms of particle energization and transport. As a result, the number of new data sets available for trapped radiation environment modeling was drastically reduced. It was not until the measurement of storm belts by the CRRES mission in 1991 that concerns were renewed about the ability to model the trapped radiation belts to sufficient accuracy for using modern microelectronics in space.

8.3.3 The Storm Belts - The CRRES Mission

A discussion of developments in our knowledge of the trapped radiation environment cannot be complete without including the contributions that were made by the CRRES mission. Not only did the mission provide data for radiation belt modeling, but it also rekindled interest in radiation belt science. The CRRES satellite carried a full complement of particle detectors, and its geosynchronous transfer orbit of 350 km perigee and over 30,000 km apogee at 18° inclination was ideal for measuring radiation belt particles. Unfortunately, the CRRES launch was too late to measure the large September and October 1989 solar events. However, CRRES was in operation for the second peak of solar cycle 22 and observed the largest magnetic event ever recorded in March of 1991. Analysis of data from the instruments on CRRES before and after the March 1991 magnetic storm showed extremely large redistributions of the trapped particle populations. Gary Mullen et al. [119] reported that the CRRES proton instrument had measured a new proton storm belt in the slot region (L = 2-3). In Figure 8.3.3.1 this belt is seen as a region outside of the inner zone belt of protons. In the 1996 Gussenhoven et al. [120] summarized all of the CRRES results including a review of this proton belt formation and the production of an electron storm belt during the same storm. Recall from Section 8.3.1 that in 1965 McIlwain previously reported that he had observed a redistribution of protons at E >34 MeV following a large magnetic storm in the L = 2-3 region.

41

8.3.4 European Space Agency (ESA) Model Improvements

Eamonn Daly *et al.* [67] identified errors in the NASA models and documentation, including a source code error in AP-8-MIN and the fact that the AZUR data set on which the AP-8-MAX is based covered a time span of 3 months, not 6 months. They also noted that the Space Shuttle and the Long Duration Exposure Facility (LDEF) satellite measured environments in low altitudes (300 to 500 km) were from 60 to 100% higher than those predicted by the AP-8 models. The authors determined that a large source of this error is due to the method used to interpolate between the B/B_0 values in the regions near the atmospheric cutoff. They developed an alternate interpolation method that increased the estimated fluxes by 10 to 40% bringing them closer to the measured levels. They also recommend that an additional L increment at the low L values be included in the models to give better resolution at steep gradients. This increased the estimated fluxes by about 40%. When these two refinements to the interpolation scheme were combined, the revised flux levels were much closer to the measured values. Daly's work renewed interest in improving the radiation belt models for applications to enabling and commercial off the shelf technologies, which can have very low radiation tolerance.

8.3.5 Radiation Belt Models with Improved Time Resolution

Analysis of the CRRES instrument and experiment data showed that not only is the environment extremely dynamic but also electronic parts respond to the short-term changes. The AP-8 and AE-8 radiation belt models, with their 4-6 year averages, were adequate for long mission durations and for long-term degradation effects. However, modern spacecraft and instrument systems have serious problems with short-term effects, such as, interference and data corruption. With a time resolution of 4-6 years, the radiation belt models place a serious restriction on the ability to address design and operation issues of space systems built with modern electronics. Several researchers have recognized the need for trapped particle models with finer time resolution.

Four empirical models were developed using CRRES data to estimate short term dynamic changes in the particle population, the CRRESPRO [121], CRRESELE [122], CRRESRAD [123], and APEXRAD [124]. While the models are based on data collected over a short 14-month period and during solar maximum conditions only, they give the most comprehensive picture available of the environment resulting from a geomagnetic storm.

Improvements were also made in the long-term time in the low altitude regions of the AP-8 model. Carl Pfitzer [125] plotted predicted flux values for low inclination orbits as a function of the average atmospheric density. From this index, he interpolated and extrapolated fluxes from the AP-8 and AE-8 models for solar activity conditions. Later Stuart Huston and Pfitzer [126]

42

analyzed proton instrument data from the CRRES and TIROS/NOAA satellites with the goal of developing a low altitude (<850 km) trapped proton model with variation over an entire solar cycle as a function of solar activity indices (see Figure 7.5.1). In 1998 Huston presented the first trapped proton model with true solar cycle variation [127]. The proton flux levels were determined by using the solar radio flux proxy for atmospheric heating and included the phase lag between rise and fall of flux levels and solar activity.

Recently, the Huston team joined efforts with Xapsos and others at GSFC to add statistical variations to the solar cycle driven model thereby adding confidence level information to proton levels [128]. This increases the ability to address trapped proton variations for spacecraft design and mission planning.

Daniel Heynderickx and Joseph Lemaire [129] also plotted model fluxes as a function of the average weighted density of the atmosphere (ns) that is encountered by a particle on its drift shell. They found that the relationship between ns and the AP-8 and AE-8 models fluxes is well ordered, especially at low L values. If a practical form for the ns calculation is developed, this method could lead to replacing B_0 with $B_0(ns)$ when accessing the AP-8 and AE-8 models, thereby reflecting solar activity effects. Using data from the proton instrument on the SAMPEX spacecraft, they also developed a trapped proton model with improved time resolution [130]. Figure 8.3.5.1 compares proton energy spectra for the AE-8, Huston et al., and Heynderickx et al. models.

In 2003, Boscher et al. published a model for electrons in geostationary regions of the Earth's radiation belts [131]. This model is the result of an international collaboration between ONERA, the French Research Laboratory, and the U.S. Los Alamos National Laboratory. The model is based on two and a half solar cycles of electron outer radiation belt measurements from Los Alamos National Laboratory geostationary satellites, covering the period 1976–2001. The measurements were cross calibrated between the satellite instruments and referenced to CRRES observations. The model takes into account the solar cycle variation. Since the release of the first geostationary electron model, two updates have been published [132,133]. The model is shown as a function of time for several energy levels in Figure 8.3.5.2.

Another model development was initiated because of the need to address the vulnerability of spacecraft materials to internal charging in geostationary electron environments. Since the threat from electrostatic discharges is related to the occurrence of flux enhancements, the standard mean flux models like the AE8 are not appropriate. The FLUMIC (Flux Model for Internal Charging) was developed to provide a worst case charging environment [134]. The latest version of the model relies heavily on data from the GOES/SEM and STRV-1b/REM instruments. The

43

FLUMIC model is included in the DICTAT internal charging tool [135]. Figure 8.3.5.3 shows a comparison of the comparison of "Worst Case" POLE, CRRESELE, and FLUMIC Models with the AE-8 Model.

In October 2004, the National Aeronautics and Space Administration's Living With a Star Program sponsored the "The Working Group Meeting on New Standard Radiation Belt and Space Plasma Models for Spacecraft Engineering (October 2004, College Park, MD)" [136]. The Workshop was organized and led by Janet Barth from NASA with co-leads from the Aerospace Corporation, the Air Force Research Laboratory, and the European Space Agency. Members of the international radiation belt and space plasma modeling community (industry, National Aeronautics and Space Administration, Air Force Research Laboratory, the Department of Defense, and the European Space Agency) attended, focusing on the development of the next generation of radiation belt models to replace the AP-8 and AE-8 models with the primary purpose for the development of new models is the reduction of risk and costs associated with the exposure of spacecraft components and instruments to the space radiation environment. The goals of the workshop were to report and document recent progress on radiation belt model development and to complete a roadmap for the development of new standard radiation belt and space plasma models for spacecraft engineering.

The most important result of the workshop was user community developed model requirements which were derived from the United States Space Technology Alliance's Space Environment and Effects Working Group and from the European Space Agency's Space Environment and Effects Program. Plenary sessions reviewed new developments in radiation belt models for protons and electrons, space plasma models, data set availability and calibration, and current and planned missions and instrumentation for space radiation environment modeling purposes. In total 35 presentations were given over three days. The workshop provided inputs to agencies for future investments, agreements on interagency cooperation, long-term modeling goals of the participants and their institutions, and community agreement on data set management and the model standardization process [137]. Also, two new models were proposed for data set review and standardization. The models cover critical regions in space for space agencies, military, and commercial spacecraft missions, namely, low altitude protons (a combination of the Huston and Pfitzer [127] and Heynderickx et al. models [130]) and geostationary electrons (the ONERA/Los Alamos "POLE" model 131). Both models have progressed through committee review and have been opened up for comments from the modeling community as a final step for standardization.

44

Since the NASA workshop in 2004, the National Reconnaissance Office (NRO), the Air Force Research Laboratory (AFRL), the Aerospace Corporation, Los Alamos National Laboratory (LANL) and the Naval Research Laboratory (NRL) formed a partnership in 2006 to produce an improved version of the trapped radiation belt and plasma models, the AE-9 and AP-9 for electrons and protons, respectively. This model upgrade will offer significant improvements in terms of the radiation hazards specified, accuracy and uncertainty quantification, spectral and spatial coverage, and time-correlated probability of occurrence statistics [138]. The goal of the program is to provide models that are applicable to a wide range of radiation effects problems (e.g., single event effects, spacecraft charging, plasma effects), unlike the AP-8 and AE-8 that were designed for long-term degradation of electronics.

A goal of the NASA's Living With a Star Program is to increase our knowledge of the radiation belts surrounding the Earth. NASA will launch two satellites (Radiation Belt Storm Probes) into the radiation belts to discover the fundamental physics underlying the source, loss, and transport processes that govern the levels of particles in the radiation belts. The data will be used to improve the AP-8 and AE-8 models and as a supporting data set for the development of the AP-9 and AE-9 models.

8.3.6 Dynamic Models – Space Weather Simulation

One of the most important conclusions from the CRRES program was that existing theory cannot explain the particle penetrations deep into the magnetosphere observed by McIlwain and Mullen et al. The frequency of occurrence of these atypical events is also unknown, therefore, applying current models to setting design and operational rad-hard requirements creates uncertainties that are impossible to quantify. Dynamic environment simulations are a method that could be used to address this issue. Boscher et al. [139] reviewed modeling techniques that provide computer generated models of trapped particle transport during storms. Bourdarie, Boscher, and others [140] have continued to develop a 4-D diffusion code (Salammbo) to calculate the transport of particles throughout the inner magnetosphere shown in Figure 8.3.6.1. They applied the code to several problems, including calculation of the transport of existing and injected particles during storms, determination of the ring current growth using calculations for both protons and electrons, and discovery of the process by which high energy particles are totally removed from the internal magnetosphere. Case studies have been validated using CRRES and STRV-1b measurements [141]. In the future the authors plan to drive the model with interplanetary magnetic field strength thereby greatly increasing the database for running the code and providing statistics for a range of conditions for a given time period.

45

Unlike other dynamic model developments that are focused strictly on space weather forecasting, one objective of the Salammbo model development program is to produce an engineering tool that will predict electron fluxes and their dynamics in Earth's radiation belts for the problems of spacecraft linked to the radiation environment for evaluating risks due to internal charging and discharges and total dose effects. The modeling effort considers electrons in the 50 keV to 10 MeV energy range. The model takes into account the radial diffusion by magnetic and electric field fluctuations, friction process by the thermospheric atoms and molecules, coulomb interactions with free and bounded electrons, wave-particle interactions (plasmaspheric hiss, whistlers, VLF), and synchrotron radiation losses. Figure 8.3.6.2 shows the results of a model simulation of a storm in the magnetosphere.

8.4 Trapped Radiation at Other Planets

After numerous missions to explore the Earth's radiation belts and interplanetary space, scientists became interested in exploring the outer planets. In 1971, Haffner [142] presented an overview of the solar "flare", galactic, and magnetically trapped particle radiation expected during missions to the four outer planets, Jupiter, Saturn, Uranus, and Pluto. He estimated the environment levels from data and models and predicted mission doses. The ability to predict the environments at the outer planets was greatly hampered by the lack of measurements of the interplanetary environment beyond 1 AU and by the lack of any measurements of the trapped radiation environments of Jupiter and Saturn.

Haffner presented estimates of the trapped radiation belts of Jupiter and Saturn. It was theorized that Jupiter and Saturn had belts similar to those of the Earth based on decametric (bursts) and decimetric (quasi-steady state) radio frequency radiation emitted by Jupiter and Saturn. Similar rf radiation emission was measured from the Earth's belts. The decimetric radiation is due to synchrotron emission of the electrons trapped in the magnetic field, the decametric radiation is associated with one of Jupiter's moons, Io. Based on assumptions about the limiting particle fluxes, similar relationships in Jupiter's and Earth's magnetic fields, and particle and plasma densities and by ignoring the effect of the planet itself, Haffner derived relationships between the magnetic field at Jupiter's equator, the particle density relative to the plasma stability limit, and the effective inner radius of the Jovian belts. From that set of parameters, the electron dose rates for mission flybys were estimated.

The same methodology could not be applied to trapped protons because they do not radiate as the electrons do. Haffner pointed out that theory explaining the source and loss mechanisms for protons or electrons in the Earth's belts that could be applied to estimating the proton belts of Jupiter did not exist. Therefore, he had to base the proton estimates for Jupiter and Saturn on the

ratios of the protons/electrons in the Earth's Van Allen belts. He used these estimates to calculate doses for the missions.

In 1972 Kase followed up Haffner's work with a presentation that focused on concerns about displacement damage on spacecraft electronics due to proton and neutron environments [143]. In addition to natural sources, Kase presented the problem posed by having neutron emitting radio-isotope thermoelectric generators (RTGs) on board spacecraft. Kase also revisited the problem of modeling the proton belts of Jupiter. By that time, Divine had developed nominal and upper limit models of the proton belts [144]. The three orders of magnitude difference between the two models was an indication of the inaccuracy inherent in the unvalidated theoretical approach. It was expected that the proton spectra were "very hard" near the surface of Jupiter and softer at great distances.

8.4.1 Measurements of the Grand Tour Mission

The Pioneer missions to the outer planets carried instruments to measure the radiation environment. The measurements showed that the radiation was orders of magnitude higher than expected. Peak intensities of electrons in the belts, as measured by Pioneer 10, were 10,000 times greater than Earth's maximum. Also, the electron energies were found to be greater than 20 MeV. Protons were several thousand times as intense as Earth's belts. The inner radiation belts of Jupiter, as measured by Pioneer 10, had the highest radiation intensity so far measured, comparable to radiation intensities following an explosion of a nuclear device in the upper atmosphere. Pioneer 11 confirmed these high intensities. In the inner region of the magnetosphere high energy protons exceeding 35 MeV appear to peak in two shells; the outer shell was detected at 3.5 Jovian radii by Pioneer 10, and confirmed by Pioneer 11, and an inner shell, discovered by Pioneer 11, has a peak at 1.78 radii of Jupiter. Pioneer 11 also found that there is a greater flux of energetic particles at high Jovian latitudes than would have been expected from the measurements made by Pioneer 10. It also discovered that the flux of energetic particles peaks on either side of the dipole magnetic equator [145]. This discovery led to the need to retrofit the Galileo spacecraft with radiation hardened bipolar processors, because the spacecraft design with unhardened processors had been fixed before the arrival of the Pioneer spacecraft at Jupiter [146]. The models of the Jupiter radiation environment were updated using data from the missions to the outer planets [147].

Saturn also has radiation belts; however they are not nearly as intense as those of Jupiter because the rings around Saturn deplete the particle levels near where their peak would occur. Measurements from instruments on the Cassini spacecraft were used to improve the SatRad model which was originally based on data from the Pioneer and Voyager missions.

8.4.2 Models Post-Galileo

Insoo Jun *et al.* [148] used measurements of the high-energy, omni-directional electron environment taken by the Galileo spacecraft Energetic Particle Detector (EPD) to develop the Galileo Interim Radiation Electron (or GIRE) model of Jupiter's trapped electron radiation in the jovian equatorial plane for the range 8 to 16 Jupiter radii (1 jovian radius = 71,400 km). Ten-minute averages of these data formed an extensive database of observations of the jovian radiation belts between Jupiter orbit insertion (JOI) in 1995 and 2002. These data were then averaged to provide a differential flux spectrum at 0.174, 0.304, 0.527, 1.5, 2.0, 11.0, and 31 MeV in the jovian equatorial plane as a function of radial distance. This omnidirectional, equatorial model was combined with the original Divine model of jovian electron radiation to yield estimates of the out-of-plane radiation environment. The GIRE model was used to the total dose for the Europa mission, and it was found that the prediction of the GIRE model is about a factor of 2 lower than the Divine model estimate over the range of 100 to 1000 mils (2.54 to 25.4 mm) of aluminum shielding, but exceeds the Divine model by about 50% for thicker shielding (see Figure 8.4.2.1). Though GIRE covers the equatorial plane of Jupiter, it can be extended by assuming the pitch-angle distribution provided by the Divine and Garrett model. It applies for electrons with energies from 0.5 to 30 MeV [149].

A model is based on the Earth Salammbo code, developed by ONERA/DESP, was adapted for the Jupiter radiation belts. It has been validated for protons and electrons for radial distances from the planet's surface up to the orbit of Europa [149]. The spatial range of the model extends from the surface to $L = 9.5$ for the electrons and $L = 6$ for the protons. It includes electrons and protons with energies from 1 to 600 MeV and 1 MeV to 1 GeV respectively.

8.5 Atmospheric Radiation

Two coordinate systems are commonly used to define the neutron distributions, energy-altitude-latitude and energy-atmospheric depth-magnetic rigidity. Taber and Normand [150] developed an empirical model in the energy-altitude-latitude system based on studies by Mendall and Korff [151], Armstrong [152], and Merker *et al.* [153]. A model by Wilson-Nealy [154], based on the energy-atmospheric depth-magnetic rigidity system, is more recent and more comprehensive, but it is not as easy to use as the older model. Taber and Normand believe that the older energy-altitude-latitude model is sufficiently accurate for microelectronics applications. Figures 8.5.1, 8.5.2, and 8.5.3 represent the Taber and Normand model and also show the energy, altitude, and latitude dependencies of the neutron environment.

Using the AIRPROP code [155], Dyer *et al.* have shown that cosmic rays and their secondary fragments are not the major contribution to SEUs at aircraft altitudes [156]. Later work [157]

concentrated on explaining both the altitude dependence and the energy deposition spectra using a microdosimetry code extension to the Integrated Radiation Transport Suite. Figure 8.5.4 shows that atmospheric secondary neutrons are the major contribution but that ions start to become important at the highest altitudes. Figure 8.5.5 shows that at 30,000 feet the charge deposition spectrum is dominated by neutron interactions at the high end while energetic secondary electrons and muons contribute to the low channels. The work of Normand *et al.* [158] arrived at similar conclusions on the neutron contribution by scaling results of irradiation of silicon detectors obtained at a spallation neutron source.

9   Role of Space Environment Definition in Increasing Reliability

Radiation hardness assurance for space systems is accomplished by addressing the effects of radiation on reliability throughout the mission life cycle. Preventative measures and operational workarounds are considered during the concept, planning, design, launch, operations, and anomaly resolution phases. Note in Table 9.1.1 that mitigation measures for all space environment effects must be started in early mission phases. The pre-launch phases are the most effective time to prevent anomalies because technology selection and system design techniques can be used to minimize risk. However, for most missions, some level of "residual risk" must be assumed due to cost constraints, increasing complexity of space systems, unknowns in the space environment, and/or unknowns in space environment effects mechanisms. Possible consequences of the residual risk on spacecraft health and safety and on degradation of service must be evaluated and mitigated by writing operational countermeasures for spacecraft operators and instructing the operators on how to use them effectively.

Space environment definition needs change dramatically as the mission passes from risk minimization to risk management modes, i.e., from pre-launch to launch and operations. Figure 9.1 shows the important role that space climate and space weather models play in increasing spacecraft reliability throughout the mission. Statistically based specification or "climate" models are used for the design phase, which includes system design and mission planning. The operation phase requires "forecasting" models for protecting the systems investment, for mission planning, and for personnel scheduling. The third type of model for "nowcasting" the environment is used to resolve anomalies so risk can be reassessed for both the operating systems and for other systems that are in development. More details on each phase are given in the sections below.

9.1   Space Environment Definition - Pre-launch

Space environment models that are used in pre-launch phases of mission development need to specify the environment, i.e., they must describe the space climate in which the spacecraft will

49

operate over its lifetime. Below is a description of the factors that are taken into account during pre-launch and the space environment information that is required to develop design accommodations.

Issues that are addressed during the mission concept phase include observation requirements, observation vantage points, and development and validation of primary technologies. Required capabilities at this stage are integrated mission design tools, which include space climate models that can simulate the space environment throughout the solar cycle. The minimum requirements of the models are that they should represent long term variation over the solar cycle with at least 1-month resolution, provide worst case estimates, provide confidence levels and represent the environment in a broad energy range so they are applicable for surface materials to deeply embedded sensors. Spatial resolution is also required so that trades between vantage points can be considered.

Issues that are addressed during the mission-planning phase are observation requirements, mission success criteria, architecture trade studies, and risk acceptance criteria. Most accommodations for space environment effects are implemented during mission design including component selection and testing, subsystem design, shielding requirements, grounding, error detection and correction, and estimates of observation loss. Mission planning and design phases require similar environment information. Time distributions of levels of activity are needed to estimate lost observation time from instrument interference and data corruption. Worst-case levels of the space environment are also required for determining the survivability of components and the level of required error mitigation. To guide decisions on the acceptable level of risk, confidence levels for the space climate models are required and the capability of forecasting models for specific environments of concern should be assessed. One of the most critical features of the space climate models is that they cover an energy range that is adequate for addressing degradation or interference from the surface (e.g., thermal control materials) to heavily shielded systems (e.g., detectors).

9.2 Space Environment Definition - Launch and Operations

Good engineering practice is not a guarantee that a spacecraft that will be 100% free from vulnerabilities from the space environment. As mentioned above, this is due to cost constraints, lack of knowledge of the development team, increasing complexity of space systems and technologies, unknowns in the space environment, and unknowns in space environment effects mechanisms. As a result, spacecraft are often vulnerable to increases in space environment levels during space storms. Therefore, launch and operation phases require models that can forecast changes in levels of the space environment due to space storms to protect the space-based asset

.50

by shutting down systems or avoiding risky operations, such as, maneuvers, system reconfiguration, data download, or re-entry. The minimum requirements of these models are spatial coverage from interplanetary to low Earth orbits, information about the level of severity of storms, forecasts of quiet times for maneuvers and on-board operations, and must be specific to effects on technologies. The need to forecast quiet times is as important as forecasting storms to give operators "windows" during which these risky operations can be performed. Spacecraft operation facilities find it useful to be able to schedule extra personnel when space storms are expected. Forecasts must be specific to the region, the particle population, and the energy range.

9.3   Space Environment Definition - Anomaly Resolution

If an anomaly occurs, it is critical to be able to restore a space-based system to normal operations quickly regardless of the service provided by the system. Often this is accomplished before resolution of the anomaly. However, it is desirable to understand the root cause of the anomaly as soon as possible to prevent further disruption of the mission or prevent possible damage to the system. Once the anomaly is resolved, the risk to the mission is reevaluated and operational countermeasures and design guidelines are updated as required. Note that it is not unusual for anomalies to be unresolved, usually due to a lack of information about the local environment at the time of the anomaly or inability to pin-point the component and/or system where the anomaly originated. Health and safety monitoring on the spacecraft may be inadequate to pinpoint the system component that was sensitive to the space environment hazard. Frequently the space environment hazard is inadequately defined in terms of spatial resolution or energy and particle resolution. Spacecraft for science missions often have data that are valuable for anomaly resolution; however, timely access to that data is generally an impediment.

9.4   Model Requirements Summary

Space environment models play a crucial role in developing reliable spacecraft throughout the mission life cycle. Model requirements change dramatically when a mission moves from pre-launch phases to launch and operations. The need for space weather models to manage residual risk during launch and operational phases is clear. However, space "climate" models are equally important because of their crucial role in minimizing risk in pre-launch phases of missions. Table 9.4.1 summarizes the characteristics that models need to have to be useful for space environment mitigation.

Large uncertainty factors in environment definition translate to large design margins. The direct result is reduced system resources due to increased shielding, higher mitigation overhead, and/or the use of less capable components. Unknowns in space environments and effects translate

directly into large design margins because of the need to reduce risk. Design margins increase overhead on systems, reducing capability, and can preclude the use of newer technologies in spacecraft systems.

10 Summary

The state of the knowledge of the space and atmospheric radiation environments was reviewed and found that the success of modeling efforts to produce models of the radiation environment that are useful for engineering applications is dependent on our knowledge of the environment, the availability of appropriate data for modeling, and funds for modeling and validation. We also saw that basic science research often is used to derive the definitions required for understanding radiation effects and for developing models that are useful for designing radiation hardened systems. Over the past ten years, there has been increasing concern about the slow pace of the development of radiation environment models and the lack of an authorizing entity to evaluate the interim models that have been developed. Recently, organizations worked together to develop requirements for new radiation environment models. Efforts include reviews of potential data sets for modeling, definition of requirements for engineering models, and reviews of current modeling efforts with assessments of interim models. Appendix A gives a summary of the interim models that are being implemented by spacecraft designers to address the deficiencies of the *de facto* models.

Appendix A

Below is a summary of the *de facto* models and models that are sometimes used to fill in their deficiencies. Table A.1 gives the energy ranges for the trapped particle models.

De facto model for trapped protons: AP-8
- Combined Release and Radiation Effects Satellite PROton Model (CRRESPRO)
  - Brautigam *et al.* sponsored by US Air Force Research Laboratory (AFRL)
- Low Altitude Trapped Radiation Model (LATRM)
  - Huston *et al.* sponsored by NASA
- Trapped Proton Model-1 (TPM-1)
  - Huston *et al.* sponsored by NASA and AFRL
- SAMPEX/PET Model (PSB97)
  - Heynderickx *et al.* sponsored by ESA

De facto model for trapped electrons: AE-8
- Combined Release and Radiation Effects Satellite ELEctron Model (CRRESELE)
  - Gussenhoven *et al.* sponsored by Air Force Research Laboratory (AFRL)
- FLUx Model for Internal Charging (FLUMIC)
  - Wrenn et *al.* sponsored by ESA
- Particle ONERA-LANL Environment Model (POLE)
  - Bourdarie *et al.* sponsored by ONERA, Los Alamos National Laboratory (LANL), and NASA

De facto models for solar protons: JP91 for cumulative fluence, CREME86/96 for worst case event fluence
- Solar Particle Event Fluence Model (SPE Fluence Model)
  - *Nymmik et al.* sponsored by Moscow State University
  - Based on power function distributions of event fluences
- Emission of Solar Proton Model (ESP)
  - Xapsos *et al.* sponsored by NASA
  - Based on satellite data from the 21 solar maximum years during solar cycles 20-22
  - Uses Maximum Entropy Principle to generate an optimal selection of a probability distribution, and Extreme Value theory to estimate worst case
  - Calculates cumulative and worst case solar proton fluences
- PSYCHIC
  - Xapsos et al. sponsored by NASA
  - ESP Model with satellite data set extended to cover the time period of 1966 – 2001
  - Energy range extended to over 300 MeV
  - Includes estimates for solar minimum spectra

De facto model for GCR heavy ions: CREME86
- Galactic Cosmic Ray (GCR) Model from Moscow State University (MSU)
  - Solar variation is modeled with diffusion-convection theory of solar modulation
- Cosmic Ray Effects in MicroElectronics (CREME96)
  - CREME86 was updated with the GCR MSU Model
- NASA GCR Model from Badhwar and O'Neill

- o Similar approach to GCR MSU model with different implementation of the solar modulation theory
- New approach by Davis et al. at the California Institute of Technology (CIT)
  - o Uses transport model for the GCRs through the galaxy preceding the penetration and subsequent transport in the heliosphere

De facto model for solar heavy ions: CREME86
- CRRES/SPACERAD Heavy Ion Model of the Environment (CHIME) – Chenette *et al.* sponsored by US AFRL
  - o Heavy ion abundances scaled to protons results in overestimates
- Modeling and Analysis of Cosmic Ray Effects in Electronics MACREE) – Majewski *at al.* sponsored by Boeing
  - o Heavy ion abundances scaled to alphas results in less conservative estimates
- CREME96
  - o Uses the October 1989 event as a worst case
  - o Most extensive heavy ion measurements are for C, O, and Fe, and remaining elemental fluences are determined from a combination of measurements in 1 or 2 energy bins and abundance ratios
- PSYCHIC
  - o Xapsos *et al.* sponsored by NASA
  - o Has statistical ranges for worst case spectra

Table A.1: Summary of New Trapped Particle Models

Model Name	# of Years of Data	Spatial Coverage	Energy Range (MeV)	Data Source
CRRESPRO	1.2	1.15 < L < 5.5	1 < E < 100	CRRES
LATRM	17	< 1000 km	16 < E < 80	TIROS/NOAA
TPM-1	Depends on Region	1.15 < L < 5.5	1 < E < 100	CRRES, TIROS/NOAA
PSB97	4	1.1 < L < 2.0	18.5 < E < 500	SAMPEX
CRRESELE	1.2	2.5 < L < 6.8	0.5 < E < 6.6	CRRES
FLUMIC	11	Outer Zone	0.2 < E < 5.9	Various
POLE	25	Geostationary	0.03 < E < 6.0	LANL Instruments

REFERENCES

[1] E. G. Stassinopoulos, 1990 IEEE NSREC Short Course, "Microelectronics for the natural radiation environments of space, Chapter I: Radiation Environments of Space," July 16,1990, Reno, Nevada

[2] J. L. Barth, 1997 IEEE NSREC Short Course, "Applying computer simulation tools to radiation effects problems, Section II: Modeling space radiation environments," 21 July 1997, Snowmass Village, Colorado.

[3] C. S. Dyer, 1998 IEEE NSREC Short Course, "Radiation effects in the new millennium – Old realities and new issues, Section II: Space radiation environment dosimetry," July 20, 1998, Newport Beach, California.

[4] J. Mazur 2002 IEEE NSREC Short Course, "Radiation effects - from particles to payloads, Section II: The radiation environment outside and inside a spacecraft," July 15, 2002, Phoenix, Arizona.

[5] W. I. Axford and S. T. Suess, "Spacecraft to explore the outer heliosphere," Eos, Transactions American Geophysical Union, Vol. 75, No. 50, Page 587, 1994.

[6] International Association of Geomagnetism and Aeronomy, http://www.ngdc.noaa.gov/IAGA/vmod/.

[7] Community Coordinated Modeling Center (CCMC), NASA/Goddard Space Flight Center, http://ccmc.gsfc.nasa.gov/modelweb/.

[8] SPace ENVironment Information System (SPENVIS), European Space Agency General Support Technologies Programme (GSTP) by the Belgian Federal Science Policy Office, http://www.spenvis.oma.be/spenvis/help/background/magfield/magfield.html.

[9] N. A. Tsyganenko and A. V. Usmonov, "Determination of the Magnetospheric Current System Parameters and Development of Experimental Geomagnetic Field Models Based on Data from IMP and HEOS Satellites," Planet. Science, Vol. 30, No. 10, pp. 985-998, 1982.

[10] C. E. McIlwain, "Magnetic Coordinates," Radiation Trapped in the Earth's Magnetic Field, Proc. of the Advanced Study Inst., edited by B. M. McCormac, pp. 45-61, Bergen, Norway, August 16-September 3, 1965.

[11] A. Hassit and C. E. McIlwain, "Computer Programs for the Computation of B and L," NSSDC 67-27, National Space Science Data Center, NASA, Greenbelt, MD, May 1967.

[12] Gussenhoven, M.S., E. G. Mullen, and D. H. Brautigam, "Improved Understanding of the Earth's Radiation Belts from the CRRES Satellite," IEEE Trans. on Nucl. Science, Vol. 43, No. 2, April 1996.

[13] D. F. Smart and M. A. Shea, "Galactic Cosmic Radiation and Solar Energetic Particles," Chapter 6 in Handbook of Geophysics and the Space Environment, p. 6-10 edited by A. S. Jursa, Hanscom, AFB, MA, 1985.

[14] C. Störmer, "Periodische Elektronenbahnen im Felde eines Elementarmagneten und ihre Anwendung auf Brüches Modellversuche und auf Eschenhagens Elementarwellen des Erdmagnetismus," Z. Astrophys., Vol. 1, pp. 237-274, 1930.

[15] M. Roth, "The Geomagnetic Cutoff", Chapter 6, p. 6-5 in Handbook-Development of Improved Models of the Earth's Radiation Environment, Technical Note 1: Model Evaluation, June 28, 1989.

[16] M. A. Shea and D. F. Smart, "A World Grid of Calculated Cosmic Ray Cutoff Vertical Rigidities for 1980.0," 18th International Cosmic Ray Conference, Conference Papers, 3: 415, 1983.

[17] J. H. Adams, Jr., R. Silberberg, and C. H. Tsao, "Cosmic Ray Effects of Microelectronics, Part I: The Near-Earth Particle Environment," NRL Memorandum Report 4506, August 25, 1981.

[18] A. H. Taber and E. Normand, "Single Upset in Avionics," IEEE Trans. on Nucl. Science, Vol. 40, p 120, December 1993.

[19] E. Normand, "Single Event Effects in Avionics," IEEE Trans. on Nucl. Science, Vol. 43, No. 2, pp. 461-474, April 1996.

[20] J. W. Wilson, L. W. Townsend, W. Schimmerling, G. Khandelwal, F. Khan, J. E. Nealy, F. A. Cucinotta, L. C. Simsonsen, J. L. Shinn, J. W. Norbury, "Radiation Safety in the Earth's Atmosphere," in NASA RP-1257, Transport Methods and Interactions for Space Radiations, p. 519, December 1991. (for corrections to some model coefficients, see Reference 21)

[21] E. Normand and T. J. Baker, "Altitude and Latitude Variations in Avionics SEU and Atmospheric Neutron Flux," IEEE Trans. on Nucl. Science, Vol. 40, No. 6, pp. 1484-1490, December 1993.

[22] R. A. Millikan, Presentation before the National Academy of Sciences, November 9, 1925, Madison, Wisconsin.

[23] P. J. McNulty, "Single event effects experienced by astronauts and microelectronic circuits flown in space," *IEEE Trans. on Nucl. Sci.*, vol. 43, no. 2, pp. 475-482, April 1996.

[24] D. Binder, E. C. Smith, and A. B. Holman, "Satellite anomalies from galactic cosmic rays," *IEEE Trans on Nucl. Sci.*, vol. 22, no. 6, pp. 2675-2680, December 1975.

[25] P. Meyer. R. Ramaty, and W. R. Weber, "Cosmic rays - astronomy with energetic particles", *Physics Today* vol. 27, no. 10, 23 1974.

[26] M. O. Burrell and J. J. Wright, The estimation of galactic cosmic ray penetration and does rates," NASA TN D-6600, March 1972.

[27] J. W. Cronin, T. K. Gaisser, and S. P. Swordy, "Cosmic Rays at the Energy Frontier," Scientific American, January 1997.

[28] Uchiyama et al. Science Magazine, October 2007.

[29] R. A. Medwadlt, "Elemental Composition and Energy Spectra of Galactic Cosmic Rays," Proc. from Conference on Interplanetary Particle Environment, JPL Publication 88-28, pp. 121-132, JPL, Pasadena, CA, April 15, 1988.

[30] R. B. McKibben, "Gradients of Galactic Cosmic Rays and Anomalous Components," Proc. from Conference on Interplanetary Particle Environment, JPL Publication 88-28, pp. 135-148, April 15, 1988.

[31] D. F. Smart and M. A. Shea, "Galactic Cosmic Radiation and Solar Energetic Particles," Chapter 6 in Handbook of Geophysics and the Space Environment, p. 6-10 edited by A. S. Jursa, Hanscom, AFB, MA, 1985.

[32] Scott E. Forbush, "Three Unusual Cosmic-Ray Increases Possibly Due to Charged Particles from the Sun," Phys. Rev. 70, 771 - 772 (1946).

[33] J. Van Allen, The National Academies Press, Biographical Memoirs, Scott E. Forbush, http://www.nap.edu/readingroom.php?book=biomems&page=sforbush.html

[34] R. Harboe-Sørensen, E. J. Daly, C. I. Underwood, J. Ward, and L. Adams, "The Behaviour of Measured SEU at Low Altitude During Periods of High Solar Activity," IEEE Trans. on Nucl. Science, Vol. 37, No. 6, pp. 1938-1943, December 1990.

[35] L. Adams, E. J. Daly, R. Harboe-Sørensen, A. G. Holmes-Siedle, A. K. Ward, and R. A. Bell, "Measurements of SEU and Total Dose in Geostationary Orbit Under Normal and Solar Flare Conditions," IEEE Trans. on Nucl. Science, Vol. 38, No. 6, pp. 1686-1692, December 1991.

[36] C. S. Dyer, K. Hunter, S. Clucas, and A. Campbell, "Observation of the Solar Particle Events of October and November 2003 from CREDO and MPTB,' IEEE Transactions On Nuclear Science, VOL. 51, No. 6, pp. 3388-3393, December 2004.

[37] "Solar Sentinels: A Mission Study Report," prepared for NASA by the Johns Hopkins Applied Physics Laboratory, February 2008.

[38] J. T. Gosling, "The Solar Flare Myth," J. of Geophysical Research, Vol. 98, No. A11, pp. 18,937-18,949, November 1, 1993.

[39] D. V. Reames, "Solar Energetic Particles: A Paradigm Shift," Revs. Geophys. (Suppl.), 33, 585, 1995.

[40] H. V. Cane, D. V. Reames, and T. T. von Rosenvinge, "The Role of Interplanetary Shocks in the Longitude Distribution of Solar Energetic Particles," J. of Geophys. Res., 93, 9555, 1988.

[41] Wibberenz, G., and H. V. Cane, Multi-spacecraft observations of solar flare particles in the inner heliosphere, Astrophys. J., 650, 1199, 2006.

[42] M. A. Xapsos, C. Stauffer, T. Jordan, J. L. Barth, and R. A. Mewaldt, "Model for Cumulative Solar Heavy Ion Energy and Linear Energy Transfer Spectra," IEEE Transactions On Nuclear Science, VOL. 54, NO. 6, December 2007.

[43] A. J. Tylka, W. F. Dietrich, and P. R. Boberg, "Probability distributions of high-energy solar-heavy-ion fluxes from IMP-8: 1973-1996," IEEE Trans. Nucl. Sci., vol. 44, no. 6, pp. 2140–2149, Dec. 1997.

[44] I. A. Daglis, *Space Storms and Space Weather Hazards*, vol. 38, Chapter 3, Kluwer Academic Publishers, 2001.

[45] J. A. Van Allen, C. E. McIlwain, and G. H. Ludwig, "Radiation observations with satellite 1958 .X, *J. Geophys. Res.* Vol. 64, pp. 271-286, 1959a.

[46] J. I. Vette, "The NASA/National Space Science Data Center trapped radiation environment model program (1964-1991)," NSSDC 91-29, NASA/Goddard Space Flight Center, National Space Science Data Center, Greenbelt, MD, November 1991.

[47] M. J. Teague and E. G. Stassinopoulos, "A model of the starfish flux in the inner radiation zone," X-601-72-487, NASA/Goddard Space Flight Center, Greenbelt, MD, December 1972.

[48] W. N. Spejeldvik and P. L. Rothwell, The Radiation Belts, Chapter 5 in Handbook of Geophysics and the Space Environment, p. 5-1 - 5-55 edited by A. S. Jursa, Hanscom, AFB, MA, 1985.

[49] L. Störmer, Polar Aurora, Clerendon, Press, Oxford, 1955.

[50] H. Alfvén and C. G. Fälthammar, Cosmical Electrodynamics, Clarendon Press, Oxford, 1963.

[51] J. G. Roederer, Physics and Chemistry in Space, Vol. 2, Dynamics of Geomagnetically Trapped Radiation, Springer-Verlag, New York, 1970.

[52] M. Schulz and L. J. Lanzerotti, Physics and Chemistry in Space, Vol. 7, Particle Diffusion in the Radiation Belts, Springer-Verlag, New York, 1974.

[53] A. L. Vampola, "Solar Cycle Effects on Trapped Energetic Particles," Journal of Spacecraft and Rockets, pp. 416-427, Nov-Dec 1989.

[54] D. Boscher, S. Bourdaire, and T. Beutier, "Dynamic Modeling of Trapped Particles," IEEE Trans. on Nucl. Science, Vol. 43, No. 2, pp. 416-425, April 1996.

[55] D. M. Sawyer and J. I. Vette, "AP-8 trapped proton environment for solar maximum and solar minimum," NSSDC/WDC-A-R&S, 76-06, NASA/Goddard Space Flight Center, Greenbelt, MD, December 1976.

[56] J. I. Vette, "The AE-8 trapped electron model environment," NSSDC/WDC-A-R&S 91-24, NASA/Goddard Space Flight Center, Greenbelt, MD, November 1991.

[57] S. A. Korff, "Cosmic-Ray Neutrons," American Journal of Physics, Volume 19, Issue 4, pp. 226-229, April 1951.

[58] C. H. Tsao, R. Silberberg, and J. R. Letaw, "Cosmic Ray Heavy Ions At and Above 40,000 Feet," IEEE Trans. on Nucl. Science, Vol. 31, No. 6, pp. 1066-1068, December 1984.

[59] R. Silberberg, C. H. Tsao, J. R. Letaw, "Neutron Generated Single Event Upsets," IEEE Trans. on Nucl. Science, Vol. 31, No. 6, pp. 1183-1185, December 1984.

[60] C. S. Dyer, A. J. Sims, J. Farren, and J. Stephen, "Measurements of the SEU environment in the upper atmosphere," IEEE Trans. on Nuc. Sci., vol. 36, no. 6, pp. 2275-2280, December 1989.

[61] A. Sims, C. Dyer, C. Peerless, K. Johansson, H. Pettersson, and J. Farren, "'The single event upset environment for avionics at high latitude," IEEE Trans. on Nuc. Sci., vol. 41, no. 6, pp. 2361-2367, December 1994.

[62] A. Taber and E. Normand, "Single event upset in avionics," IEEE Trans. on Nucl. Sci., vol. 40, pp. 120, April 1993.

[63] J. F. Ziegler, "Terrestrial cosmic rays," IBM Journal of Research and Development, vol. 40, no. 1, pp. 19-39, January 1996.

[64] C. S. Dyer and F. Lei, "Monte-Carlo calculations of the influence on aircraft radiation environments of structures and solar particle events," IEEE Trans. on Nucl. Sci.,vol. 48, no. 6, pp. 1987-1995, Dec. 2001.

[65] D. Heynderickx, "Comparison Between Methods to Compensate for the Secular Motion of the South Atlantic Anomaly", Radiation Measurements, vol. 26, pp. 369-373, 1996.

[66] G. D. Badhwar, "Drift rate of the South Atlantic Anomaly", J. Geophys. Res., vol. 102, pp. 2342-2349, 1997.

[67] E. J. Daly, J. Lemaire, D. Heynderickx, and D. J. Rodgers, "Problems with models of the radiation belts," IEEE Trans. on Nucl. Sci., vol. 43, no. 2, pp. 403-415, April 1996.

[68] G. P. Ginet, D. Madden, B. K. Dichter and D. H. Brautigam, "Energetic Proton Maps for the South Atlantic Anomaly," Nuclear and Space Radiation Effects Conference 2007 Radiation Effects Data Workshop, 2007.

[69] A. Van Helden, "The Galileo Project," 1995, http://galileo.rice.edu/sci/observations/sunspots.html.

[70] Schwabe, S.H. 1843, Astronomische Nachrichten, 20, no. 495, 234-235.

[71] E. G. Stassinopoulos, G. J. Brucker, D. W. Nakamura, C. A. Stauffer, G. B. Gee, and J. L Barth, "Solar Flare Proton Evaluation at Geostationary Orbits for Engineering Applications," IEEE Trans. on Nucl. Science, Vol. 43, No. 2, pp. 369-382, April 1996.

[72] J. Feynman, T. P. Armstrong. L. Dao-Gibner, and S. Silverman, "New Interplanetary Proton Fluence Model," J. Spacecraft, Vol. 27, No. 24, pp 403-410, July-August 1990.

[73] E. Sabine, "On Periodical Laws Discoverable in the Mean Effects of the Larger Magnetic Disturbances," No. 2, Phils. Trans. R. Soc. London, 142, 103, 1852.

[74] R. C. Carrington, "Description of a Singular Appearance Seen on the Sun on September 1, 1859," Mon. Not. R. Astron. Soc. 20, 13, 1860.

[75] C.R.Clauser and G. Siscoe, editors, "The Great Historical Geomagnetic Storm of 1859: A Modern Look," Advances in Space Research, Volume 38, Issue 2, 2006, Pages 117-118.

[76] E. J. Lerner, "Space Weather," Discover - The World of Science, pp. 45-61, August 1995.

[77] W. Li, J. Raeder, M. Øieroset, and T. D. Phan, "Cold dense magnetopause boundary layer under northward IMF: Results from THEMIS and MHD simulations," JOURNAL OF GEOPHYSICAL RESEARCH, VOL. 114, A00C15, doi:10.1029/2008JA013497, 2009.

[78] J. C. Ritter, 1996 IEEE NSREC Short Course, Indian Wells, CA.

[79] J. H. Allen, (17 April 1997), NOAA/National Geophysics Data Center, [WWW document], URL http://julius.ngdc.noaa.gov/stp/GEOMAG/apstar.html

[80] D. L. Chenette, J. Chen, E. Clayton, T. G. Guzik, J. P. Wefel, M. Garcia-Muñoz, C. Lapote, K. R. Pyle, K. P. Ray, E. G. Mullen, and D. A. Hardy, "The CRRES/SPACERAD Heavy Ion Model of the Environment (CHIME) for Cosmic Ray and Solar Particle Effects on Electronic and Biological Systems in Space," IEEE Trans. on Nucl. Science, Vol. 41, No. 6, pp. 2332-2339 December 1994.

[81] C. S. Dyer, A. J. Sims, J. Farren, J. Stephen, "Measurements of Solar Flare Enhancements to the Single Upset Environment in the Upper Atmosphere," IEEE Trans. on Nucl. Science, Vol. 37, No. 6, pp. 1929-1937, December 1990.

[82] J. I. Vette, "The space radiation environment," *IEEE Trans. on Nucl. Sci.*, vol. 12, no. 5, pp. 1-17, October 1965.

[83] H. H. Malitson and W. R. Webber, "A summary of solar cosmic ray events," Solar Proton Manual, NASA TRR-169.

[84] J. W. Haffner, "Natural nuclear radiation environments for the Grand Tour missions," *IEEE Trans. on Nucl. Sci.*, vol. 18, no. 6, pp. 443-453, December 1971.

[85] J. H. Adams, Jr., R. Silberberg, and C. H. Tsao, "Cosmic ray effects of microelectronics, Part I: The near-earth particle environment," NRL Memorandum Report 4506, August 25, 1981.

[86] J. H. Adams, Jr., J. R. Letaw, and D. F. Smart, "Cosmic ray effects of microelectronics, Part II: Geomagnetic cutoff effects," NRL Memorandum Report 5099, May 26, 1983.

[87] J. H. Adams, Jr., "The natural radiation environment inside spacecraft," *IEEE Trans. on Nucl. Sci.*, Vol. 29, No. 6, pp. 2095-2100, December 1982.

[88] E. L. Peterson, P. Shapiro, J. H. Adams, Jr., and E. A. Burke, "Calculation of cosmic-Ray Induce Soft Upsets and Scaling in VLSI Devices," IEEE Trans. on Nucl. Sci., Vol. 29, No. 6, pp. 2055-2063, December 1982.

[89] W. Heinrich, *Radiation Effects*, vol. 34, no. 143, 1977.

[90] E. L. Peterson, Approaches to proton single-event rate calculations," *IEEE Trans on Nucl. Sci.*, vol. 43, no. 2, pp. 496-504, April 1996.

[91] J. C. Pickel and J. T. Blanford Jr., "Cosmic ray induced errors in MOS memory cells," *IEEE Trans. on Nucl. Sci.*, vol. 25, no. 6, pp. 1166, December 1978.

[92] J. H. Adams, Jr., "Cosmic ray effects on microelectronics, Part IV," NRL Memorandum Report 5901, Naval Research Laboratory, Washington, DC, December 31, 1986.

[93] E. L. Petersen, J. C. Pickel, J. H. Adams, Jr., and E. C. Smith, "Rate Prediction for Single Event Effects - A Critique," IEEE Trans. on Nucl. Science, Vol. 39, No. 6, pp. 1577-1599, December 1992.

[94] D. L. Chenette, J. Chen, E. Clayton, T. G. Guzik, J. P. Wefel, M. Garcia-Muñoz, C. Lapote, K. R. Pyle, K. P. Ray, E. G. Mullen, and D. A. Hardy, "The CRRES/SPACERAD Heavy Ion Model of the Environment (CHIME) for Cosmic Ray and Solar Particle Effects on Electronic and Biological Systems in Space," IEEE Trans. on Nucl. Science, Vol. 41, No. 6, pp. 2332-2339 December 1994.

[95] G. D. Badhwar and P. M. O'Neill, "An Improved Model of the Galactic Cosmic Radiation for Space Exploration Missions," Nucl. Tracks Radiation Meas., 20, No. 3, pp. 402-410, 1992.

[96] P. P. Majewski, E. Normand, and D. L. Oberg, "A New Solar Flare Heavy Ion Model and Its Implementation Through MACREE, An Improved Modeling Tool to Calculate Single Event Effects Rates in Space," IEEE Trans. on Nucl. Science, Vol. 42, No. 6, pp. 2043-2050, December 1995.

[97] D. V. Reames, H. V. Cane, and T. T. von Rosenvinge, "Energetic particle abundances on solar electron events," *The Astrophys. J.*, vol. 357, pp. 259-270, July 1, 1990.

[98] C.S. Dyer, A.J. Sims, J.S. Farren, J. Stephen, C. Underwood, "Comparative measurements of single event upset and total dose environments using the CREAM instruments'" Nuclear Science, IEEE Transactions on Nuclear Science, Volume: 39 , Issue: 3 , Part 1-2, p: 413 – 417, June 1992.

[99] A. J. Tylka, F. Dietrich, and P. R. Boberg, "CREME96: A revision of the cosmic ray effects on microelectronics code," *IEEE Trans. on Nucl. Sci.*, vol. 44, no. 6, pp. 2150-2160, December 1997.

[100] R. A. Nymmik, M. I. Panusyk, T. I. Pervark, A. A. Suslov, "A Model of Galactic Cosmic Rays," Nucl. Tracks Radiation Meas., Vol. 20, No. 3, pp. 427-429, 1992.

[101] R.A. Nymmik, M.I. Panasyuk and A.A. Suslov, Galactic Cosmic Ray Flux Simulation and Prediction, Adv. Space Res. 17 (2) (1995), p. 19.

[102] P.M. O'Neill, "Badhwar–O'Neill galactic cosmic ray model update based on advanced composition explorer (ACE) energy spectra from 1997 to present," Advances in Space Research, Volume 37, Issue 9, 2006, Pages 1727-1733

[103] A. J. Davis, R. A. Mewaldt, C. M. S. Cohen, A. C. Cummings J. S. George, R. A. Leske , E. C. Stone, M. E. Wiedenbeck, N. E. Yanasak , E. R. Christian, T. T. vonRosenvinge, W, . R Binns, and P. L. Hink, "Solar minimum spectra of galactic cosmic rays and their implications for models of the near-earth radiation environment," JOURNAL OF GEOPHYSICAL RESEARCH, VOL. 106, NO. A12, PAGES 29,979-29,987, DECEMBER 1, 2001.

[104] C. S. Dyer, K. Hunter, S. Clucas, D. Rodgers, A. Campbell, and S. Buchner, "Observation of solar particle events from CREDO and MPTB during the current solar maximum," IEEE Trans. Nucl. Sci., vol. 49, no. 6, pp. 771–2775, Dec. 2002.

[71] D. C. Jensen and J. C. Cain, "An interim geomagnetic field

[105] M. A. Xapsos, C. Stauffer, T. Jordan, J. L. Barth, and R. A. Mewaldt, "Model for Cumulative Solar Heavy Ion Energy and Linear Energy Transfer Spectra," IEEE Transactions On Nuclear Science, VOL. 54, NO. 6, DECEMBER 2007.

[106] J. B. Weddel and J. W. Haffner, "Statistical evaluation of proton radiation from solar flares", Report SID 66-421, North American Aviation, July 1966.

[107] J. H. King, "Solar proton fluences for 1977-1983 space missions," *J. Spacecraft and Rockets*, vol. 11, no. 6, pp. 401-408, June 1974.

[108] J. Feynman, G. Spitale, J. Wang, and S. Gabriel, "Interplanetary fluence model: JPL 1991," *J. Geophys. Res.*, vol. 98, pp 13281-13294, 1993.

[109] M. A. Xapsos, J. L. Barth, E. G. Stassinopoulos, G. P. Summers, E. A. Burke, G. B. Gee, "Model for prediction of solar proton events," Proceedings from the Space Radiation Environment Workshop, Farnborough, UK, 1-3 November 1999.

[110] M. A. Xapsos, G. P. Summers, P. Shapiro, and E. A. Burke, "New techniques for prediction solar proton fluences for radiation effects applications," *IEEE Trans. on Nucl. Sci.*, vol. 43, no. 6, December 1996.

[111] R. A. Nymmik, "Probabilistic model for fluences and peak fluxes of solar energetic particles," Radiation Meas., vol. 30, pp. 287–296, 1999.

[112] M. A. Xapsos, C. Stauffer, G. B. Gee, J. L. Barth, E. G. Stassinopoulos, and R. E. McGuire, "Model for solar proton risk assessment," IEEE Trans. Nucl. Sci., vol. 51, no. 6, pp. 3394–3398, Dec. 2004.

[113] M. A. Xapsos, G. P. Summers, and E. A. Burke, "Probability model for peak fluxes of solar proton events," *IEEE Trans. on Nucl. Sci.*, vol. 45, no. 6, pp. 2948-2953, December 1998.

[114] M. A. Xapsos, G. P. Summers, J. L. Barth, E. G. Stassinopoulos, and E. A. Burke, "Probability model for worst case solar proton event fluences," *IEEE Trans. on Nucl, Sci.*, vol. 45, no. 6, pp. 1481-1485, December 1999.

[115] M. A. Xapsos, J. L. Barth, E. G. Stassinopoulos, E. A. Burke, and G. B. Gee, "Model for emission of solar protons (ESP) – cumulative and worst case event fluences," NASA-Marshall Space Flight Center SEE Program, http://see.msfc.nasa.gov.

[116] M. A. Xapsos, J. L. Barth, E. G. Stassinopoulos, G. P. Summers, E. A. Burke, G. B. Gee, "Model for prediction of solar proton events," Proceedings from the Space Radiation Environment Workshop, Farnborough, UK, 1-3 November 1999.

[117] J. I. Vette, "The space radiation environment," *IEEE Trans. on Nucl. Sci.*, vol. 12, no. 5, pp. 1-17, October 1965.

[118] C. E. McIlwain "The Radiation Belts, Natural and Artificial," Science 142 (1963), p. 355.

[119] E. G. Mullen, M. S. Gussenhoven, K. Ray, and M. Violet, "A double-peaked inner radiation belt: cause and effect as seen on CRRES," *IEEE Trans. on Nucl. Sci.*, vol. 38, no. 6, pp. 1713-1717, December 1991.

[120] M. S. Gussenhoven, E. G. Mullen, and D. H. Brautigam, "Improved understanding of the earth's radiation belts from the CRRES satellite," IEEE Trans. on Nucl. Sci., vol. 43, no. 2, pp. 353-368, April 1996.

[121] M. S. Gussenhoven, E. G. Mullen, M. D. Violet, C. Hein, J. Bass, and D. Madden, "CRRES high energy proton flux maps," *IEEE Trans. on Nucl. Sci.*, vol. 40, no. 6, pp. 1450-1457, December 1993

[122] D. H. Brautigam, M. S. Gussenhoven, E. G. Mullen, "Quasi-static model of outer zone electrons," *IEEE Trans. on Nucl. Sci.*, vol. 39, no. 6, pp. 1797-1803, December 1992.

[123] M. S. Gussenhoven, E. G. Mullen, M. Sperry, K. J. Kerns, "The effect of the March 1991 storm on accumulated dose for selected orbits: CRRES dose models," *IEEE Trans. on Nucl. Sci.*, vol. 39, no. 6, pp 1765-1772, December 1992.

[124] M. S. Gussenhoven, E. G. Mullen, J. T. Bell, D. Madden, and E. Holeman, "APEXRAD: low altitude orbit dose as a function of inclination, magnetic activity and solar cycle," *IEEE Trans. on Nucl. Sci.*, vol. 44, no. 6, pp. 2161-2168, December 1997.

[125] K. A. Pfitzer, "Radiation dose to man and hardware as a function of atmospheric density in the 28.5 degree Space Station orbit," MDSSC Rep. H5387, McDonnell Douglas Space Systems Co., Huntington Beach, CA, 1990.

[126] D. Heynderickx, (17 April 1997), Belgisch Instituut voor Ruimte-Aëronmie/Institut d'Aéronomie Spatiale de Belgique (BIRA/IASB), Proceedings from Model Workshop, "Low altitude trapped radiation model using TIROS/NOAA data" by S. L. Huston, G. A. Kuck, and K. A. Pfitzer, WWW document, URL http://magnet.oma.be/trend/trend2.html

[127] S. L. Huston and K. A. Pfitzer, "A new model for the low altitude trapped proton environment," *IEEE Trans. on Nucl. Sci.*, vol. 45, no. 6, pp. 2972-2978, December 1998.

[128] M. A. Xapsos, S. L. Huston, J. L. Barth, and E. G. Stassinipoulos, "Probabilistic model for low-altitude trapped proton fluxes," *IEEE Trans. on Nucl. Sci.*, vol. 49, no. 6, pp. 2776-2781, December 2002.

[129] D. Heynderickx and J. Lemaire, "Coordinate systems for mapping low-altitude trapped particle fluxes," Proc. Taos Workshop on Earth's Trapped Particle Environments, Aug. 14-19, 1994.

[130] D. Heynderickx, M. Kruglanski, V. Pierrard, J. Lemaire, M. D. Looper, and J. B. Blake, "A low altitude trapped proton model for solar minimum conditions based on SAMPEX/PET data," *IEEE Trans. on Nucl. Sci.*, vol. 46, no. 6, pp. 1475-1480, December 1999.

[131] D. M. Boscher, S. A. Bourdarie, R. H. W. Friedel, and R. D. Belian, "Model for the Geostationary Electron Environment: POLE," *IEEE Trans. on Nucl. Sci,* vol. 50, no. 6, pp. 2278-2283, December 2003.

[132] Sicard-Piet, A., S. Bourdarie, D. Boscher, and R. H. W. Friedel (2006), A model for the geostationary electron environment: POLE, from 30 keV to 5.2 MeV, IEEE Trans. Nucl. Sci., 53(4), 1844– 1850, doi:10.1109/ TNS.2006.

[133] Sicard-Piet, A., S. Bourdarie, D. Boscher, R. H. W. Friedel, M. Thomsen, T. Goka, H. Matsumoto, and H. Koshiishi (2008), A new international geostationary electron model: IGE-2006, from 1 keV to 5.2 MeV, Space Weather, 6, S07003, doi:10.1029/2007.

[134] G.L. Wrenn, D.J. Rodgers, P. Buehler, " Modeling the Outer Belt Enhancements of Penetrating Electrons," Journal of Spacecraft and Rockets, vol. 37, issue 3, pp. 408-415, 2000.

[135] D.J. Rodgers, K.A. Ryden, G.L. Wrenn, P.M .Latham, J. Söringnsen, L. Levy," An Engineering Tool for the Prediction of Internal Dielectric Charging, 6th Spacecraft Charging Technology Conference", Hanscom, 1998.

[136] J-M Lauenstein, J. L. Barth, D. G. Sibeck, "Introduction to special section on International Working Group Meeting on New Standard Radiation Belt and Space Plasma Models for Spacecraft Engineering," SPACE WEATHER, VOL. 3, S07B01, doi:10.1029/2005SW000159, 2005.

[137] International Working Group Meeting on New Standard Radiation Belt and Space Plasma Models for Spacecraft Engineering, SPACE WEATHER, VOL. 3, S11B05, doi:10.1029/2005SW000150, 2005.

[138] G. P. Ginet, T. P. O'Brien, "AE-9/AP-9 Trapped Radiation and Plasma Models - Requirements Specification." http://lws-set.gsfc.nasa.gov/Documents/AE9-AP9_Requirements_v3.pdf.

[139] D. Boscher, S. Bourdaire, and T. Beutier, "Dynamic modeling of trapped particles," *IEEE Trans. on Nucl. Sci.*, vol. 43, no. 2, pp. 416-425, April 1996.

[140] S. Bourdarie, D. Boscher, and T. Beutier, "Modeling the charged particle transport in the Earth's internal magnetosphere," in Workshop of the GdR Plasmae, Tournon, France, Apr. 10-12, 1995.

[141] Private Communication with S. Bourdarie, ONERA, Toulouse, France, September 2002.

[142] J. W. Haffner, "Natural nuclear radiation environments for the Grand Tour missions," *IEEE Trans. on Nucl. Sci.*, vol. 18, no. 6, pp. 443-453, December 1971.

[143] P. G. Kase, "The radiation environments of outer-planet missions," *IEEE Trans. on Nucl. Sci.*, vol. 19, no. 6, pp. 141-146, December 1972.

[144] N. Divine, "The Planet Jupiter (1970)," NASA SP-8069, Jet Propulsion Laboratory, Pasadena, California, December 1971.

[145] From the History of NASA, SP-349/396 Pioneer Odyssey, http://history.nasa.gov/SP-349/ch5.htm.

[146] Private communication with T. Oldham on talk by G. Lee at the 1983 Single Event Effects Symspoium, QSS Group at Goddard Space Flight Center, Code 561, Greenbelt, MD 20771, January 2003.

[147] N. Divine and H. B. Garrett, "Charged particle distributions in Jupiter's magnetosphere," *J. of Geo. Phys. Res.*, vol. 88, no. A9, pp 6889-6903, September 1983.

[148] I. Jun, H.B. Garrett, and R.W. Evans, "High-Energy Trapped Particle Environments at Jupiter: An Update," IEEE Transactions On Nuclear Science, VOL. 52, NO. 6, pp. 2281-2285, December 2005.

[149] S. Bourdarie and A. Sicard, "Jupiter environmental modelling," ONERA technical note 120 issue 1.2, ESA contract 19735/NL/HB, FR 1/11189 DESP, October 2006.

[150] A. H. Taber and E. Normand, "Investigation and Characterization of SEU Effects and Hardening Strategies in Avionics," DNA-TR-94-123, Defense Nuclear Agency, Alexandria, VA, February 1995.

[151] R. B. Mendall and S. A. Korff, "Fast neutron flux in the atmosphere," *J. Geophys.*, vol. 68, 5487, 1963.

[152] T. W. Armstrong et al., "Calculation of neutron flux spectra induced in the earth's atmosphere by galactic cosmic rays," *J. Geophys. Res.*, vol. 78, 2715, 1973.

[153] M. Merker et al., "Time dependent world-wide distribution of atmospheric neutrons and their products," *J. Geophys. Res.*, vol. 78, 2727, 1973.

[154] J. W. Wilson, L. W. *Townsend*, W. Schimmerling, G. Khandelwal, F. Khan, J. E. Nealy, F. A. Cucinotta, L. C. Simsonsen, J. L. Shinn, J. W. Norbury, "Radiation Safety in the Earth's Atmosphere," in NASA RP-1257, Transport Methods and Interactions for Space Radiations, p. 519, December 1991.

[155] C. Tsao, R. Silberberg, J. Adams Jr., and J. Letaw, "Cosmic ray effects on microelectronics: Part III: Propagation of cosmic rays in the atmosphere," NRL Memorandum Report 5402, Aug 1984.

[156] C.S. Dyer, A. Sims, and C, Underwood, "Measurements of the SEE Environment from Sea Level to GEO Using the CREAM and CREDO Experiments," IEEE Transactions On Nuclear Science, VOL. 43, NO. 2, pp. 383-402, April 1996.

[157] C. S. Dyer and P. R. Truscott, "Cosmic radiation effects on avionics," ERA Technology Conference Volume for 1997 Avionics Conference, Heathrow UK, pp 6.3.1-6.3.10, November 1997.

[158] E. Normand, D. Olberg, J. Wert, J. Ness, P. Majewski, S. Wendron, and A. Gavron, "Single event upset and charge collection measurements using high energy protons and neutrons," *IEEE Trans. on Nul. Sci.*, vol. 41, no. 6, pp. 2203-2209, Dec 1994.

TABLE 7.6.1: ENHANCEMENT FACTORS FOR CREAM ON CONCORDE DURING SOLAR PARTICLE EVENTS

Channel Number & Charge Deposition Threshold	29 Sep 1406-1726	19 Oct 1420-1735	20 Oct 0859-1204	22 Oct 1814-2149	24 Oct 1805-2135
1 19 fC	3.7 ± 0.02	1.6 ± 0.01	1.4 ± 0.01	1.5 ± 0.01	3.4 ± 0.01
2 46 fC	4.9 ± 0.1	1.9 ± 0.04	1.6 ± 0.04	1.8 ± 0.04	4.5 ± 0.06
3 110 fC	5.7 ± 0.1	2.1 ± 0.07	1.8 ± 0.07	1.9 ± 0.07	5.2 ± 0.1
4 260 fC	5.9 ± 0.2	2.0 ± 0.1	1.8 ± 0.1	2.0 ± 0.1	5.7 ± 0.2
5 610 fC	5.6 ± 0.6	2.0 ± 0.3	2.0 ± 0.4	2.1 ± 0.3	4.9 ± 0.4
6 1.50 pC	6.1 ± 1.5	3.0 ± 0.7	1.1 ± 0.8	1.0 ± 0.6	4.3 ± 1.1
7 3.40 pC	(17.4 ± 17.4)	-	(30.4 ± 30.4)	-	-
8 8.10 pC	-	-	-	-	-
9 19.3 pC	-	-	-	-	-

Table 9.1.1: Spacecraft Effects and Mitigation

Effect	Mitigation
Total Ionizing Dose	Selection of hardened components, Shielding
Non-ionizing Dose	Selection of hardened components, Shielding, Plans for degradation, Close shutters
Surface Erosion	Selection of materials
Single Event Effects	Selection of components, Error correction, Watch-dog timers, Current limiters, Operational "workarounds"
Surface Charging	Grounding, Material selection, Operational "workarounds"
Deep-dielectric Charging	Shielding, Grounding, Material selection, Circuit protection
Impacts	Shields, Material selection, On-orbit maneuvers
Drag	Fuel consumption estimates, re-boosts, Relocation

Table 1.1: Radiation Effects in Space

Radiation Effect	Impact on Mission	Space Environment	Natural Variation in Environment
Surface Charging	Biasing of instrument readings, Power drains, Physical damage	0.01 - 100keV: Electrons	Minutes
Surface Dose	Changes in thermal, electrical, and optical properties	Ultraviolet, Atomic oxygen, Particle Radiation	Minutes
Deep-dielectric Charging	Electrical discharges causing physical damage	>100keV: Electrons	Hours
Total Ionizing Dose	Performance degradation, Loss of function, Loss of mission	>100keV: Trapped and solar protons, Trapped electrons	Hours
Non-Ionizing Dose	Degradation of optical components and solar cells	>10 MeV: Trapped and solar protons, Trapped electrons, Neutrons	Days
Single Event Effects	Data corruption, Noise on images, Interruption of service, Loss of spacecraft	>10 MeV/amu: Protons (Trapped & Solar) Heavy ions (Galactic Cosmic Rays & Solar) Neutrons	Days

Table 2: Maximum Energies of Particles

Particle Type	Maximum Energy
Trapped Electrons	10s of MeV
Trapped Protons & Heavy Ions	100s of MeV
Solar Protons	GeV
Solar Heavy Ions	GeV
Galactic Cosmic Rays	TeV
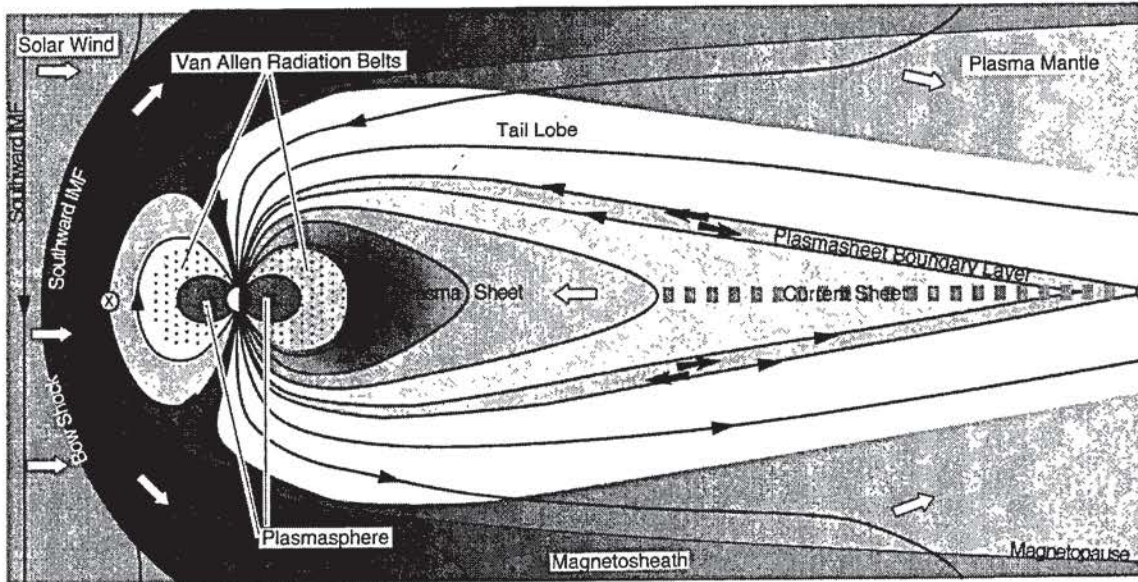
Fig. 2.3.1: The Earth's magnetosphere, diagram adapted from T. W. Hill by P.H. Reiff
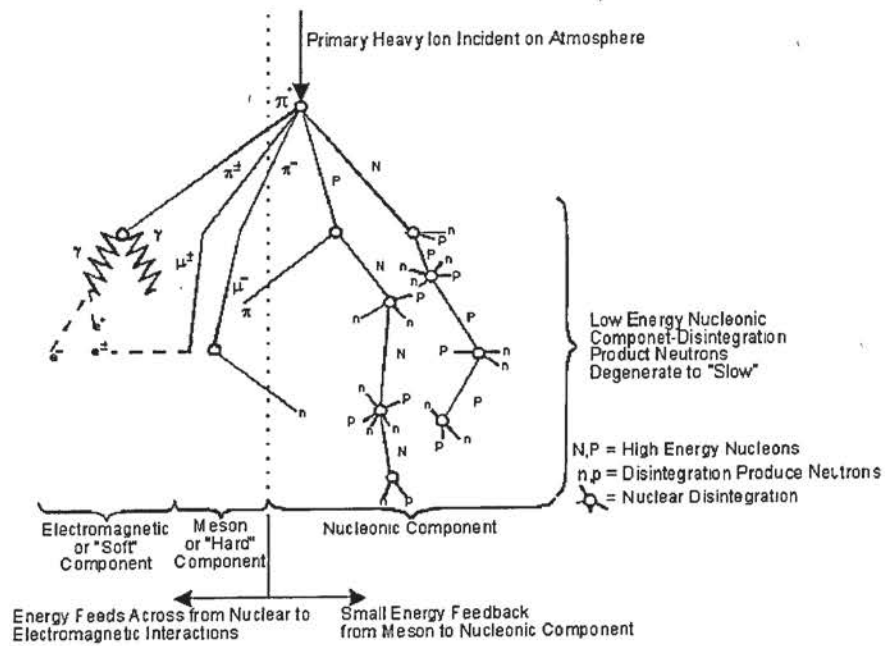
Fig. 2.4.1: Cosmic rays hit the top of the atmosphere and disintegrate into neutrons. *Smart and Shea*

Table 9.4.1: Summary of Models

Mission Phase	Characteristics of Models
Pre-launch "Climate" Models	Levels throughout the solar cycle, Spatial resolution, Worst-case environments Time distributions of changes in levels due to solar activity, Confidence levels, Broad energy range
Launch & Operations "Weather" Models	Forecasts specific to the region, Forecasts specific to particle population, Energy range information, Quiet-time forecasts
Anomaly Resolution "Climate" and "Weather" Models	Time specific, Location specific, Environment component relevant to the effect, Energy spectrum of environment component
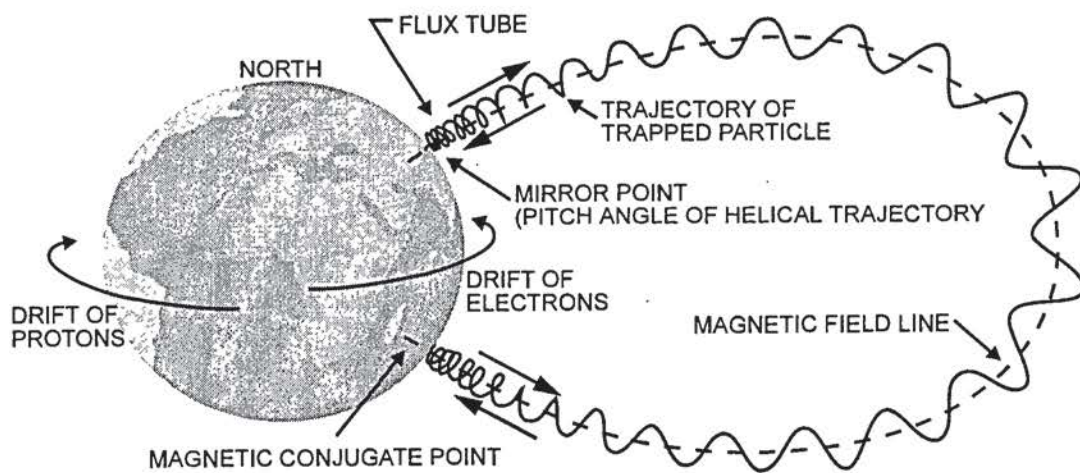
Fig. 3.2.1: The three motions of the trapped particles form drift shells. *after Hess*
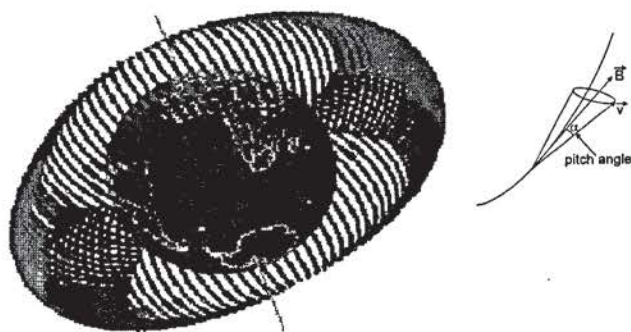
Fig. 3.2.2: Drift shell of a trapped particle. *Lemaire et al.*
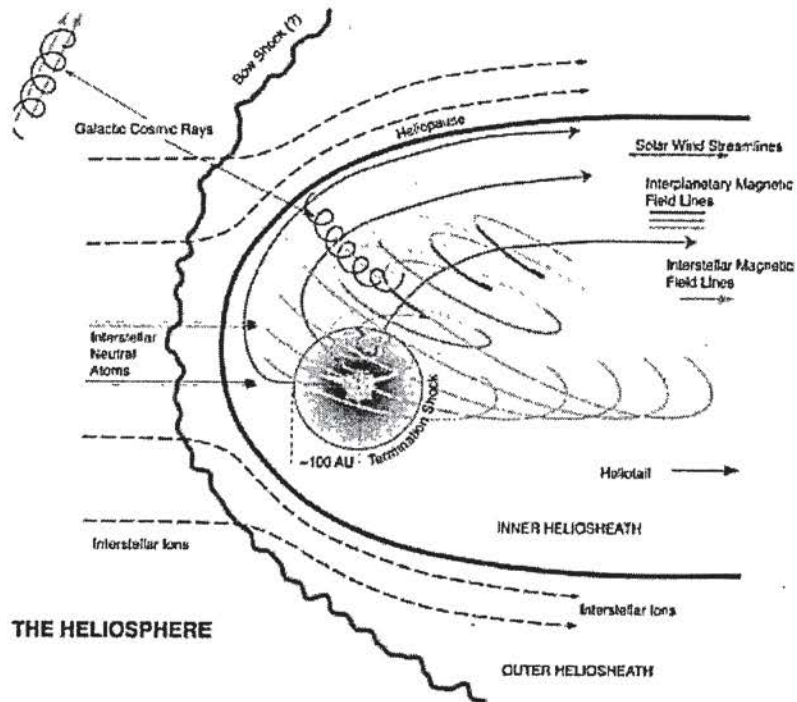
Fig 2.5.1: The global heliosphere is created by the supersonic solar wind diverting the interstellar plasma flow around the Sun. SOURCE: Jet Propulsion Laboratory, courtesy of Steven T. Suess.
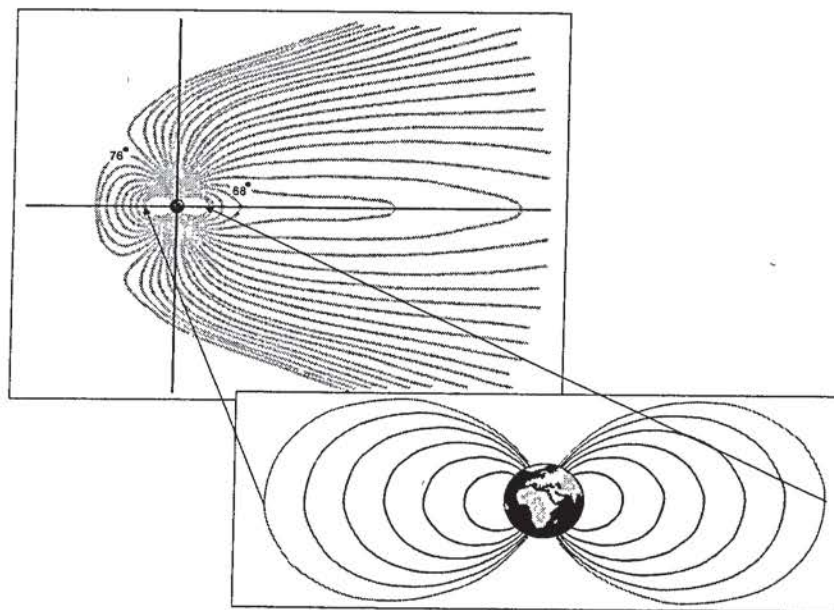
Fig. 3.1.1: Dipole field lines calculated with internal and external field models.

World Map of Geomagnetic Rigidity Contours at 800 km
After Shea & Smart, 1975 and Adams et al, 1981
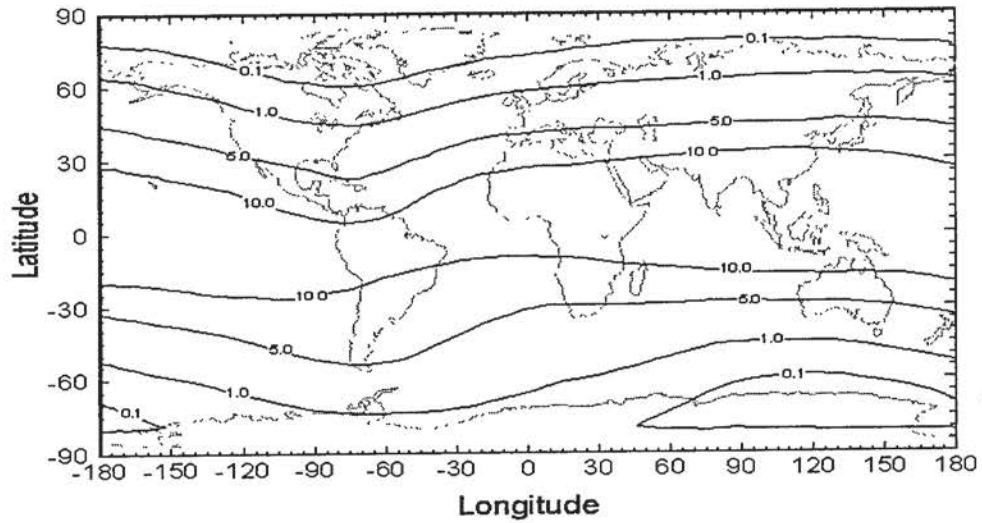
Fig. 3.3.2: Magnetic rigidity as calculated by Shea and Smart. Note that rigidity is lower at higher latitudes, allowing increased particle exposure near the poles.

Nuclear Composition of Galactic Cosmic Particles
Energy ~ 2 GeV/nuc, Normalized to Silicon = 10^6
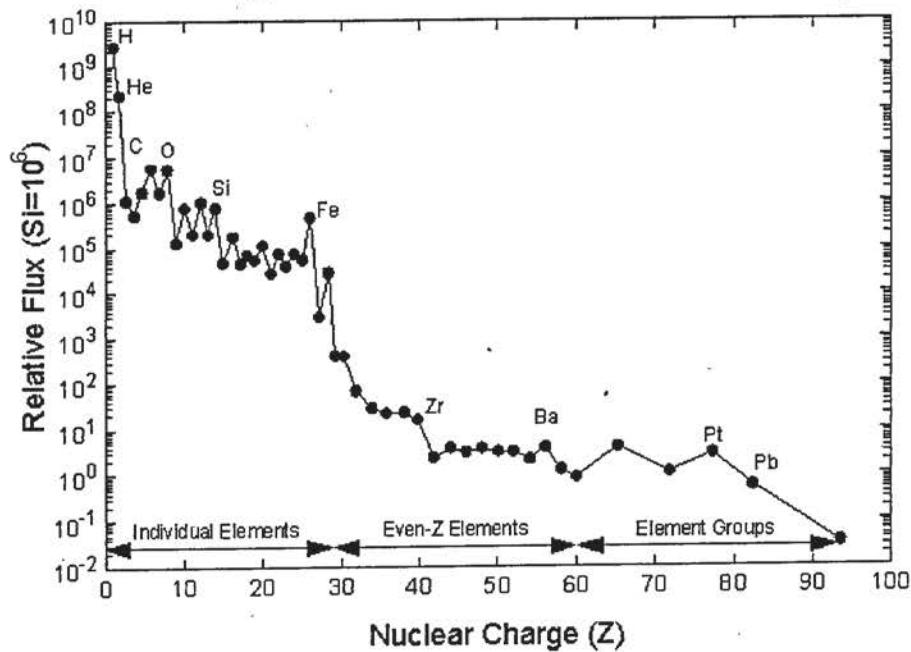
Fig. 4.1.4.1: Relative abundances of galactic cosmic ray ions in interplanetary space. *after Medwaldt*
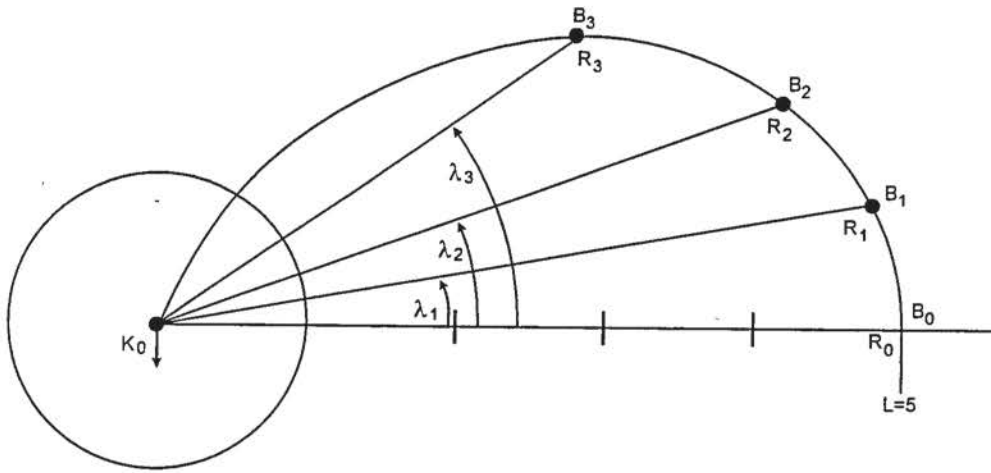
Fig. 3.2.3: The B-L magnetic coordinate system is used to map the location of charged particles. *after Stassinopoulos*
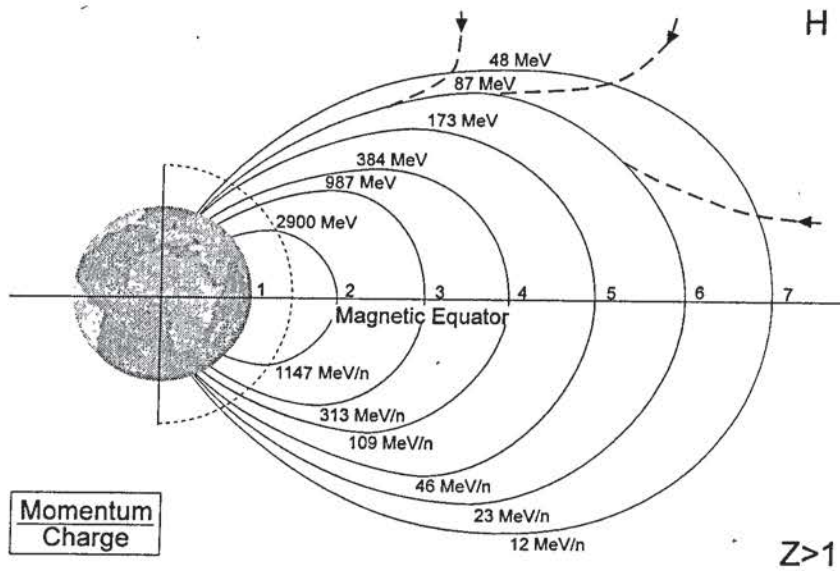
Fig. 3.3.1: The relationship between the dipole shell parameter, L, and cutoff rigidity is often used to determine the particle energy required to penetrate the magnetosphere. *after Stassinopoulos*
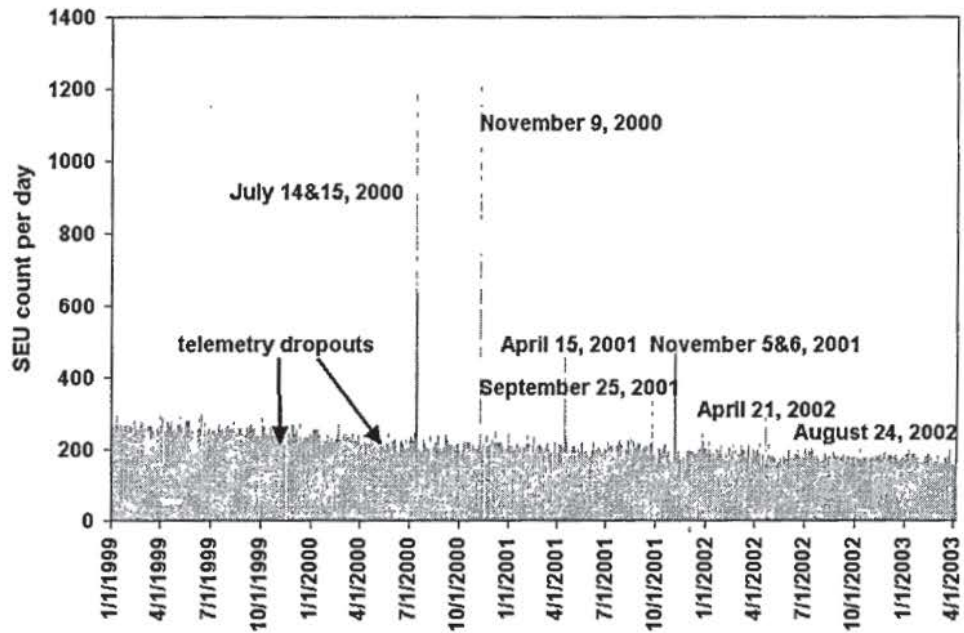
Fig. 4.2.2.1: Large increases in daily SEU rates are observed during solar particle events.
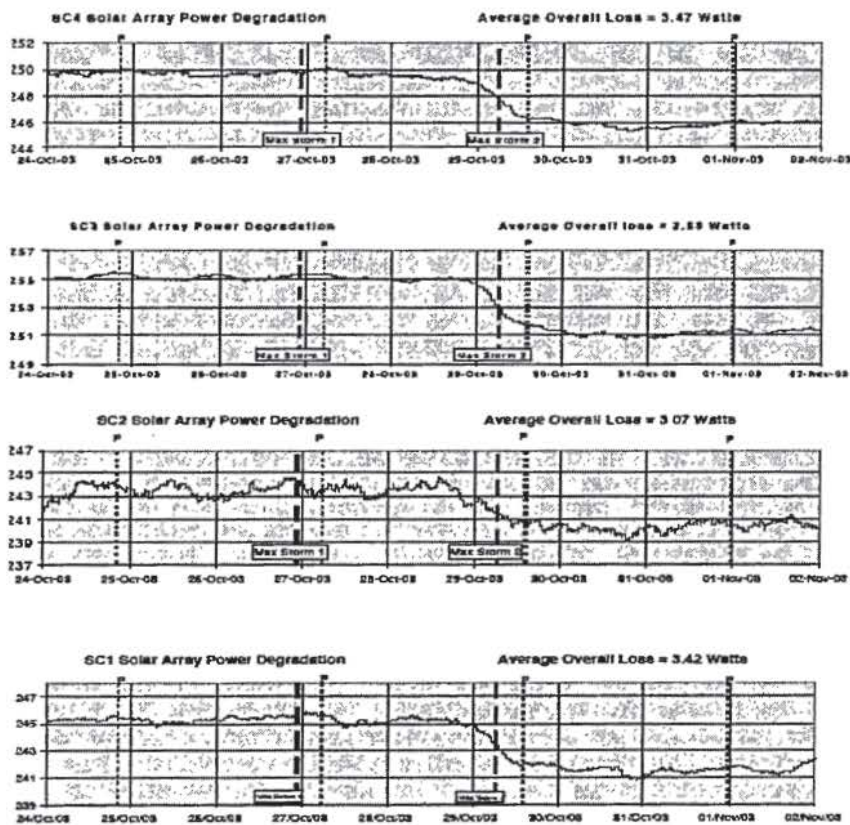
Fig 4.2.2.2: Increased rate of solar cell degradation because of increased levels of protons during the October 2003 solar storms.
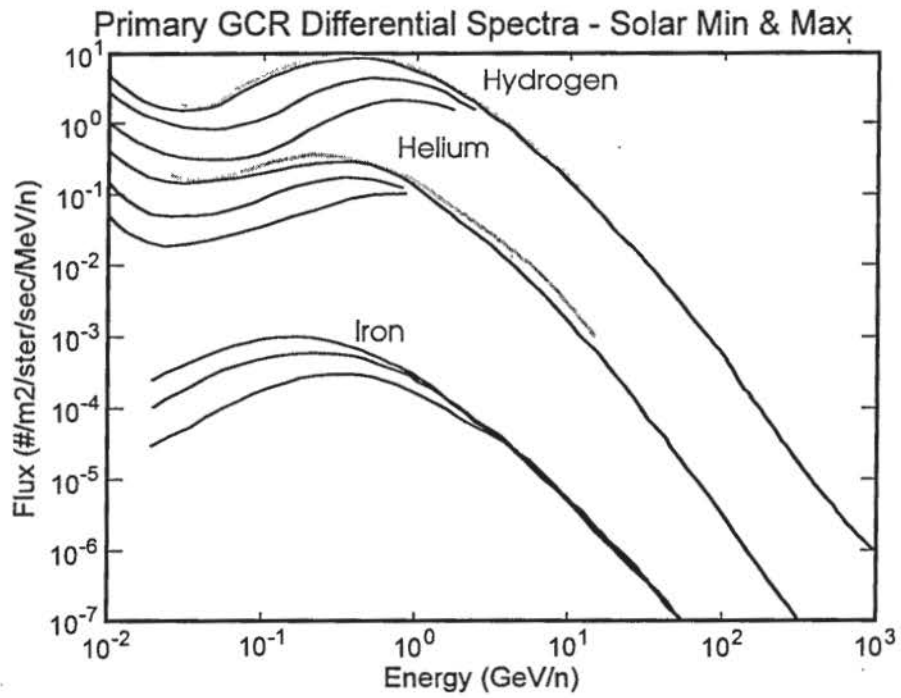
Fig. 4.1.4.2: Energy spectra of interplanetary galactic cosmic rays. Hydrogen values are multiplied by 5 to distinguish them from the helium spectra. *after Smart and Shea*
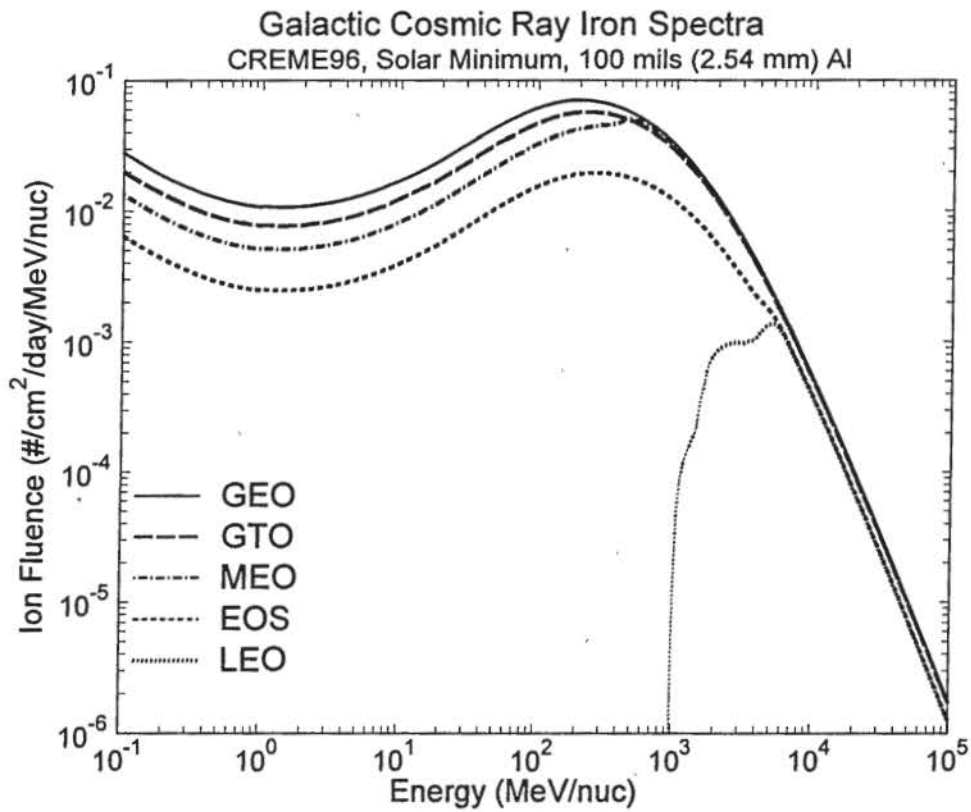
Fig. 4.1.4.3: Energy spectra for GCRs for various Earth orbits. Note the effect of the magnetosphere on attenuating heavy ions for low Earth orbits.

Electrons@GOES-6 (1 minute)
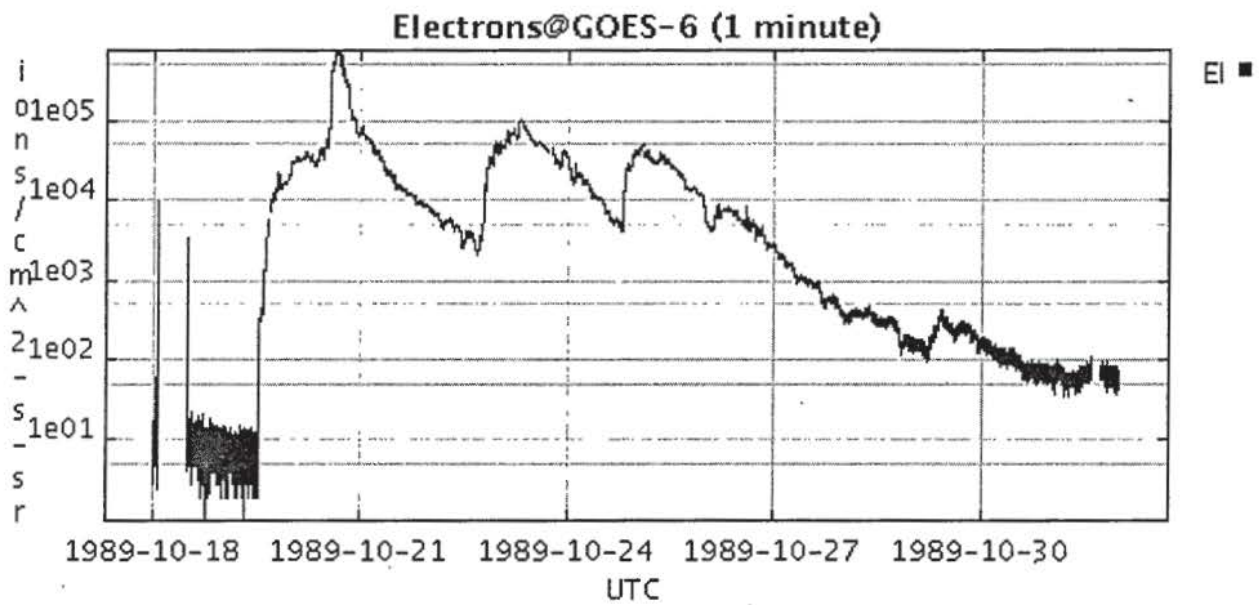
Fig.4.2.4.1: > 2 MeV electron levels at Geostationary during the October 1989 storms.

Alpha-particles@GOES-6 (1 minute)
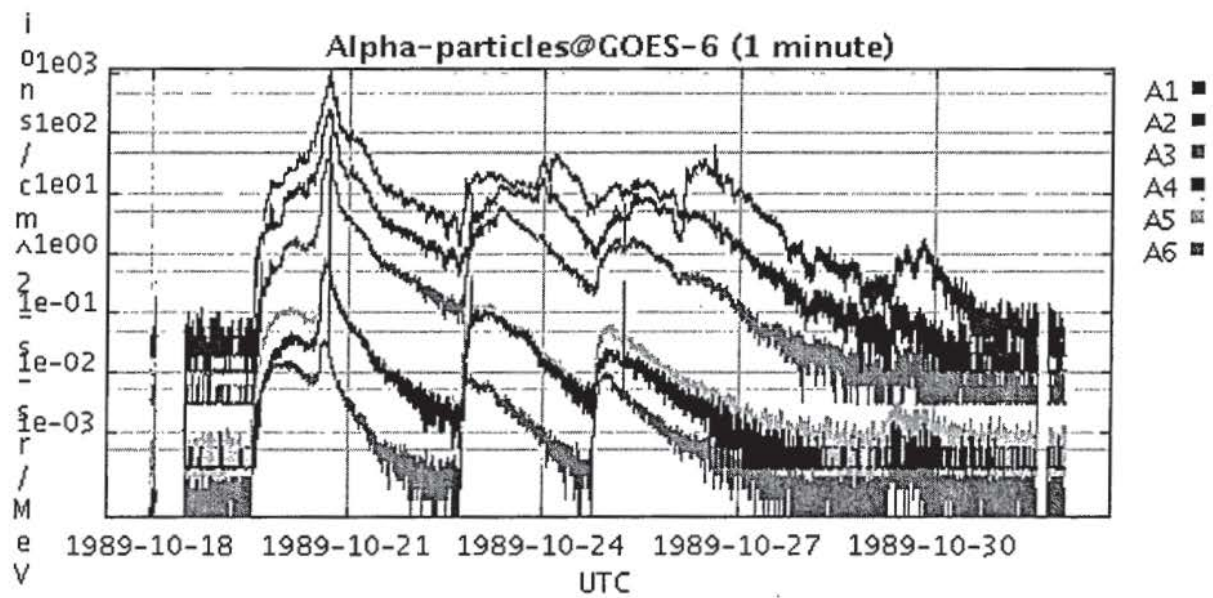
Fig. 4.2.4.2: > High energy alpha particle measurements (uncorrected) at geostationary during the October 1989 solar storms.
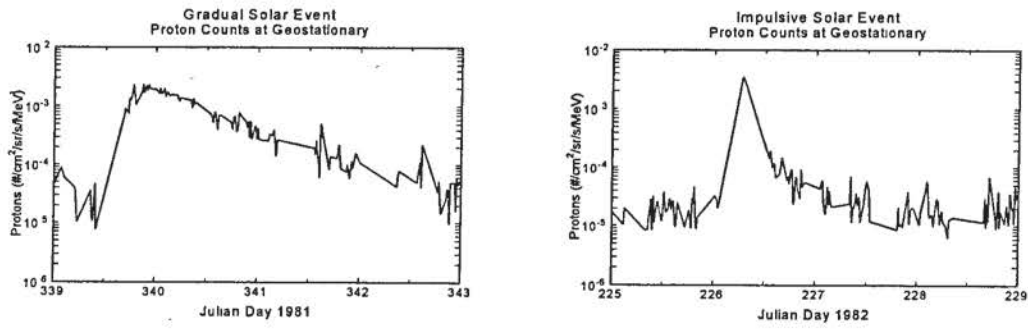
Fig. 4.2.3.1: The difference in the proton counts at geostationary is a fundamental characteristic of gradual and impulsive solar events. *after Reames*
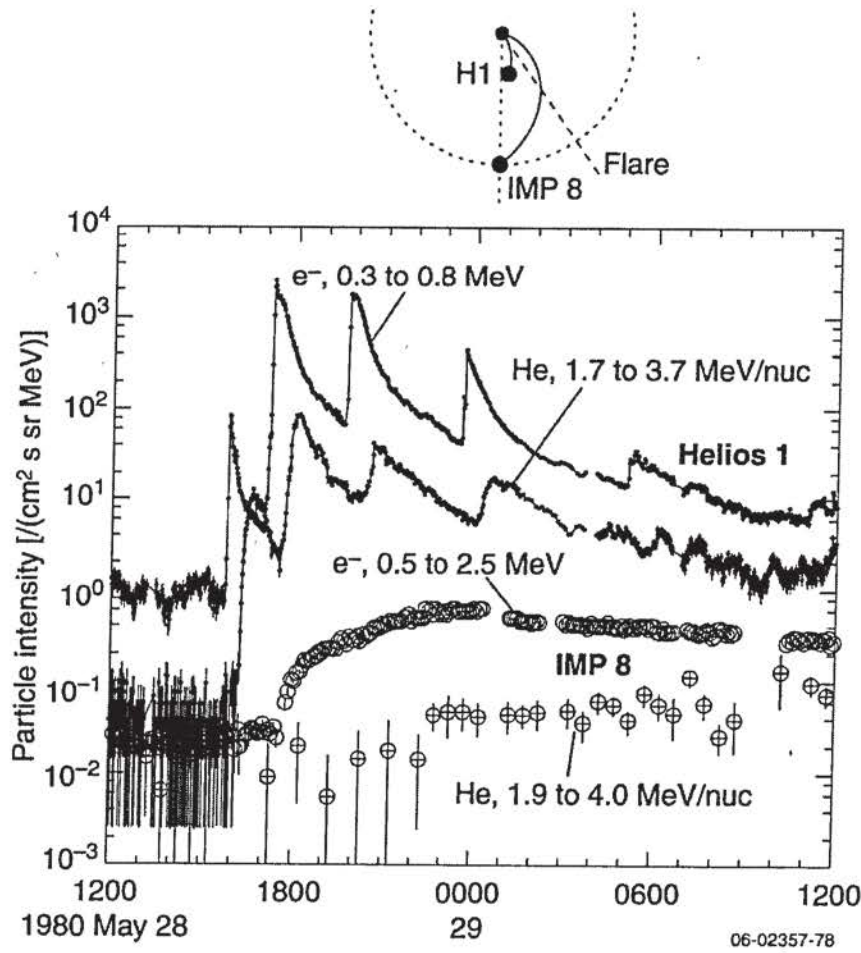
Fig. 4.2.3.2 Electron and alpha particle time profiles recorded by Helios-1 at 0.3 AU and by IMP-8 at 1.0 AU during a series of impulsive particle events on 28 May 1980. [*Wibberenz and Cane*].
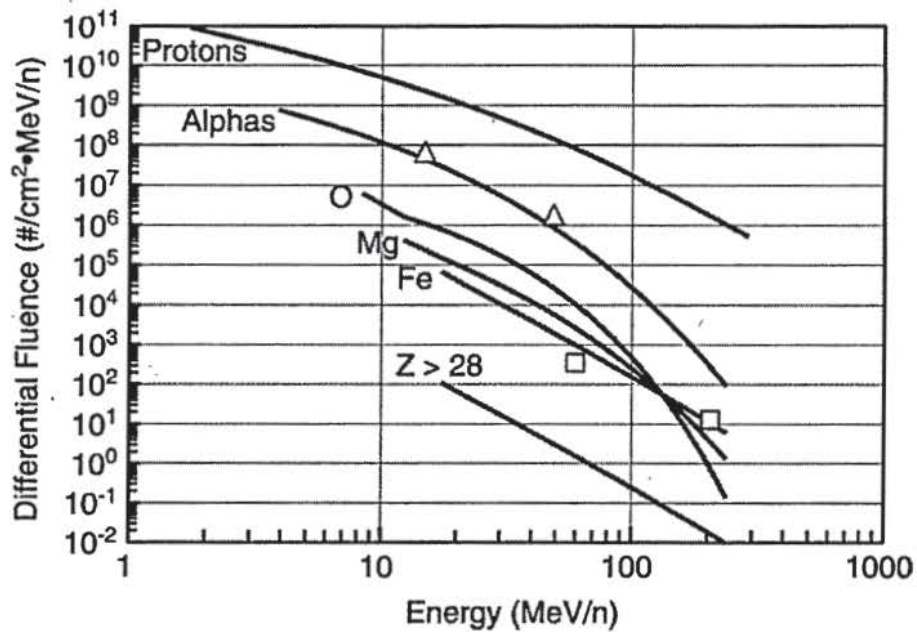
Fig. 4.2.4.5: Differential fluence-energy spectra for protons, alpha particles, oxygen, magnesium, iron and summed spectra for Z > 28 elements for a 2-year mission during solar maximum at the 90% confidence level as predicted by the PSYCHIC model. Triangles and squares are results for alpha particles and iron, respectively. *after Tylka et al.*
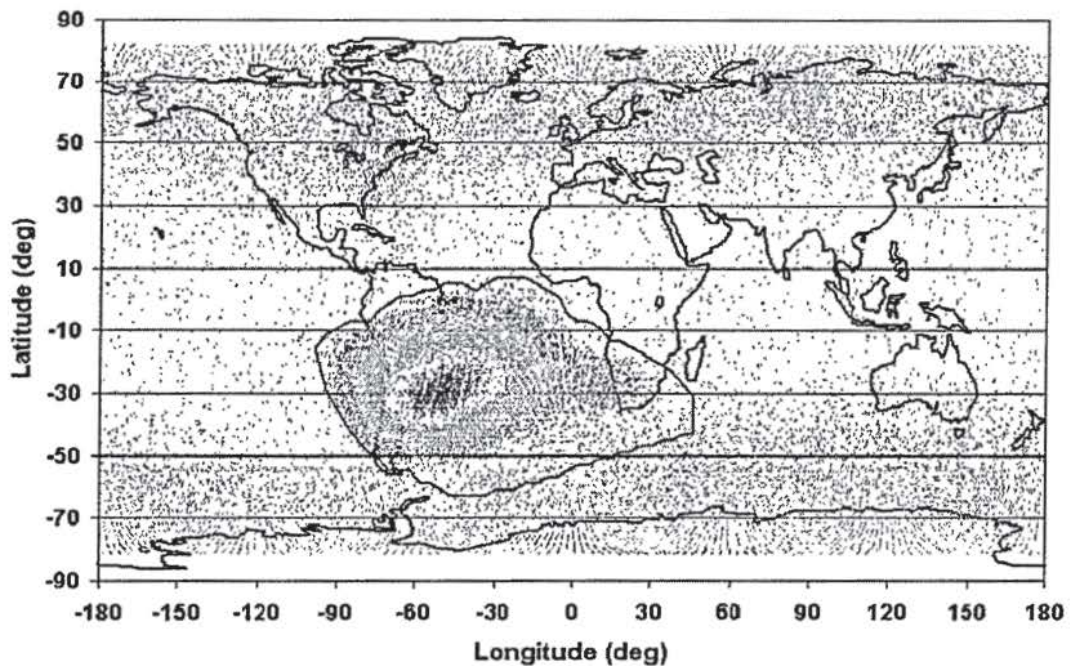
Fig. 5.2.1: Single event upsets on the Seastar spacecraft solid state recorder in the South Atlantic Anomaly. Upsets in the high latitude regions are from galactic cosmic ray heavy ions a particle from solar events.

Integral Solar Proton Spectra for Selected Cycle 22 Events
Compares October 1989 with August 1972
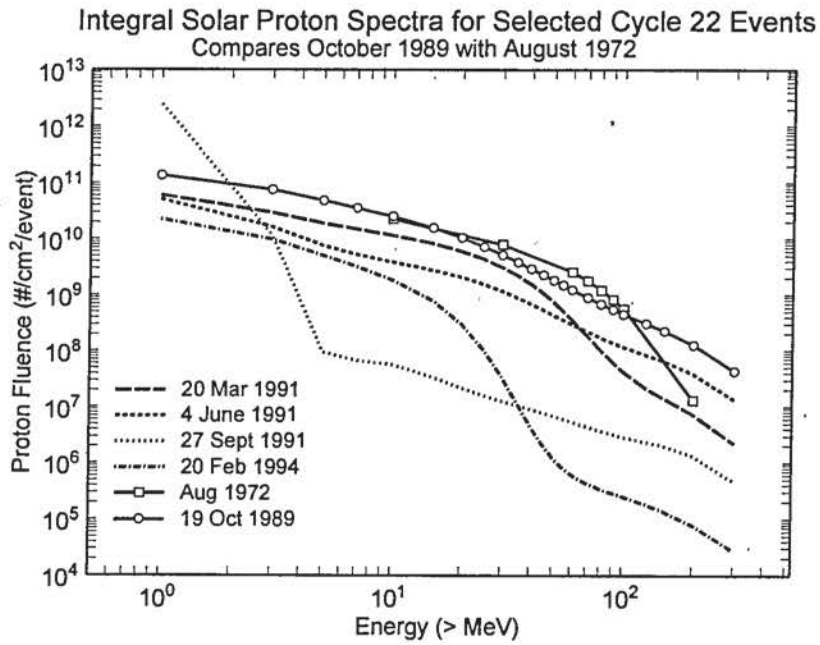
Fig. 4.2.4.3: Solar proton fluence spectra for some of the largest solar cycle 22 events compared to the August 1972 event. *Stassinopoulos et al.*

Differential Solar Proton Fluxes
Average Over Worst Day of Solar Cycle, 100 mils Shielding
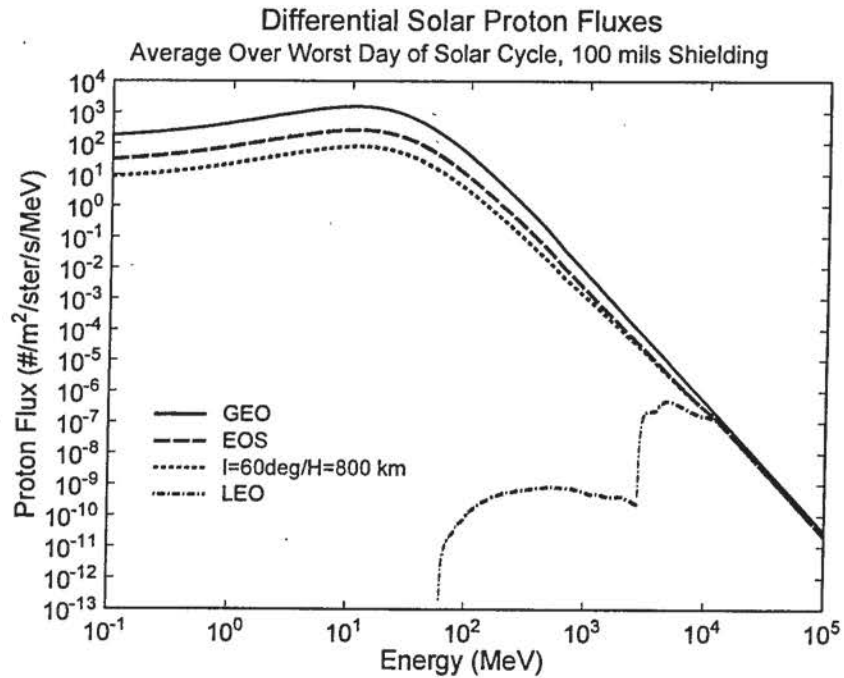
Fig. 4.2.4.4: Energy spectra for solar protons for various Earth orbits. Note the effect of the magnetosphere on attenuating protons for low Earth orbits.

Omnidirectional Integral Proton Fluxes at Magnetic Equator
AP-8 for Solar Maximum
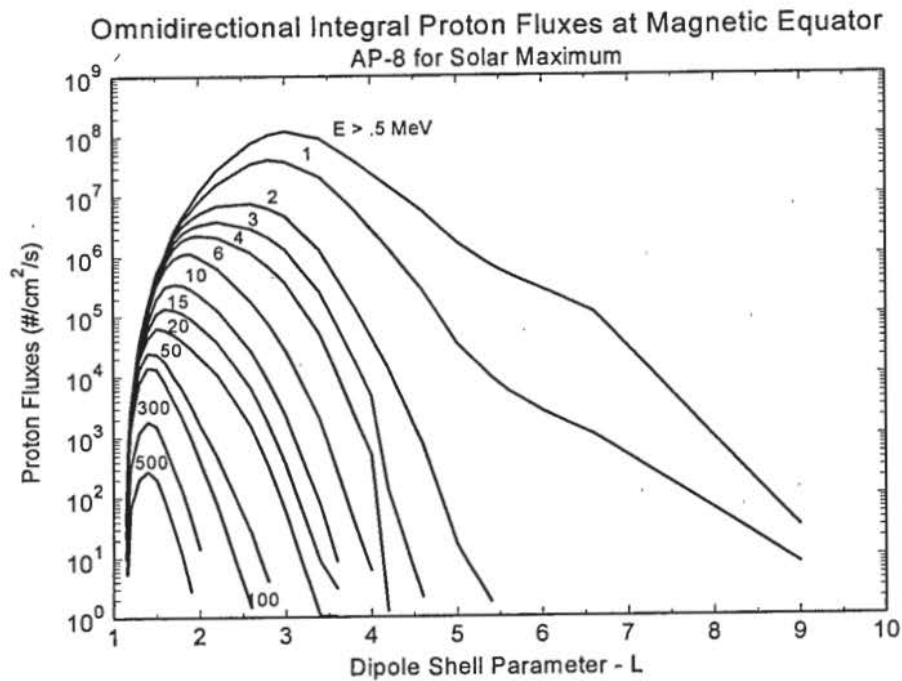
Fig. 5.4.3: Variation of proton flux levels with radial distance from the Earth.

Integral Proton Flux Contours for E > 30 MeV (#/cm²/s)
Altitude = 1000 km, Solar Maximum
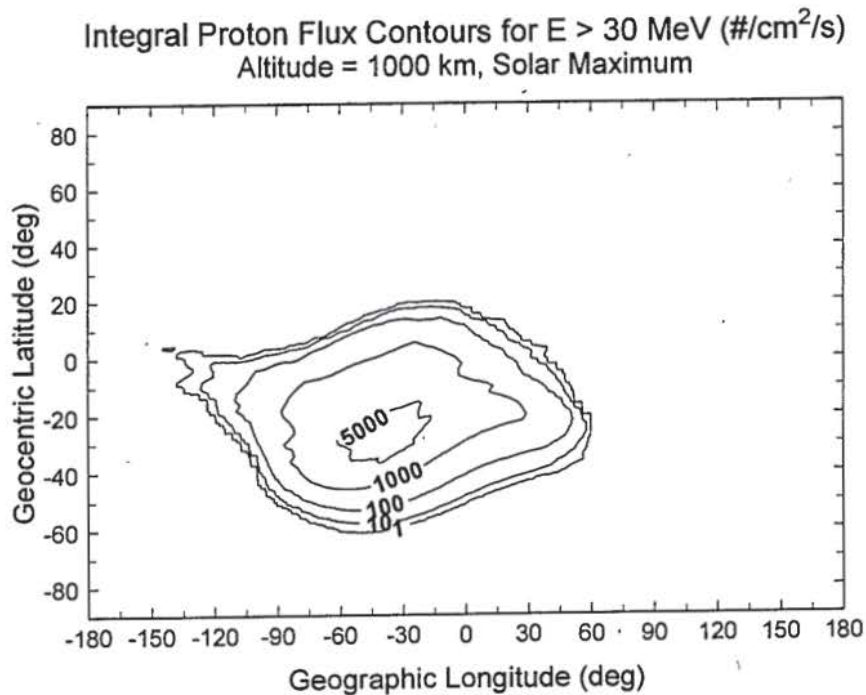
Fig. 5.4.4: Proton flux contours in the inner zone at 1,000 km.
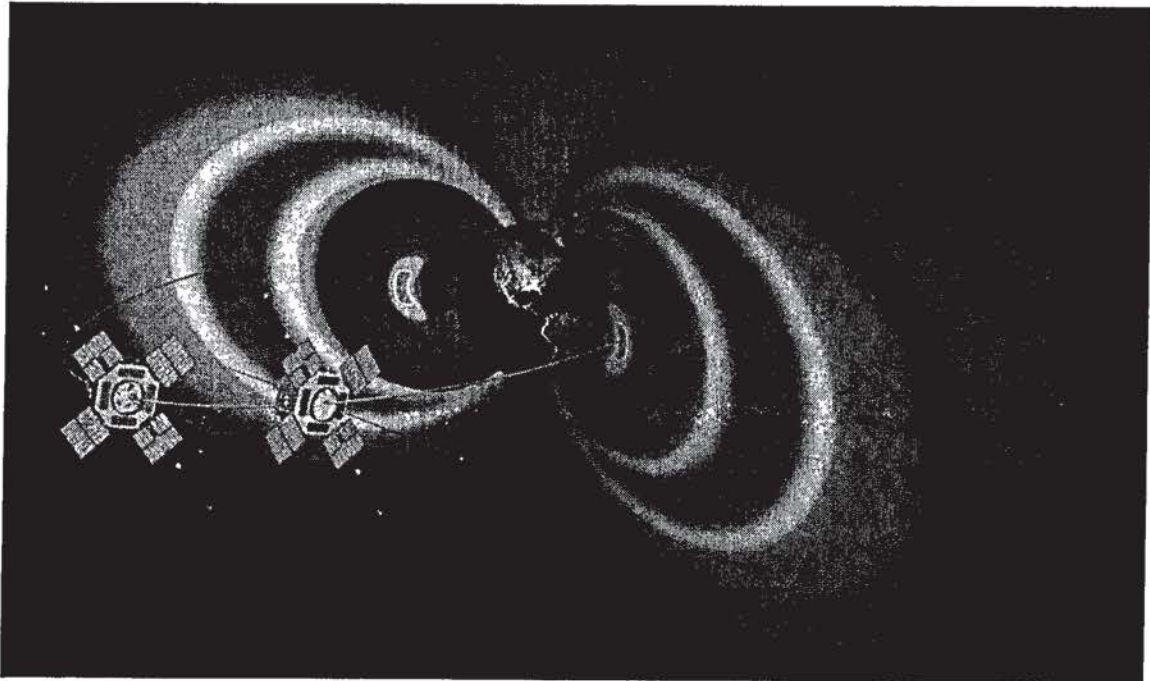
Fig. 5.4.1: An artist's drawing of the Earth's radiation belts. (*NASA, Radiation Belt Storm Probe mission*)

Fig. 5.4.2: Plot of the proton radiation belt showing the South Atlantic Anomaly (SAA) in low altitude regions. (*ESA*)
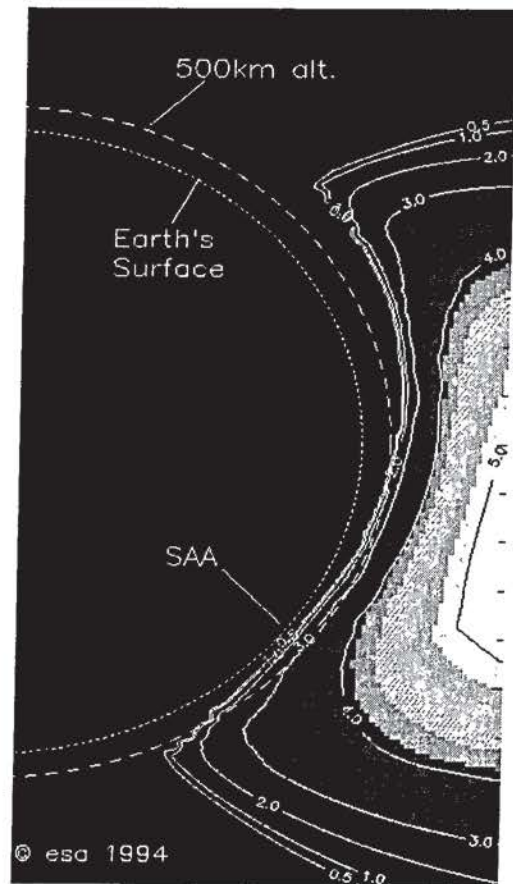
Integral Electron Flux Contours for E > 0.5 MeV (#/cm²/s)
Altitude = 1000 km, Solar Maximum
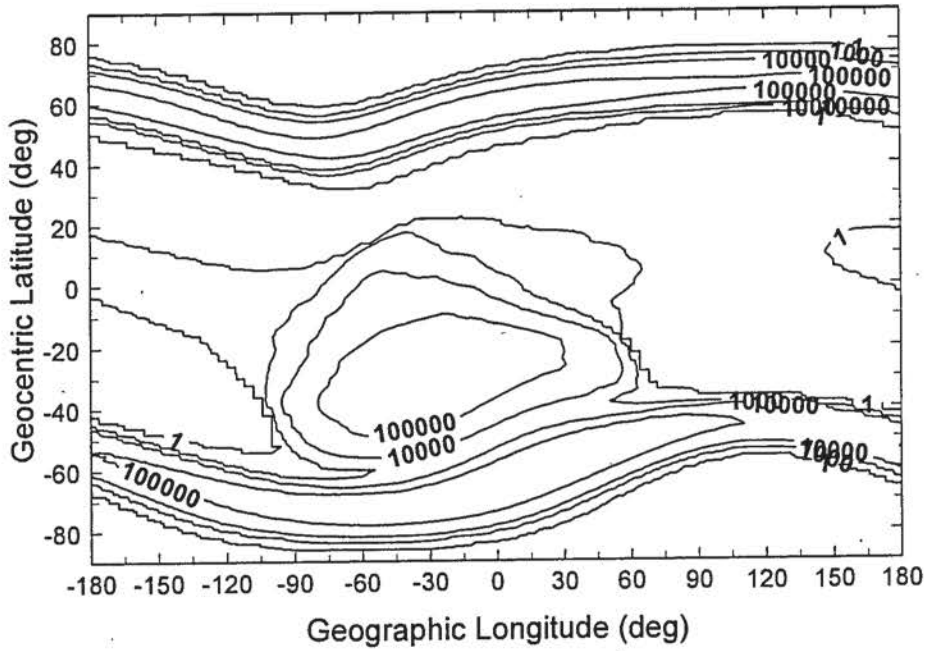
Fig. 5.4.7: At 1000 km, the SAA electrons begins to spread out, covering a larger region.

Daily Integral, Orbit-Averaged Fluences
AE-8, Solar Maximum
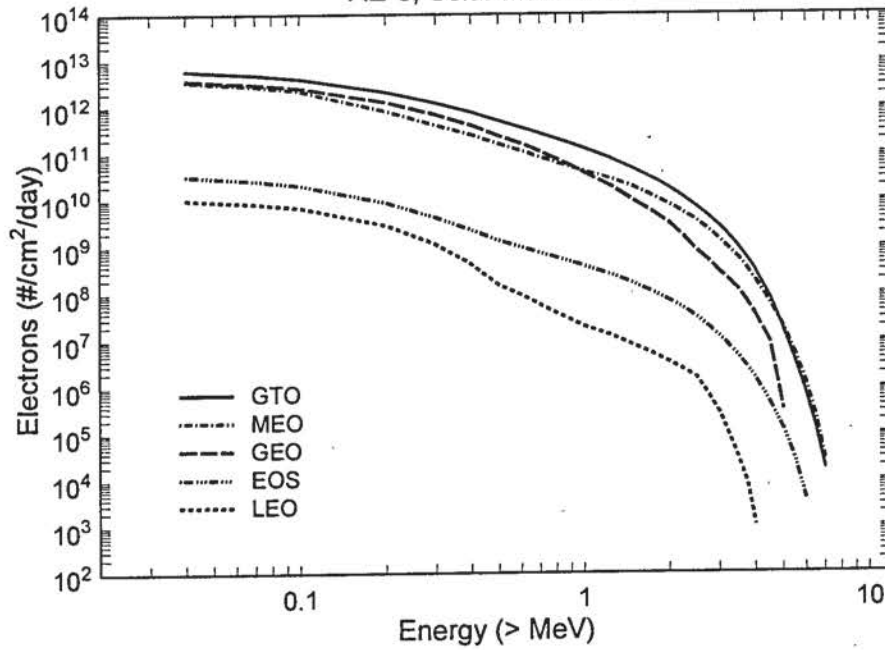
Fig. 5.4.8: High altitude orbits (GEO, GTO, MEO) spend large amounts of time in the intense outer zone resulting in higher daily fluences.

Daily Orbit-Integrated, Integral Proton Fluence
Solar Maximum
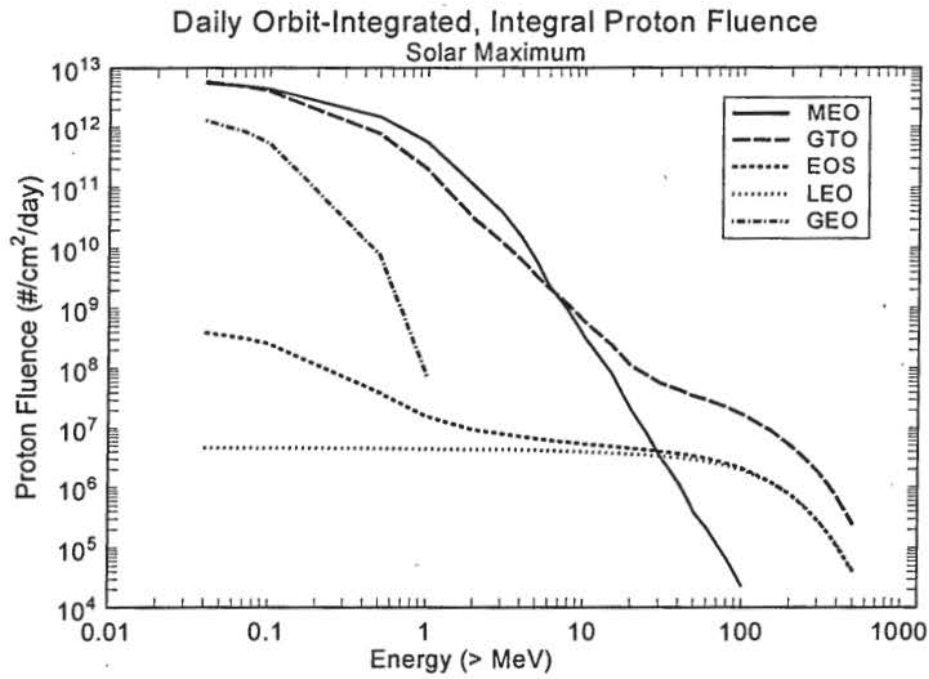
Fig. 5.4.5: Proton fluence levels have large orbit-dependent variations. Note that, for the GEO orbit, the protons cut off at low energies.

Omnidirectional Integral Electron Fluxes at Magnetic Equator
AE-8 for Solar Maximum
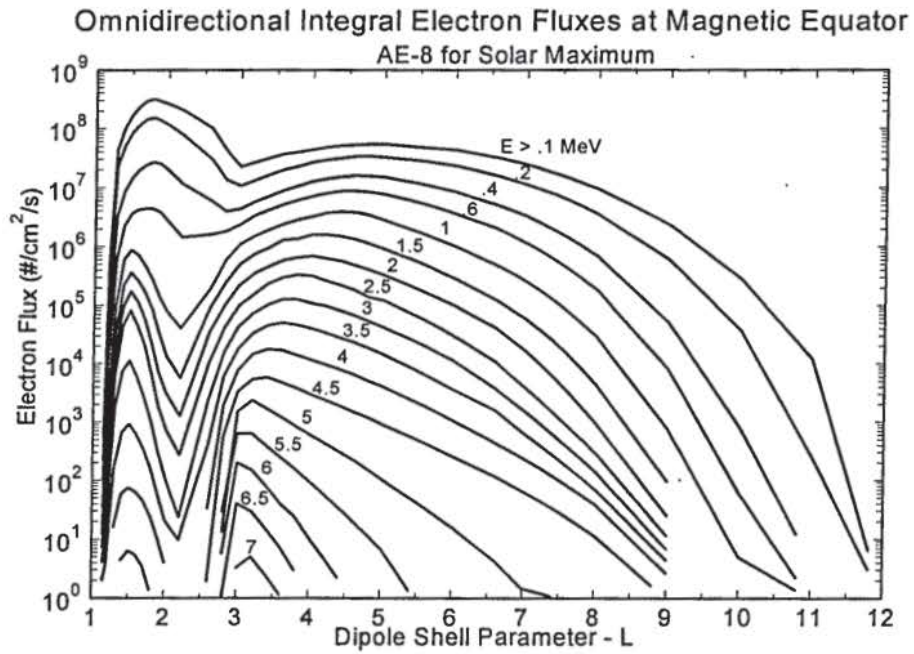
Fig. 5.4.6: Variation of electron flux levels with radial distance from the Earth. Note the double peak showing the inner and outer zones
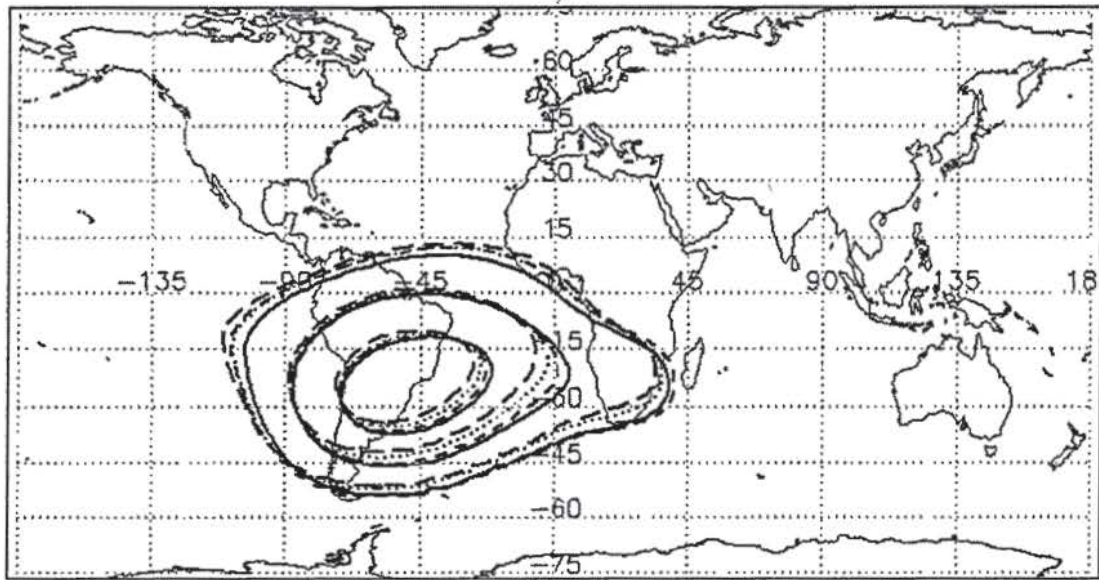
Altitude = 800 to 850 km

Fig. 7.1.1: Boundary contours representing 1/2 maximum (inner most), 1/10 maximum (middle) and the 3σ above background level for the > 23 MeV (solid curve), > 38 MeV (short dash curve), > 66 MeV (dot curve) and > 94 MeV (long dash curve) channels at 800 km.
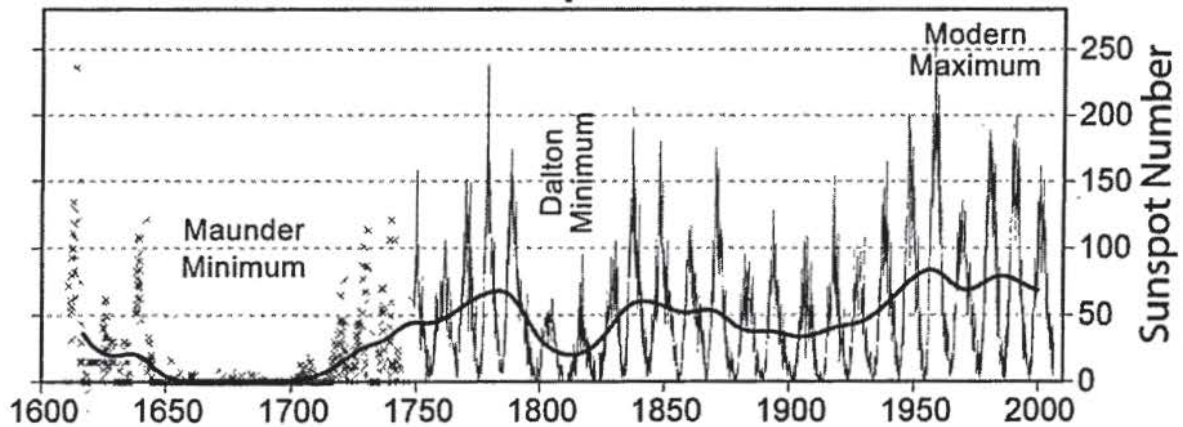
Fig. 7.2.1: Sunspot observations from various sources.
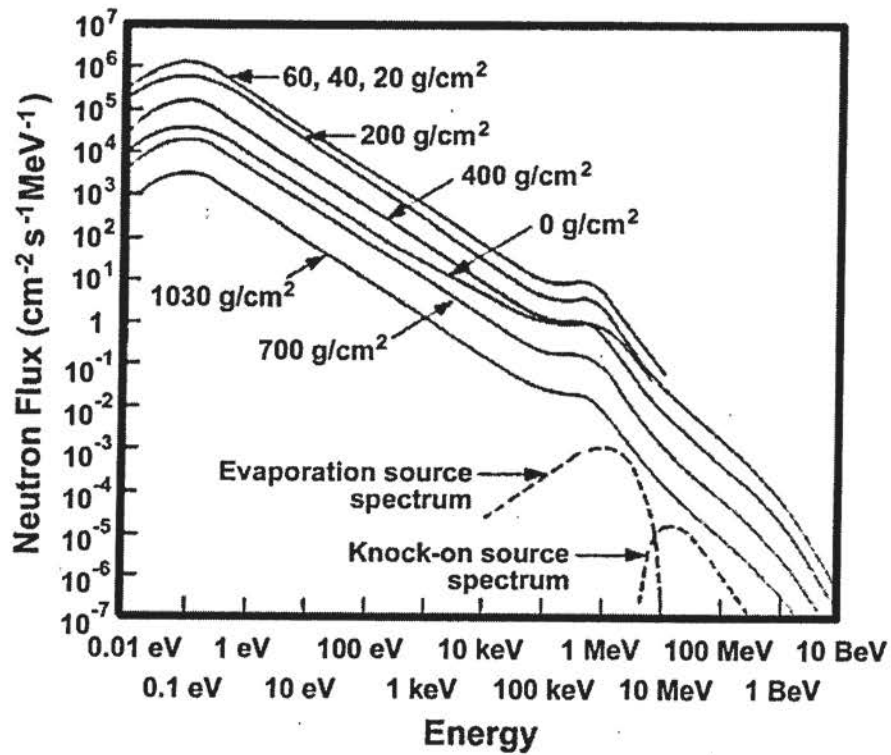
Fig.6.3.1: "Hess values" of measured energy spectra of neutrons at various altitudes up to outer space. The lowest curve at 1030 g/cm² is at sea level and the curve marked 700 g/cm² is at an altitude of 2 miles. *Zeigler*
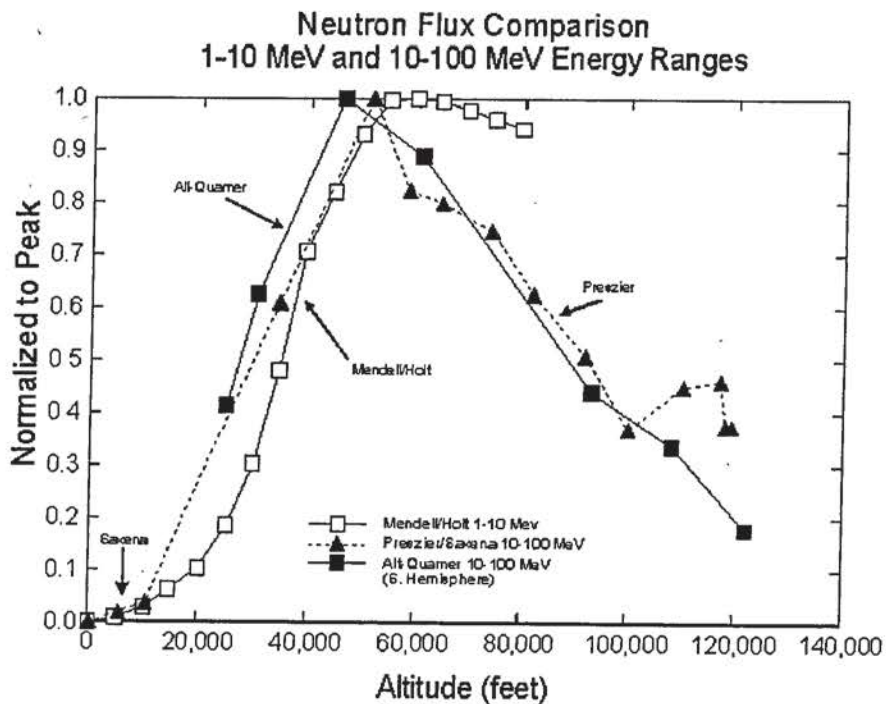
Fig.6.3.2: Measurements of atmospheric neutrons show the variation as a function of altitude. *Normand et al.*
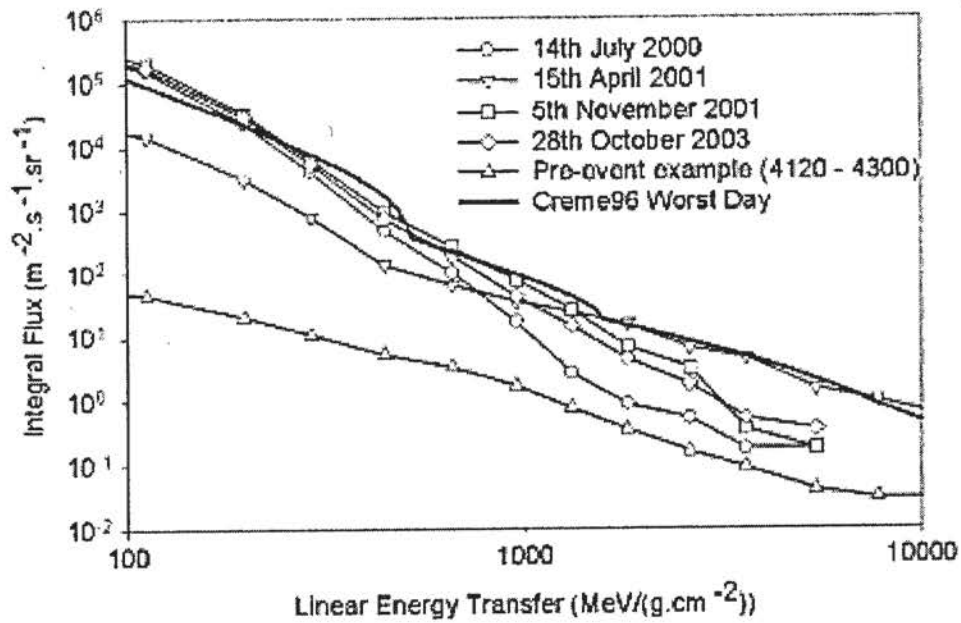
Fig. 7.3.2: Integral LET spectrum under 6 mm of equivalent aluminum shielding at the peak of the October 28, 2003, event is compared with the previous largest events of this solar maximum and with the CREME96 worst day.

CNO - 24 Hour Averaged Mean Exposure Flux
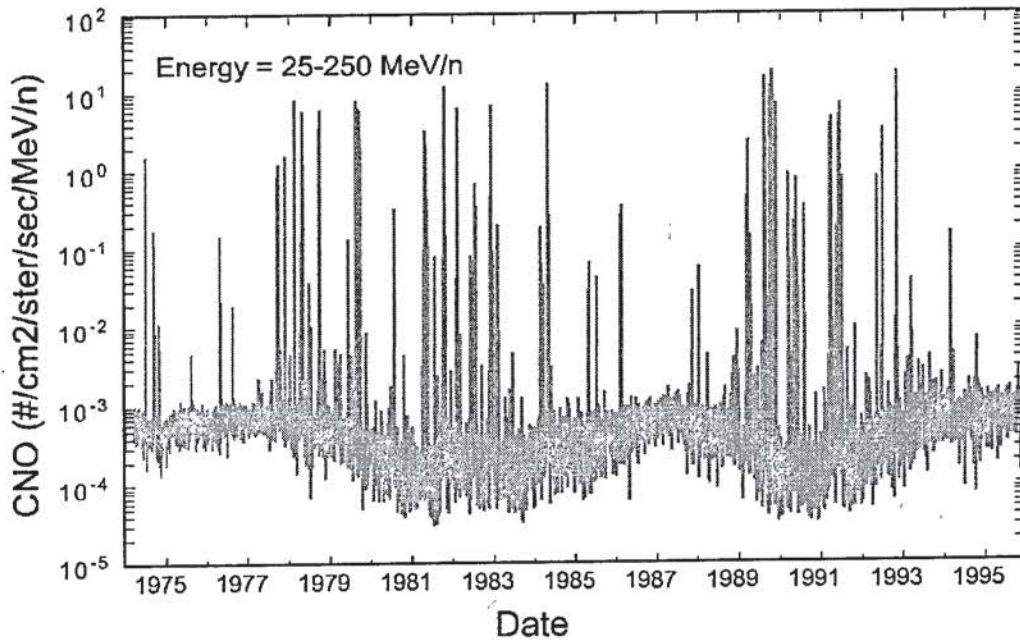
Fig. 7.4.1: IMP-8 measurements of interplanetary ions from the C-N-O group. Note the solar particle event spikes superimposed on the lower level, slowly varying galactic cosmic rays. *after Nakamura*

Sunspots & Magnetic Storm Days
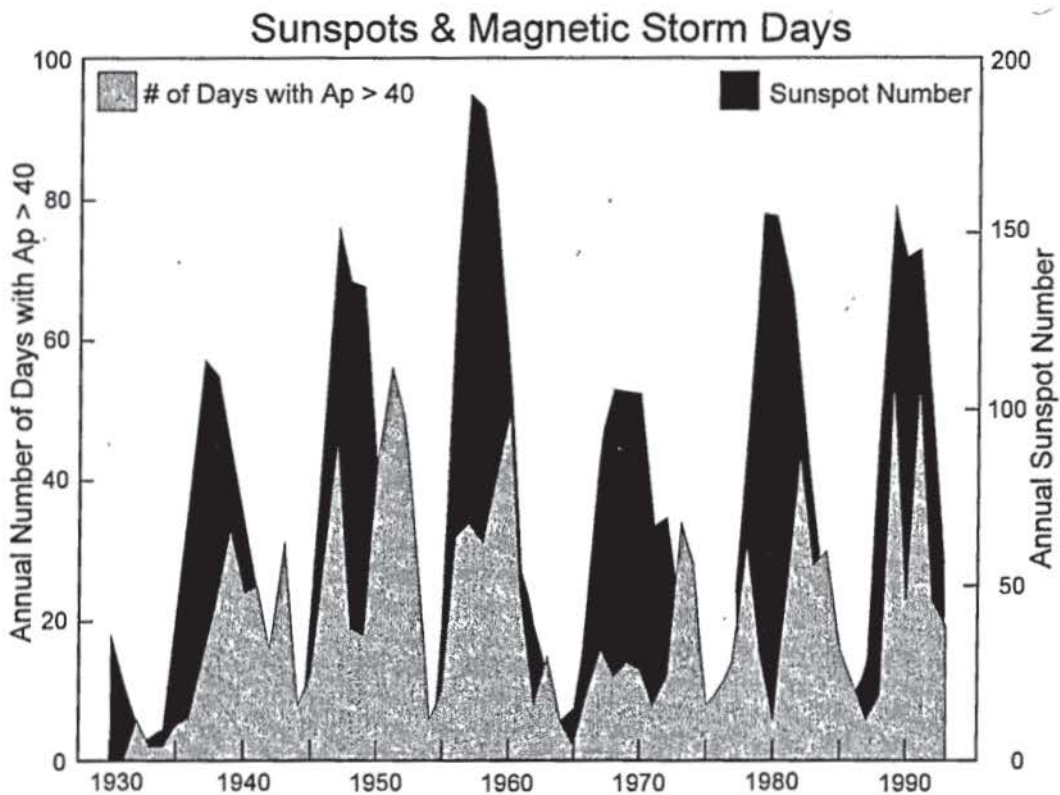
Fig. 7.2.2: The number of magnetic storm days correlates closely with the level of solar activity, as measured with sunspot numbers.

Event Fluences For Cycles 20 - 22
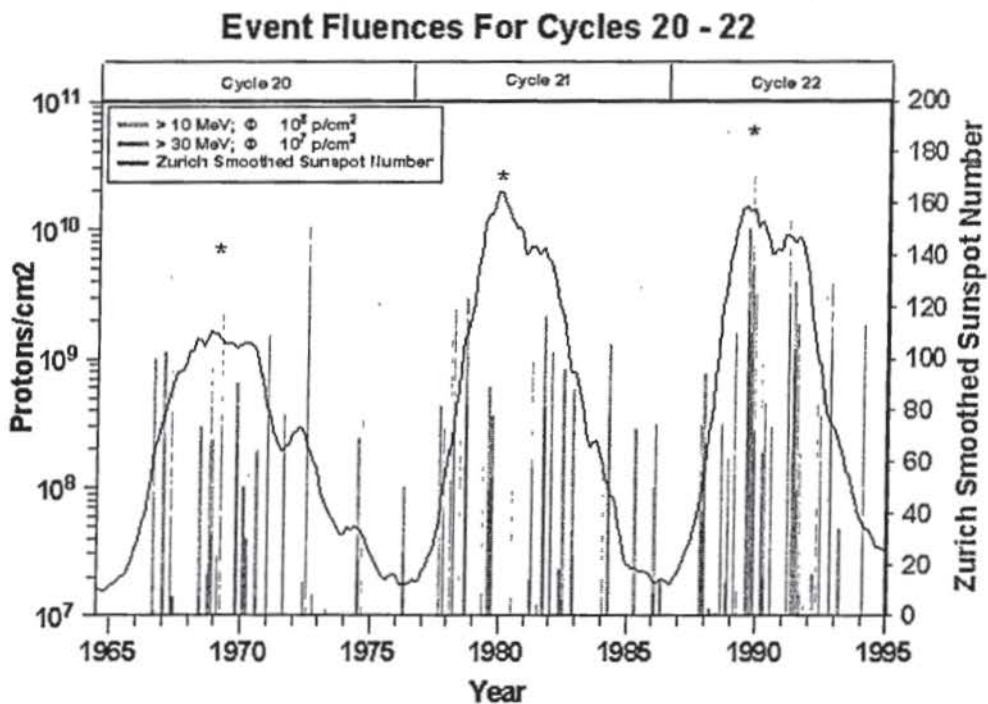
Fig. 7.3.1: Large solar proton events for the last three solar cycles. The number of sunspots is superimposed on the graph.

GOES-7 112.2 W. Lon. Electrons, E>2 MeV
October 1, 1993 - March 31, 1994
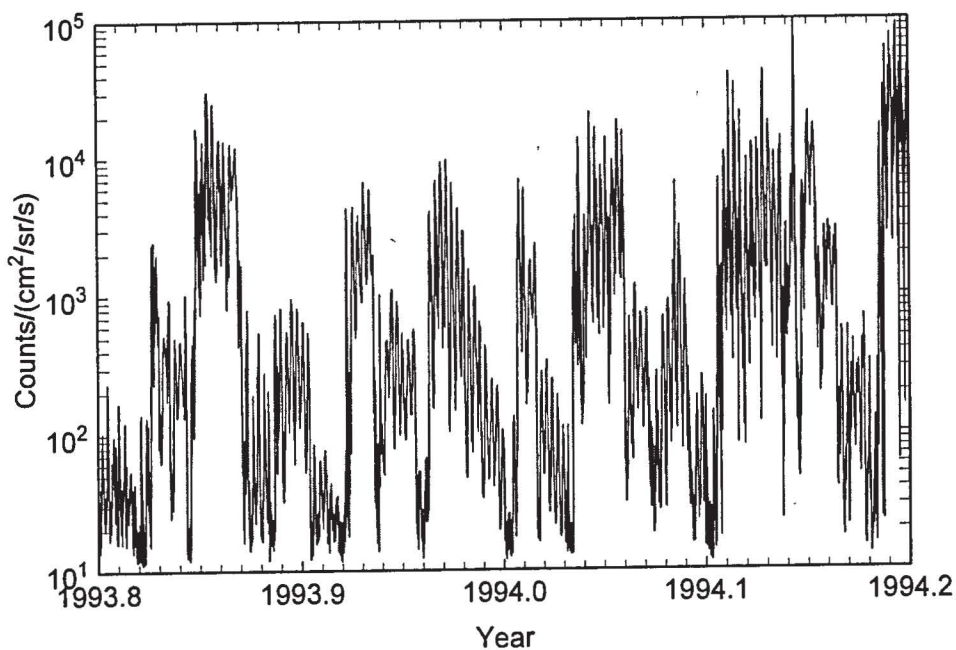
Fig. 7.5.3: Cyclic variation in electrons in the outer zone due to 27-day solar rotation. *after Nakamura*

SAMPEX/P1ADC: Electrons E > 0.4 MeV
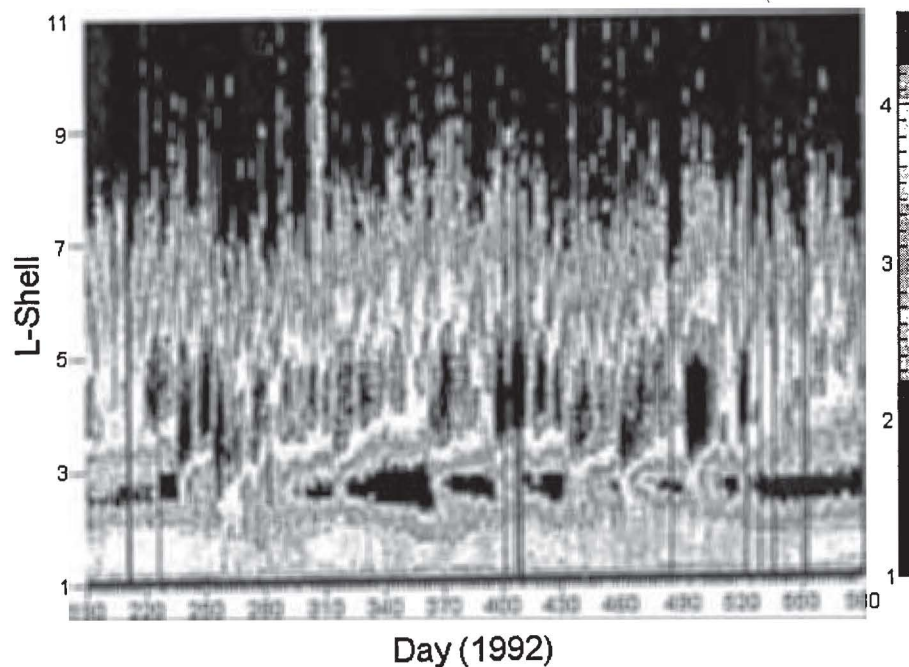
Fig. 7.5.4: Radiation belt electrons (E > 0.4 MeV) measured by the SAMPEX spacecraft. The measurements are plotted as a function of L and the day of year. The outer zone (L>3), slot region (L=2-3), and the inner zone (L<3) can be clearly seen. The plot shows the dynamic electron population in the outer zone and the numerous episodes of the slot region being filled with storm electrons. *S. Kanekal, NASA/GSFC*

P8 (80 MeV), B/B$_{min}$=1.0
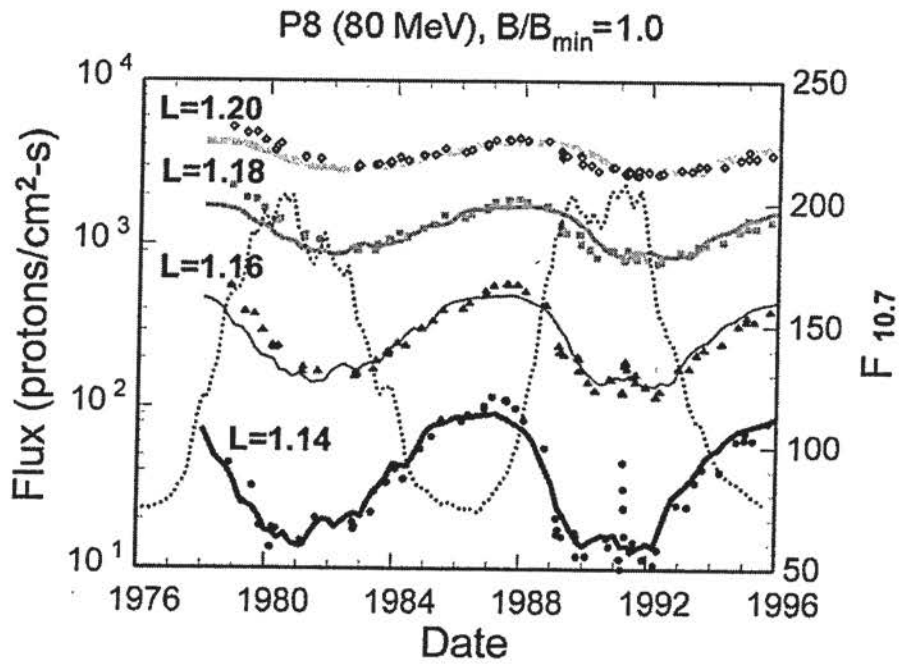
Fig. 7.5.1: Protons distributions for protons in the inner zone at >16 MeV which were used as the basis for the first trapped proton model with true solar cycle dependence. *Huston and Pfitzer*

EXPLORER 12 302 (E>1.9 MeV)
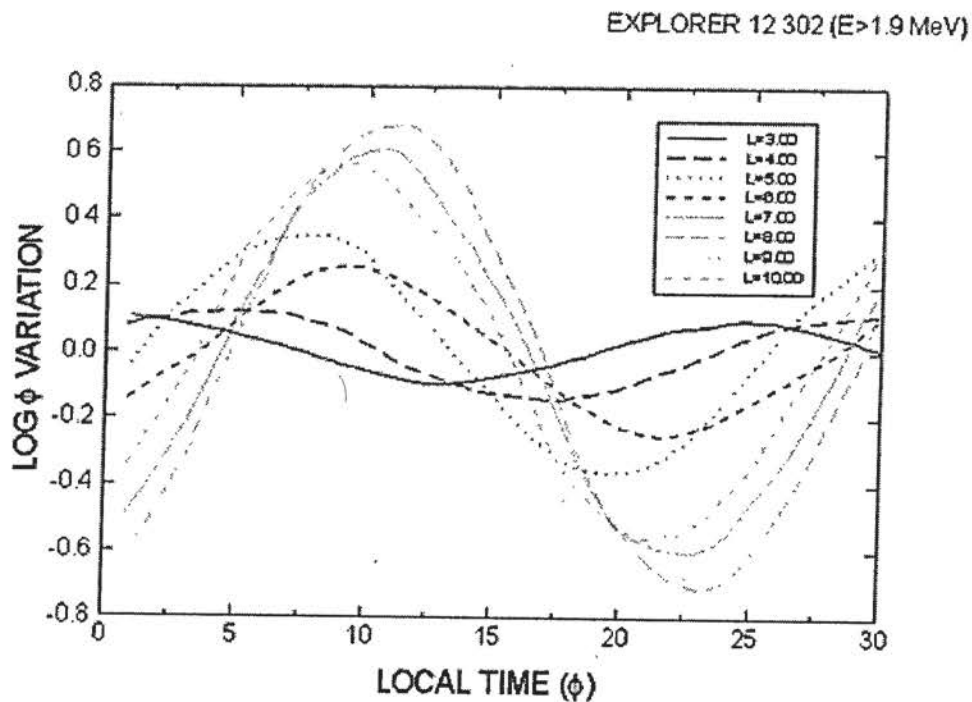
Fig. 7.5.2: Local time variations of outer zone electrons become more pronounced with increasing L. *after Stassinopoulos*

Total Integral LET Spectra for Solar Heavy Ions
GEO: I=0 deg, H=36,000/36,000 km, 100 mils Al
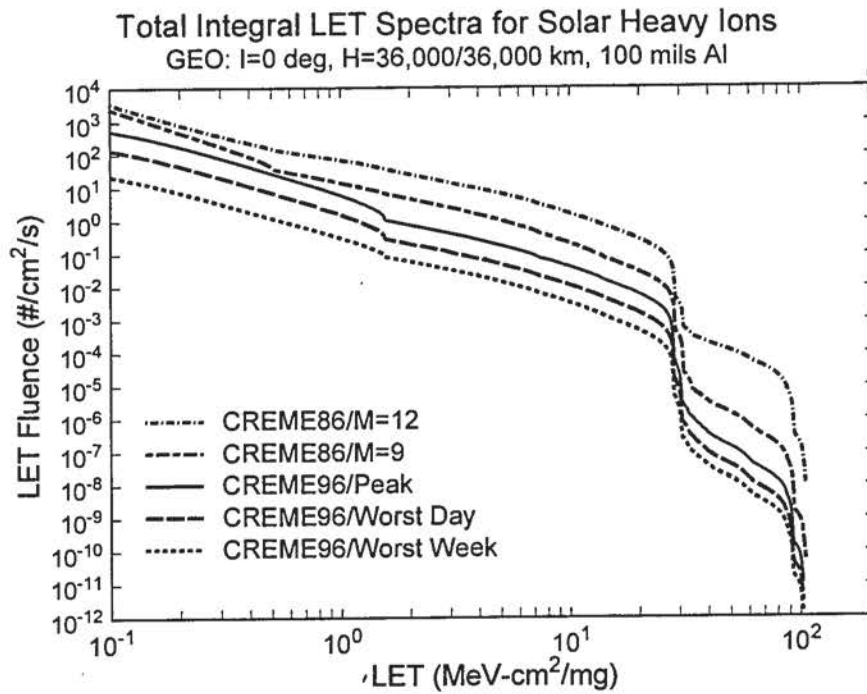
Fig. 8.1.5.2: Total integral LET spectra from CREME96 for GCRs and solar heavy ions.
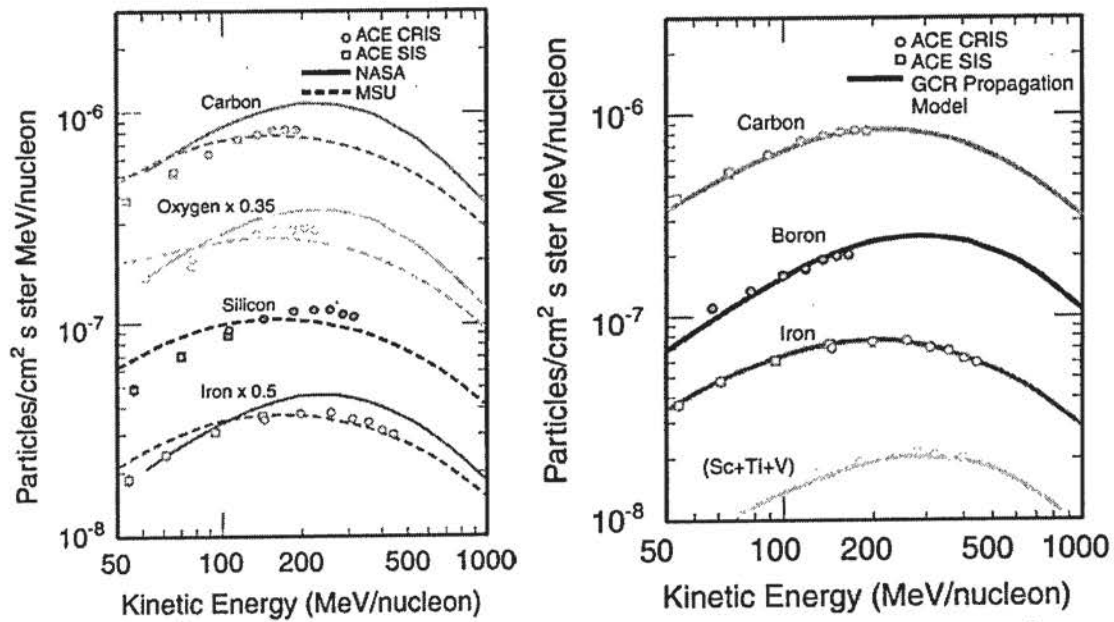
Fig. 8.1.6.1: Comparison of NASA, MSU, CIT Models with ACE Instrument Data.
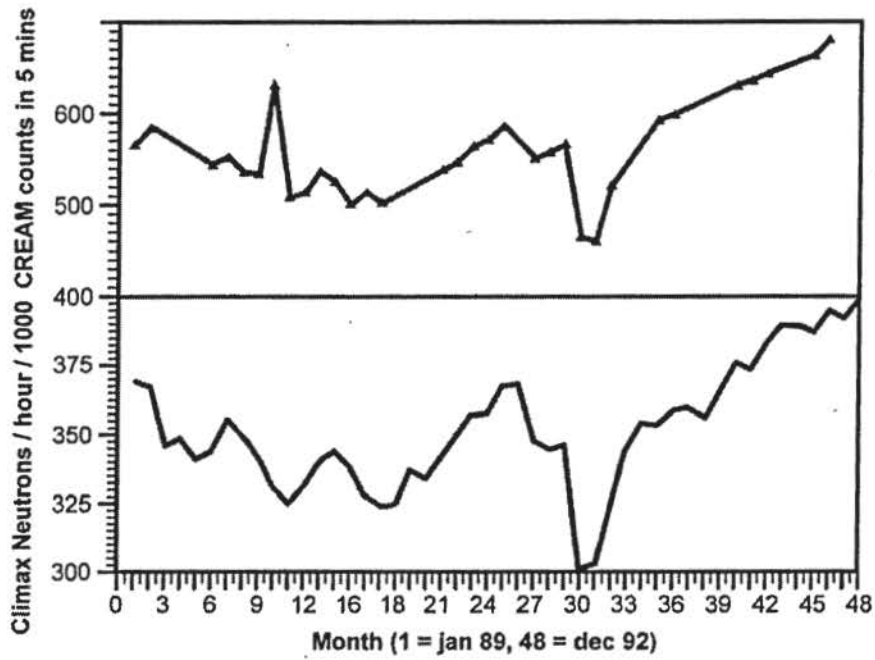
Fig. 7.6.1: Monthly mean count rates from the CREAM instrument on Concorde from Jan 1989 to Dec 1992 compared with ground level neutron monitor at Climax.
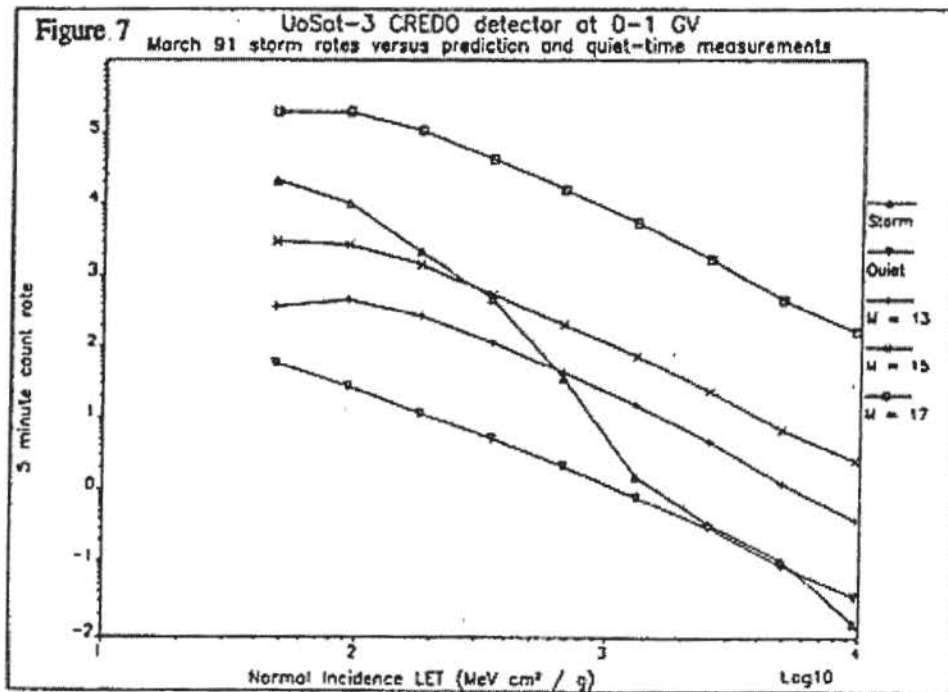
Fig. 8.1.5.1: LET spectra measured by UoSAT-3 compared to the CREME86 solar heavy ion models.
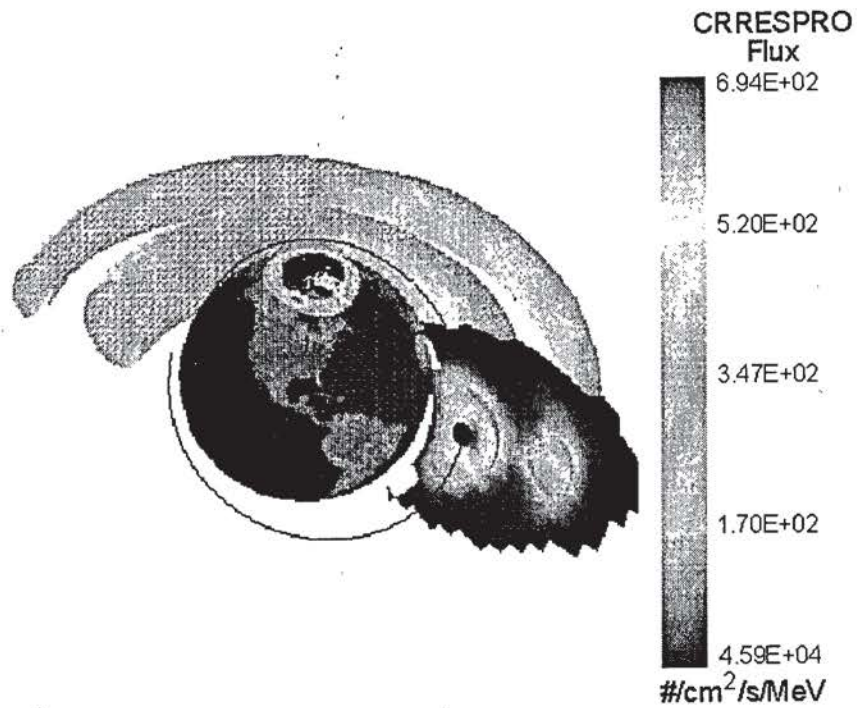
Fig. 8.3.3.1: Trapped proton storm belt measured by the CRRES satellite March 1991.
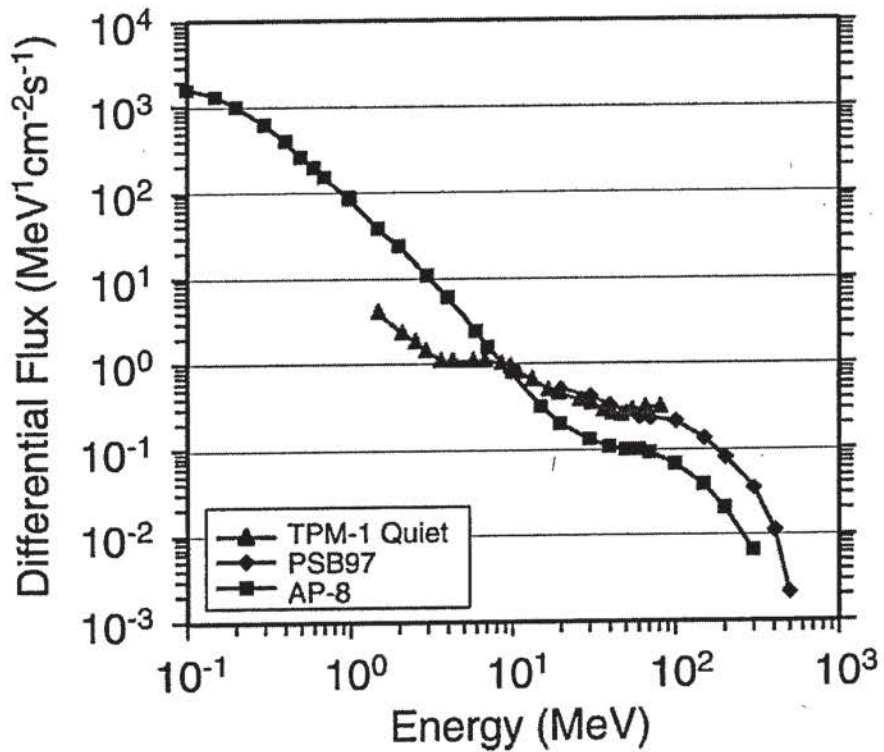
Fig. 8.3.5.1: Comparison of inner zone trapped protons models.
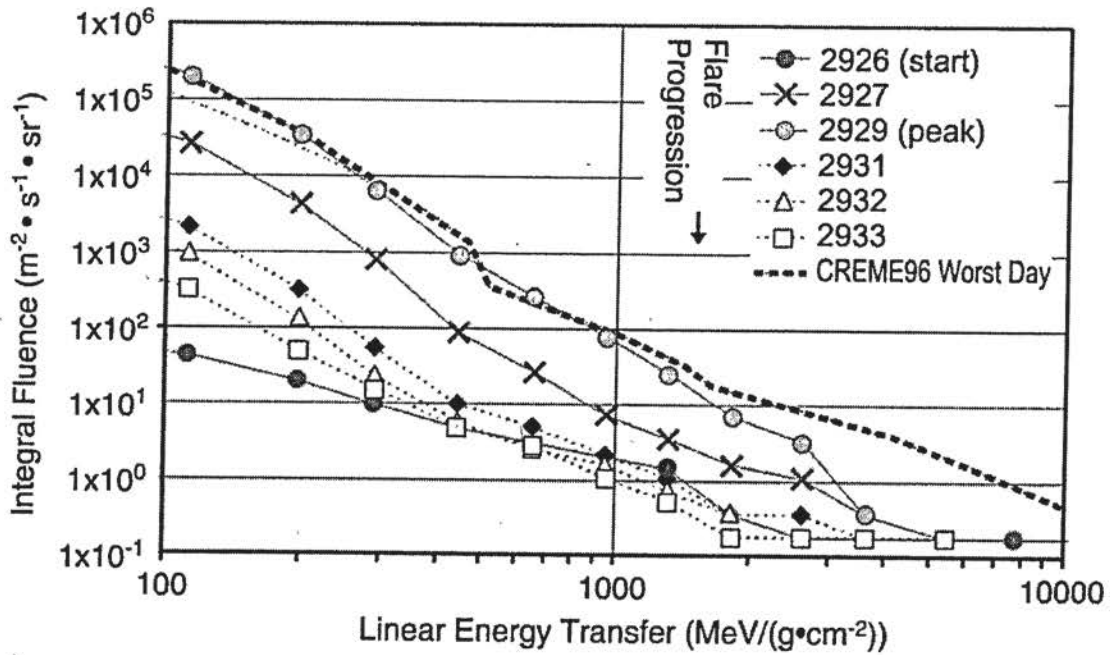
Fig. 8.1.6.2: Comparison of CREME96 to CREDO Measurements during 2000 and 2002 using the MPTB.
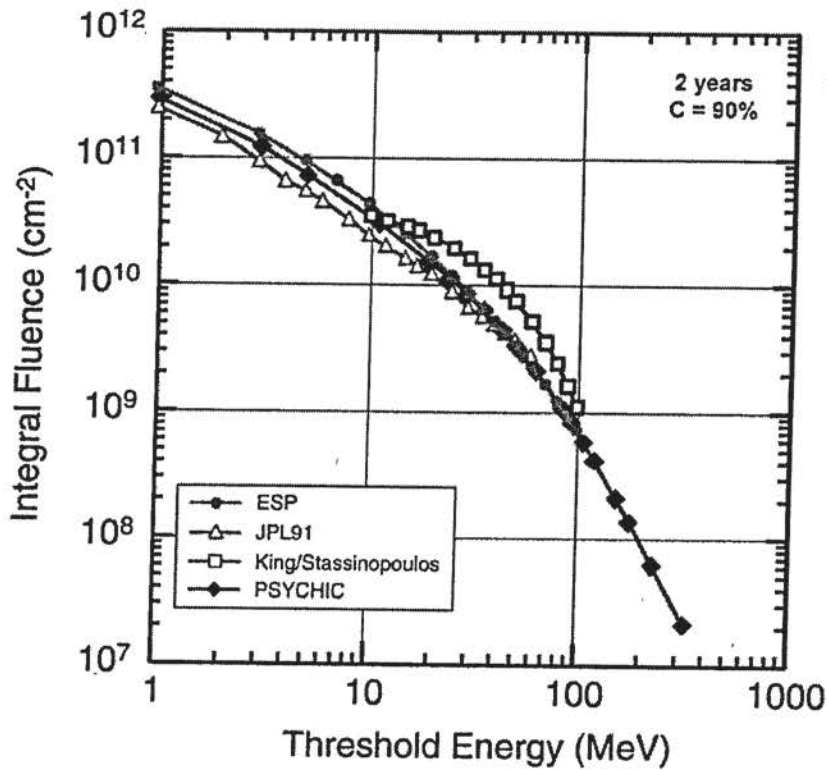
Fig. 8.2.3.1: Comparison of cumulative solar proton models, ESP, JPL91, King/Stassinopoulos, and PSYCHIC Models.
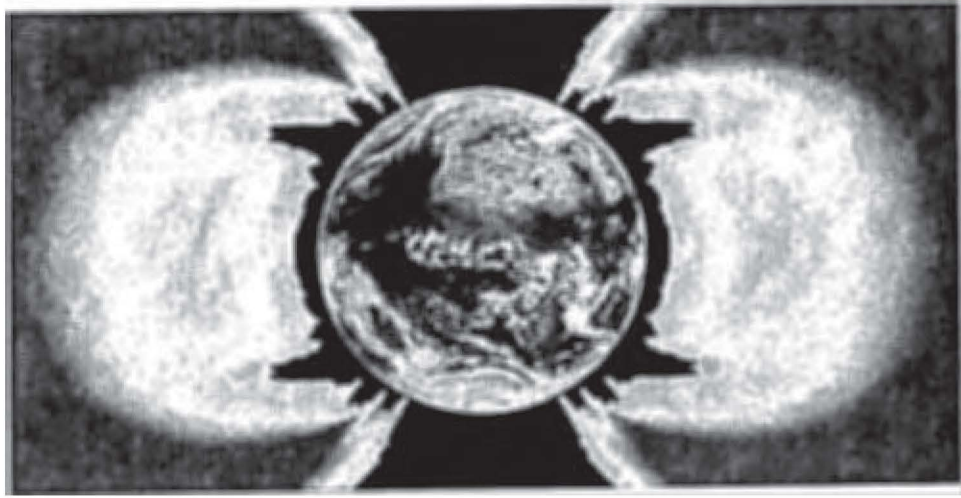
Fig. 8.3.6.1: Electron fluxes in the Earth's magnetosphere calculated with the Salammbo code. *ONERA*

T_0 Time T_{end}
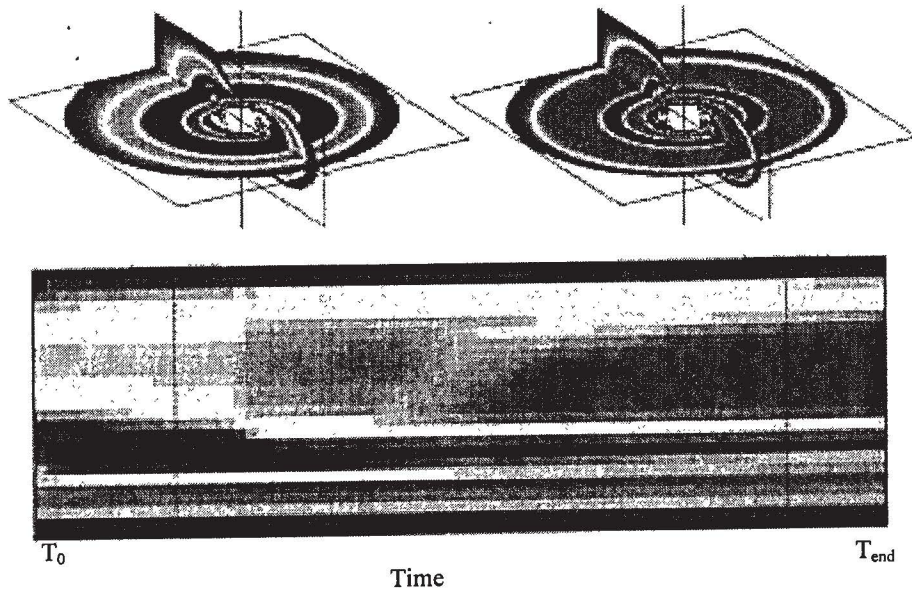
Fig. 8.3.6.2: Simulation of electron diffusion in the Earth's magnetosphere as the result of a storm with the Salammbo code. *ONERA*
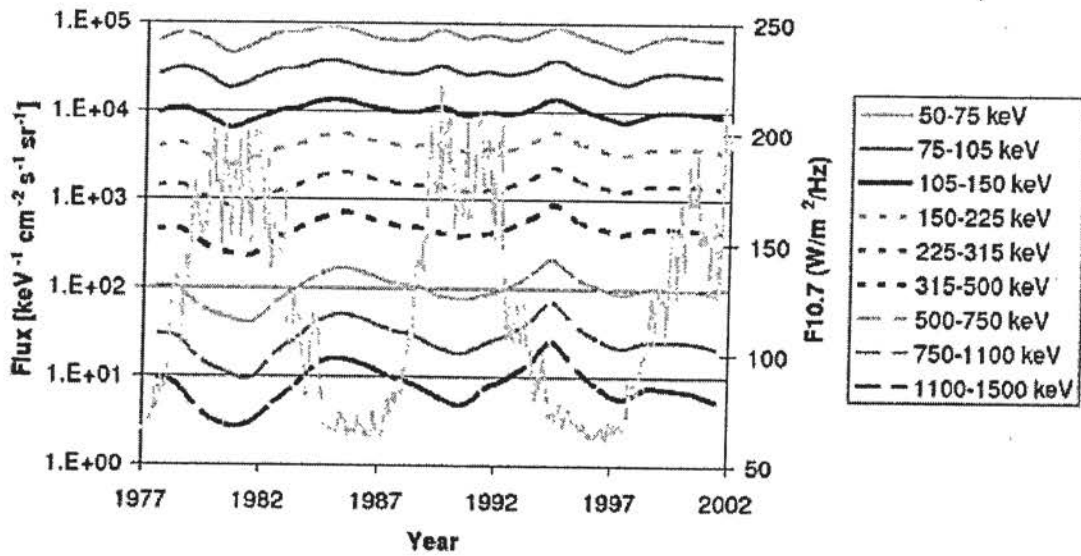
Fig. 8.3.5.2: Electron fluxes at geostationary orbit as a function of the solar cycle.
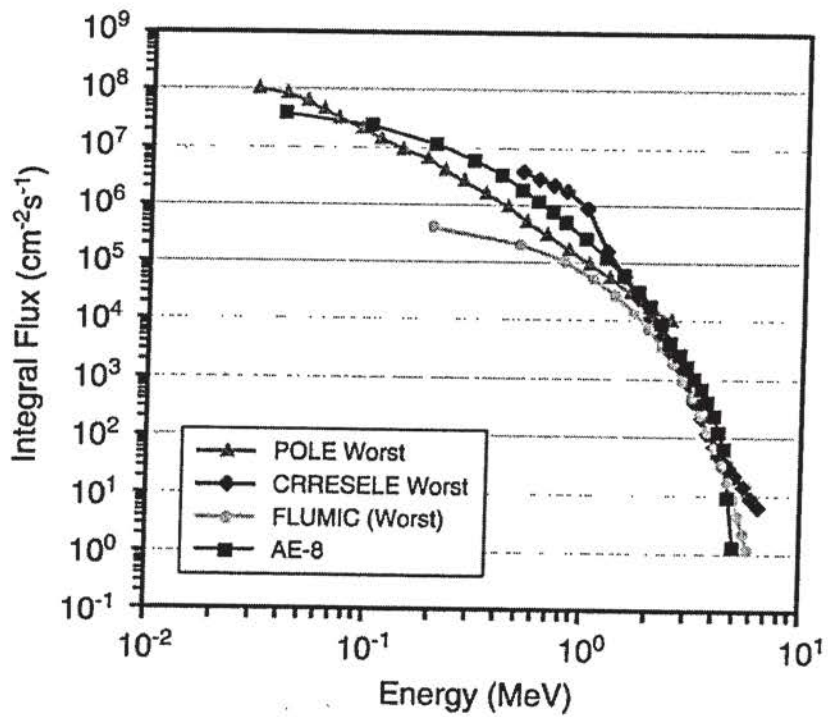
Fig. 8.3.5.3: Comparison of "Worst Case" POLE, CRRESELE, and FLUMIC Models with the AE-8 Model
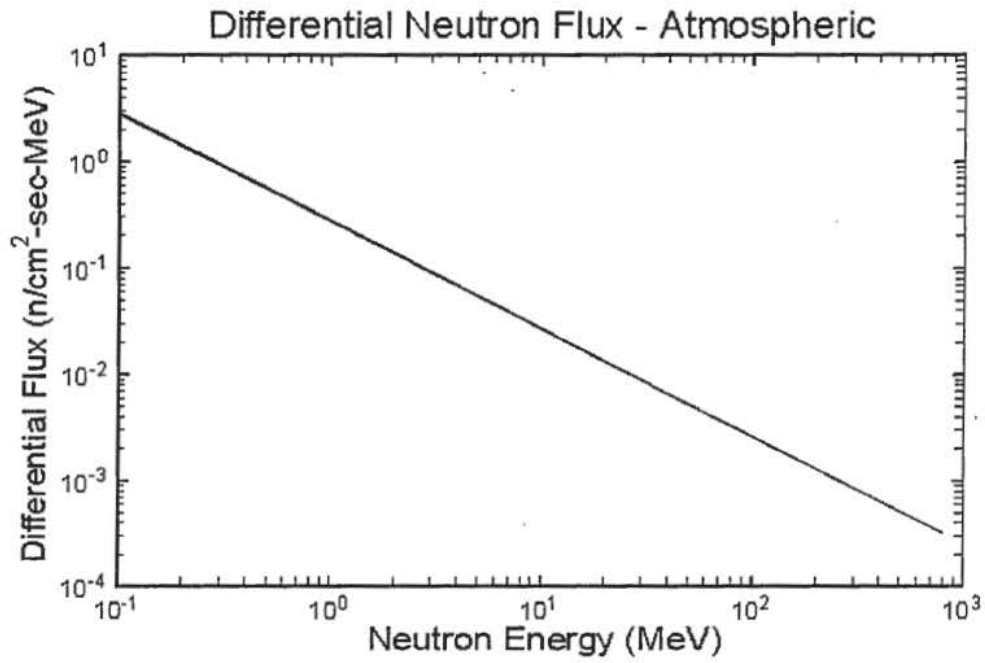
Fig. 8.5.1: Since the neutron flux energy spectrum is invariant in latitude and altitude, it can be applied across spatial parameters. Normand *et al.*
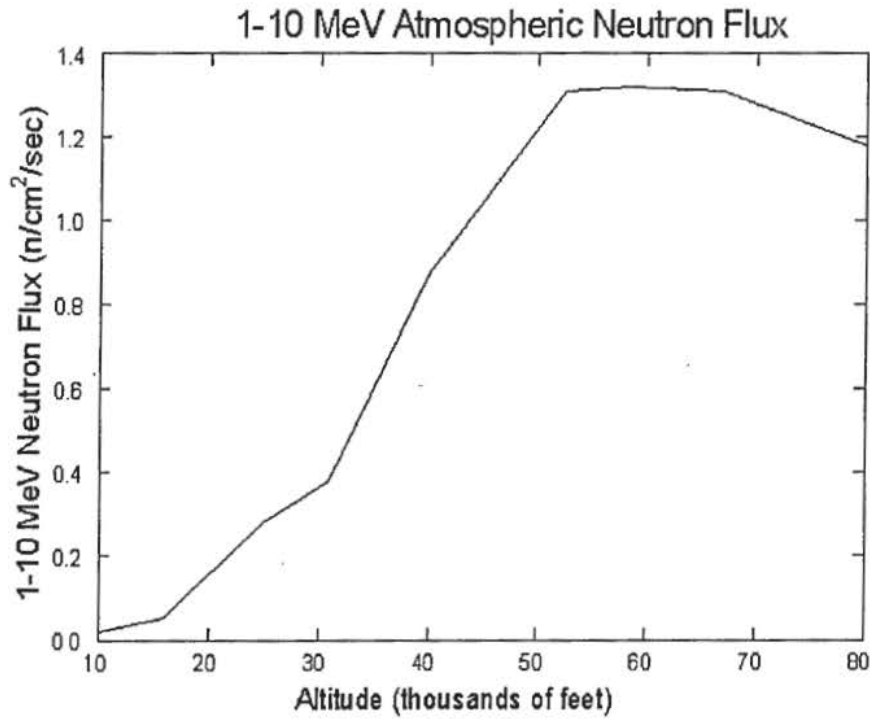
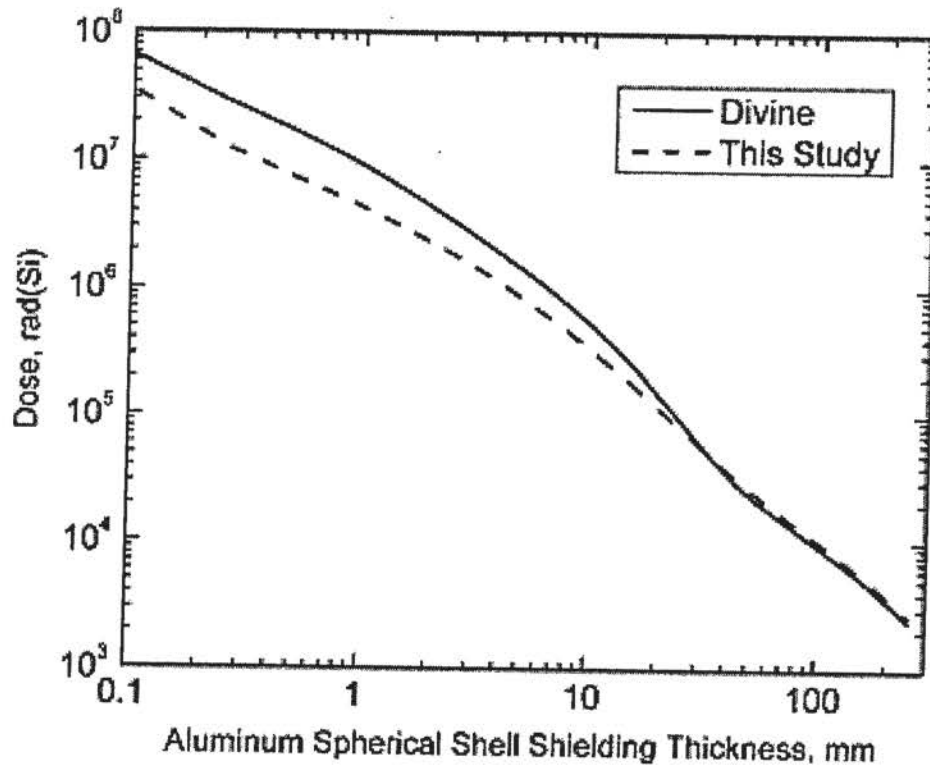Fig. 8.5.2: The Taber and Normand model of neutron flux - altitude dependence. Note the peak of the flux levels is at 60,000 feet, Normand *et al.*

Fig. 8.4.2.1: Dose estimates versus aluminum shielding thickness for the GIRE and the Divine spectra in Fig. 4 (2.54 mm = 100 mils) for the Europa Mission.
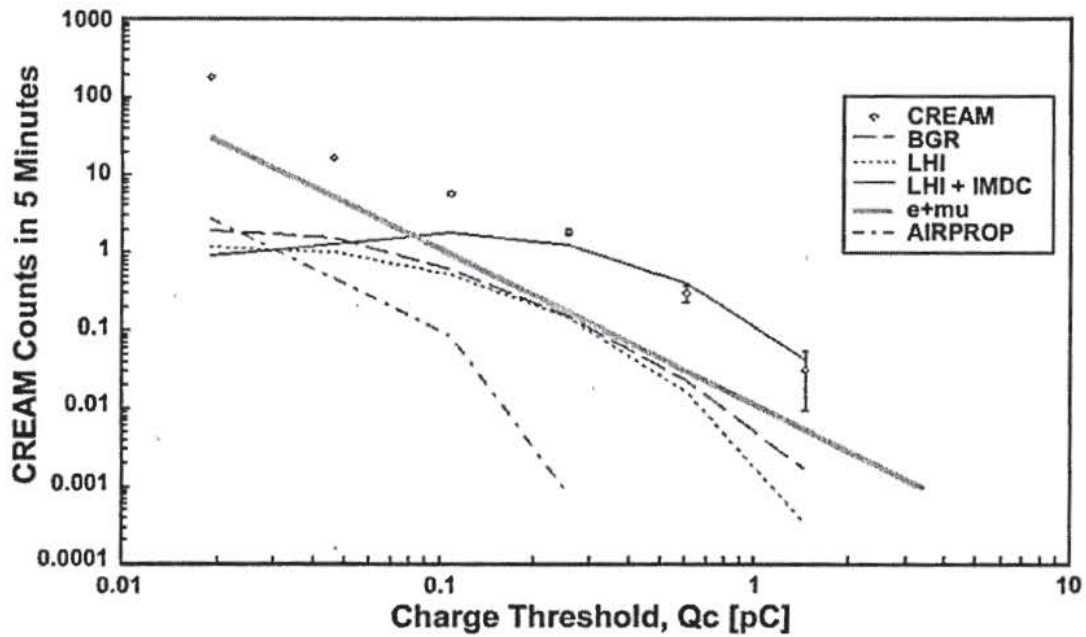
Fig. 8.5.5: The spectrum of charge deposition from CREAM at 30,000-31,000 feet compared with predictions. Neutrons dominate at high values while electrons and muons contribute at the low end.
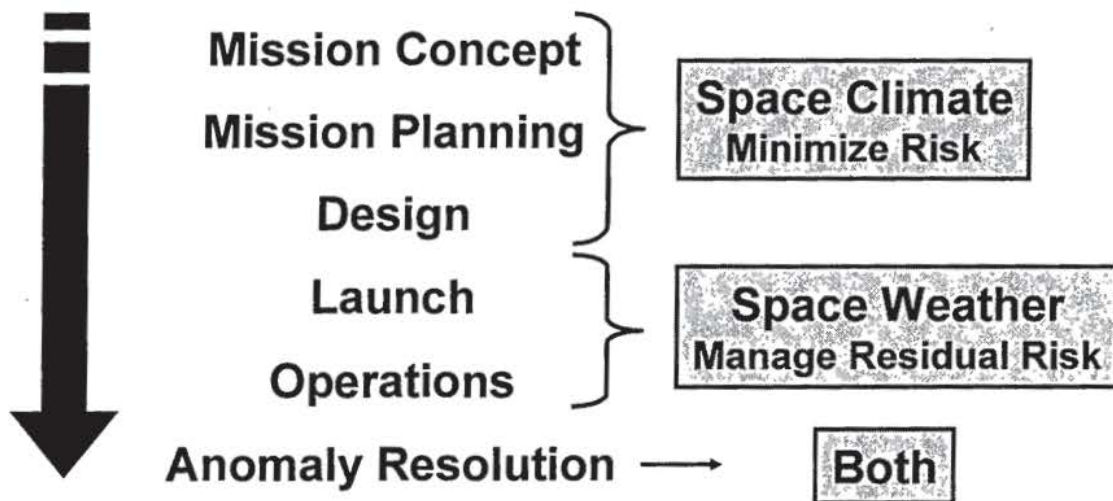

Fig. 9.1: Space climate and space weather models are critical to radiation hardness assurance in all phases of spacecraft missions.
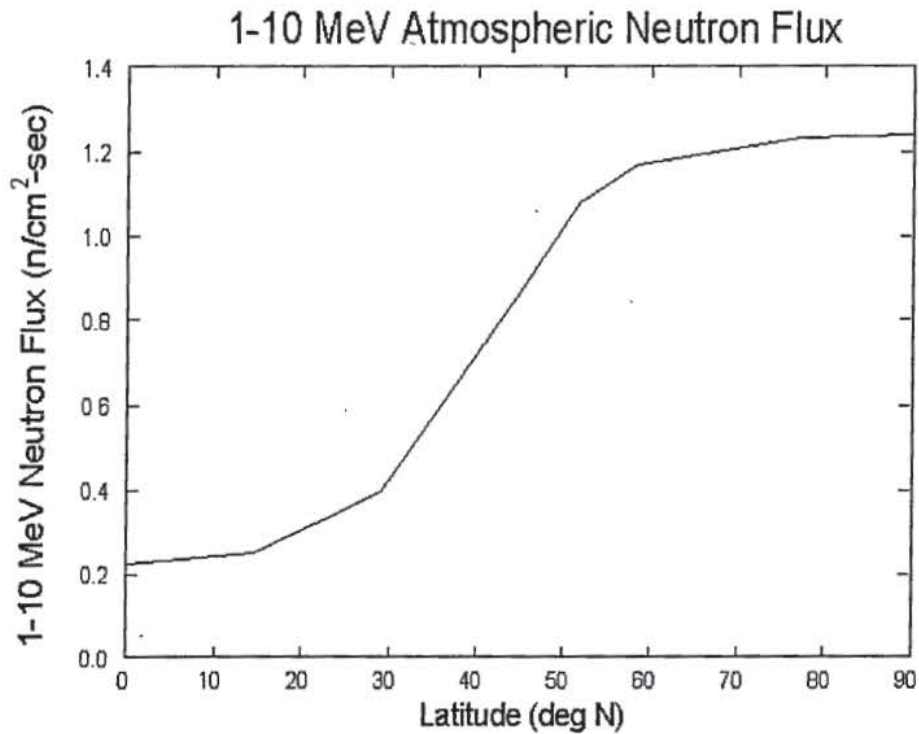
1-10 MeV Atmospheric Neutron Flux

Fig. 8.5.2: The Taber and Normand model of neutron flux - latitude dependence. Note the increase of flux levels with increasing latitude, Normand *et al.*
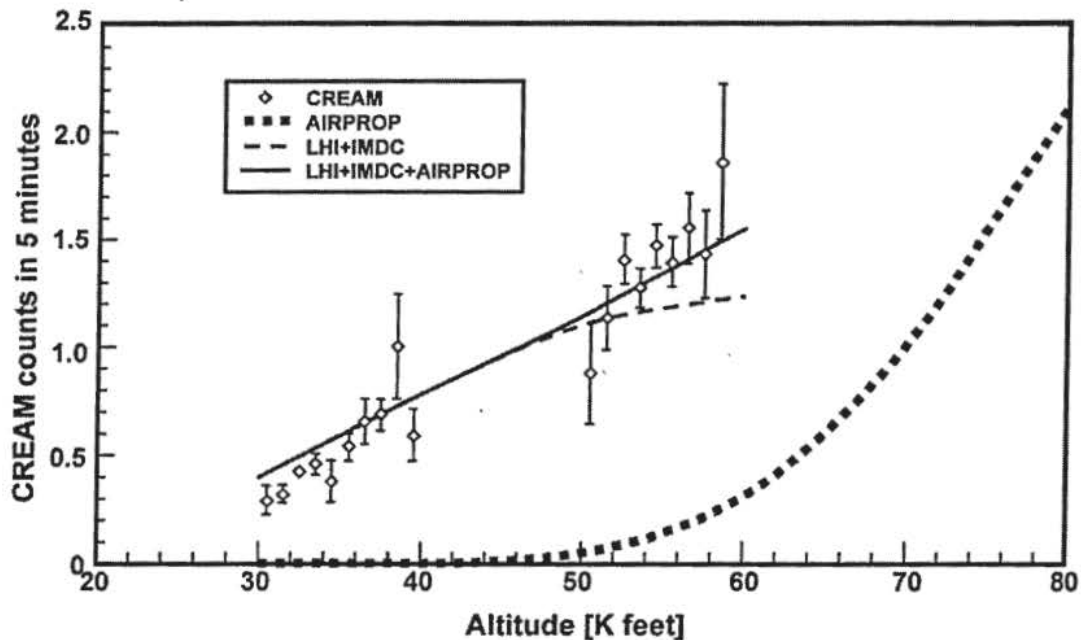

Fig. 8.5.4: Average CREAM channel 5 count rates as a function of altitude at 1-2 GV from SAS and Concorde flights. Also shown are the predictions from AIRPROP and from neutron interactions as calculated using radiation transport and microdosimetry codes (LHI+IMDC). Neutrons dominate at 3,000 to 40,000 feet but cosmic ray ions contribute at supersonic altitudes.